UNIVERSITY OF TORONTO

Hybrid Rocket Aerospike Nozzle Design

by

Emerson Vargas Niño, Kevin Course, Yao Tong, Shi Yu, Qidong Zhao

APS490Y

Department of Applied Science and Engineering

October 2020

UNIVERSITY OF TORONTO

Abstract

APS490Y
Department of Applied Science and Engineering

by Emerson Vargas Niño, Kevin Course, Yao Tong, Shi Yu, Qidong Zhao

UTAT has requested the investigation of aerospike nozzle due to their proven efficiency advantages over conventional bell nozzles. Despite their inherent advantages, UTAT has been reluctant to explore this concept in the past due to significant challenges associated with their implementation. In specific, aerospike nozzles are notoriously challenging to cool and integrate with engine assemblies. This paper presents a detailed method for the design and analysis of an aerospike nozzle following the example of a nozzle designed for use on a small scale test stand. Processes for judiciously choosing the engine parameters, designing the nozzle contour, applying cooling analysis, optimizing the contour, completing the mechanical design, and analyzing an aerospike nozzle using modern computational methods are explained in detail. In addition, a cost, safety, and environmental analysis is performed for the example nozzle. Furthermore, a comparison of aerospike engine performance versus that of a conventional bell nozzle reveals that a scaled up version of the example test stand nozzle could be expected to be operate with an average efficiency of approximately 4% better than a the conventional bell nozzle currently in use by UTAT's flagship rocket, Defiance.

Contents

List of Figures

List of Tables

Symbols

Symbols

A	Passage area normal velocity vector
Bo	Boiling number
Co	Convection number
Cp	Specific heat capacity at constant pressure
D	Diameter
Fr	Froude number
G	Mass flux per unit area and per unit time
h	Convective heat transfer coefficient
Δh_{vap}	Specific heat of evaporation
k	Thermal conductivity
$\dot{m}$	Mass Flow-rate
M	Mach Number
P, p	Pressure
Pr	Prandtl number
q	Heat flux
r	Radius
Re	Reynold number
s	Meridonal coordinate
T	Temperature
V, U	Velocity
w	Temperature exponent of the viscosity equation
x	Axial direction along the nozzle, vapour quality
β	Reference temperature ratio
ρ	Density
γ	Ratios of specific heats (isentropic exponent)
ϵ	Expansion ratio
ν	Prandtl-Meyer expansion fan angle
μ	Mach angle, dynamic viscosity
γ	Specific heat ratio
η	Efficiency
ψ	Two phase multiplier for the heat transfer coefficient

Subscripts

c	Coolant
g	Combustion gas
t	Nozzle throat
w	Wall
∞	Free stream

Chapter 1

Introduction

1.1 Problem Description

The main objective of this project is to design, analyze and document the design work-flow required to build and test an aerospike nozzle suitable for a hybrid rocket engine.

A key reason that UTAT commissioned this project is due to the increasing design apogee that UTAT sets out year after year. The efficiency provided by an aerospike nozzle is most applicable in single stage to orbit vehicles (SSTO), where a single engine will have to traverse across a high range of atmospheric pressures. An aerospike nozzle can effectively compensate for the wide ranges of atmospheric pressures while a more typical nozzle, such as a bell nozzle does not have this feature as it is designed with only a single pressure in mind.

There is a clear pattern of raising the bar on apogee year after year in rocket design and UTAT hopes to continue the pattern in the coming years. In 2014 UTAT worked on "EOS III", 270lbf thrust N2O-Paraffin Hybrid rocket designed to 10,000 ft. In 2015 UTAT worked on "Deliverance I", 400 lbf thrust N2O-Paraffin Hybrid rocket designed to 20,000 ft. In 2016 UTAT worked on "Deliverance II", 600 lbf thrust N2O-Paraffin Hybrid rocket, designed to 23,000 ft optimizing on the design of Deliverance I. Starting in 2017 UTAT has undertaken its most ambitious project yet, Defiance, a 1500 lbf thrust N2O-Paraffin Hybrid rocket designed to break Canadian High Power altitude record of 13.4 km, with a rocket capable of a target apogee of 18.3km. The team has stated that within the next few years it hopes to develop a rocket capable of reaching space.

1.2 Objectives

This section summarizes the design objectives of this project, and are divided into 5 major categories: Functionality, Safety, Manufacturability, Optimization and Environment.

The objectives are ranked into three categories of importance. The "must have" objectives are those that are absolutely necessary to the success of the project. The "should have" objectives are secondary objectives that the team will aim for, but might be able to fulfill due to lack of

resource or other unforeseen circumstances. The “nice to have” objectives are extra analysis that the team will complete given the right resource and opportunity.

The objectives are listed in Table 1.1 and an evaluation of the design against each of the objective will be conducted in Section 12.

1.3 Design Challenges

Despite the benefits of aerospike nozzles, there are two specific challenges which have kept their inclusion in modern rocketry less prolific than one would expect. The first obstacle is the design of a cooling system capable of cooling the nozzle contour. As the nozzle contour resides directly within the exhaust plume, it is required to withstand combustion products moving at extremely high speeds and temperatures of up to approximately 2600K. Very few materials can withstand this amount of heat transfer – with a notable exception being graphite for at least a few seconds – without some form of active cooling. In addition, aerospike nozzles pose a mechanical challenge given that the plug portion of the nozzle must be suspended in the middle of the exhaust plume. Both of these technical challenges are addressed in more detail in future sections.

TABLE 1.1: Aerospike nozzle design objectives and metrics

	Objectives	Metrics
Functionality	1.1 Must be able to expand and accelerate combustion gases	-Thrust
	1.2 Must be able to be implemented in a future UTAT hybrid rocket engine without sweeping overarching design changes	-Nozzle efficiency
	1.3 Must be reusable to the extent of an average converging diverging nozzle	-Throat erosion rate
Safety	2.1 Must identify and reduce all hazards: -Nitrous oxide and carbon dioxide -Pressurized vessels and pipes -High temperature equipment and open flames	-HAZOP analysis -Factor of safety
Manufacturability	3.1 Should design nozzle with ease of manufacturing in mind	-Cost
	3.2 Should minimize cost of all testing components including compressed gas tanks, test stand, piping, etc	-Lead time
Optimization	4.1 Nice to have accurate modeling of the flow parameters around nozzle given current software capabilities	-Nozzle efficiency
	4.2 Should optimize nozzle design parameters using established optimization methods	
	4.3 Should evaluate the model's accuracy given testing results and incorporate testing results into the design	
	4.4 Nice to compare performance of an aerospike nozzle to that of a bell nozzle on the same engine	
	4.5 Nice to determine the scalability range of the nozzle designed	
Environment	5.1 Should reduce the environmental impact of an aerospike engine's life cycle from manufacturing to testing	-Greenhouse Gases Equivalent -Cumulative Energy Demand

Chapter 2

Design Process Overview

In this report, the design process of an aerospike nozzle for a test stand application will be outlined in detail. The design of a lab scale aeospike nozzle will be used as an example to guide the reader through the design process.

This section provides an overview of the design process. The overview flowchart is shown in Figure 2.1. The design process starts with the performance requirements and ends with the final mechanical design.

The engine parameters are determined based on the engine's performance requirements. In this case, the test stand engine parameters are determined based on the scaling analysis of the new UTAT rocket, Record Breaker. Using the engine parameters, the nozzle contour and combustion gas properties are then computed. A cooling analysis is then performed assuming that the nozzle will be actively cooled. The nozzle parameters and cooling requirement are then fed to an optimization algorithm. With the optimized nozzle contour, a cooling strategy is chosen and the mechanical components of the nozzle is designed. The team would then work with machine shops to finalize a design that could be manufactured, and if necessary, make modification to the applicable engine and nozzle parameters.

Each step outlined in the flowchart is explained in detail in Sections 3.0 - 8.0.

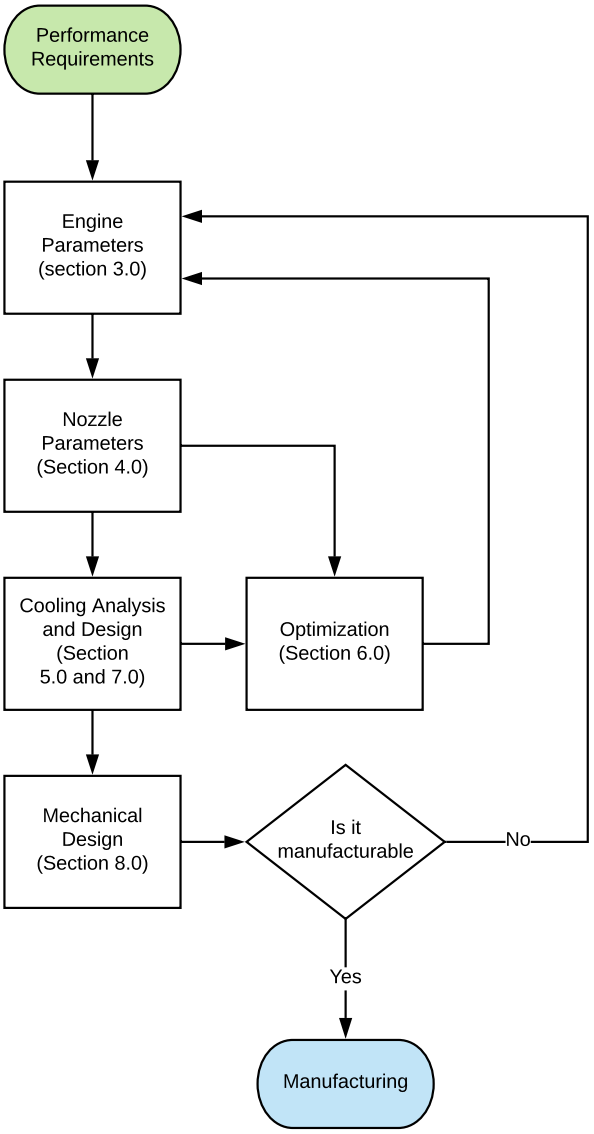

FIGURE 2.1: Aerospike nozzle design process overview

Chapter 3

Requirements and Engine Parameters

The design process summarized can be seen in the flowchart in Figure 3.1. The design process ultimately yielded the parameters summarized in Appendix A.

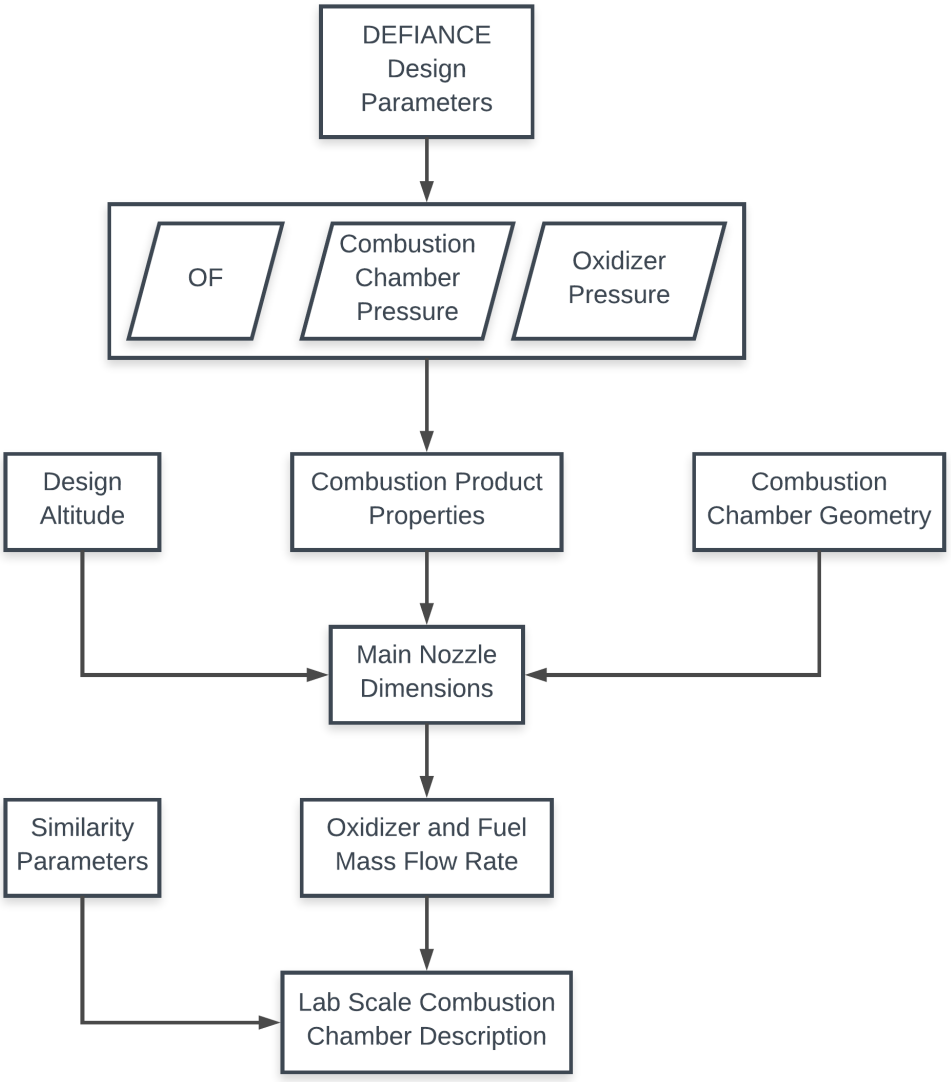

FIGURE 3.1: Design Flowchart for Lab Scale Combustion Chamber

An aerospike nozzle cannot be designed without considering the broader system it will be implemented in. This section will outline the high level system requirements which will be used to guide the nozzle design as well as the cooling system design.

An aerospike nozzle has never been attempted by UTAT previously, as such it will require validation through hot fire testing in order to characterize its performance and to address any issues which may potentially arise. The nozzle therefore needs to be designed around a propulsion system, the obvious choice for this is "Defiance", the rocket that UTAT is currently designing.

Defiance, however is not a suitable choice for this project. Defiance is a high thrust engine designed for a high apogee. The oxidizer mass flow rate required by defiance is 2.8 kg/s, and for a full engine test it requires a total of 24.8 kg of nitrous oxide. In addition to this, the oxidizer tank that is currently in development for defiance is over 3 metres long, and the required auxiliary testing equipment, personnel, and time required to run a single engine test makes Defiance an unfit target for current testing. In addition to this, the manufacturing of Defiance, and its test stand is not scheduled to be completed for many months.

An effective alternative is to employ similarity parameters in order to design a small-scale model of Defiance. The small-scale rocket, henceforth referred to as "Lab Scale Model", would maintain the same internal combustion kinetics as Defiance, in this way it could serve to simultaneously validate the aerospike nozzle in realistic operating conditions and even assist in the development of Defiance through the gathering of operating data to verify key design parameters[4]. In addition, the creation of a lab scale model is highly desired by UTAT as it would help in development of current and proposed projects, primarily, complete characterization of N2O injector elements, and effect of fuel core regression as a function of differing fuel core additives. In addition, the physical compactness of a lab scale rocket would significantly reduce costs per test, as less oxidizer would be required, would reduce manufacturing costs due to parts not being as large, and set up, test and turn around time between engine tests would all decrease significantly.

The quintessential work on hybrid rocket similarity analysis was laid out by Gany would who would go on to revise, improve and summarize his findings. Gany laid out the following three main parameters for the design of a small scale system capable of simulating a large scale system [4].

1. Geometric similarity
2. Identical propellants
3. Scaled oxidizer mass flow rate proportional to port diameter

The second similarity parameter is the most high level and can be fulfilled by maintaining the fuel and oxidizer combination to that which UTAT has built all its past rockets with, paraffin as the fuel and nitrous oxide as the oxidizer. The oxidizer to fuel ratio (OF ratio) would need to be maintained although the quantities of fuel and oxidizer can be scaled accordingly. As such an OF ratio of 4.5 is used. A more in depth discussion of OF ratio is to follow.

A fourth similarity parameter exists which suggests a constant value of the product of pressure and port diameter, however Gany states that this parameter can be omitted if the following three conditions hold.

- The third similarity parameter is met
- Combustion pressure is sufficiently high, at least 25 bar
- A post-combustor is used

The reason for being able to effectively ignore this 4^{th} similarity parameter is because physical, not chemical, aspects dominate hybrid combustion processes. In order to meet these conditions, a sufficiently high chamber pressure of 3102 kPa (450 psi) is used. This chamber pressure was chosen as it corresponds to the chamber pressure of Defiance. An identical chamber pressure is helpful as it allows for structural validation of the nozzle under the same operating pressures. Since upstream oxidizer pressure is chosen based on general guidelines of a 20 percent pressure drop across the injector, this allows us to choose the same upstream pressure of 700 psi as Defiance. The upstream and downstream pressure combination has the added benefit of facilitating tests necessary by the additional projects such as the nitrous oxide injector element characterization.

The optimal OF ratio is a function of the propellant combination and combustion pressure. Using a chemical equilibrium analysis such as NASA CEA, one can determine, using specific impulse, a measure of how effectively a rocket uses propellant, that the optimal OF ratio for the proposed combination of nitrous Oxide and Paraffin, at a combustion pressure of 450 psi is approximately 5.5. In practice, most rocket engines run with a OF ratio lower than stoichiometric. This leads to three important benefits,

- A fuel rich design will insure all the oxidizer is completely consumed within the combustion chamber. Forcing all the combustion to occur within the combustion chamber leads to a shorter post-combustor length, which translates to a smaller length combustion chamber. A post-combustor being an empty area between the fuel core and the nozzle whose sole purpose is to increase mixing time. This reduces weight leading to aerodynamic savings in flight and reduces physical length leading to economic savings [5] [6].

- It has been shown that throat erosion rate is strongly reduced for fuel rich mixtures. This is because oxidizer rich mixtures have an increased presence of molecular oxygen which will cause an oxidizing reaction of the nozzle throat material, leading to heat release increasing the temperature at the walls, this leads to erosion acceleration at the throat of the nozzle leading to a decreased effective life span for the nozzle. In contrast, fuel rich mixtures will have a lower flame temperature and no oxidizing agents leading to maximum nozzle life [7].

- In practice, a lower OF ratio actually leads to a higher specific impulse. This is because lighter weight molecules do not react in the combustion reaction leading to a mixture with a lower average weight [5]. The lower weight of the resulting gases means the gases can be accelerated to a higher speed as seen by the molecular weight term MW in the denominator of equation 3.1, the ideal exhaust velocity equation. This leads to an increase in the impulsive contribution of the thrust equation, equation 3.2.

$$V_e = \sqrt{\left(\frac{2\gamma}{\gamma-1}\right)\left(\frac{R*T_c}{MW}\right)\left(1-\left(\frac{P_e}{P_{cc}}\right)^{\frac{\gamma-1}{\gamma}}\right)} \tag{3.1}$$

$$F = \dot{m}V_e + (P_e - P_{atm})A_e \tag{3.2}$$

Characteristics of the combustion products, for the aforementioned propellant and engine parameters, were determined using NASA's Chemical Equilibrium with Applications (CEA) code [8]. Equilibrium conditions were used which assume chemical equilibrium, as opposed to frozen flow which assume products frozen at one point. The results are presented in 3.1

TABLE 3.1: Characteristic of combustion product assuming chemical equilibrium

	Chamber	Throat	Exit
P_∞/P	1.0000	1.8046	36.697
$T(K)$	2831.47	2527.09	1322.73
$\rho(\frac{kg}{cu})$	3.0461	1.8958	1.7840-1
$c_p(\frac{kJ}{kgK})$	2.0146	1.8364	1.6146
M	0.000	1.000	2.915

Using the combustion product characteristics the characteristic velocity can be readily calculated through equation 3.3,

$$c^* = \frac{\sqrt{\gamma R T_0}}{\gamma\sqrt{[2/(\gamma+1)]^{\frac{(\gamma+1)}{(\gamma-1)}}}} \tag{3.3}$$

Characteristic velocity, a function of the propellant combination, is then multiplied by a combustion efficiency factor, to account for incomplete combustion of all the propellants. In this case 90% was used to be conservative.

$$c_{\eta}^{*} = \eta c^{*} \tag{3.4}$$

Optimum expansion for nozzle flow occurs when the flow is discharged from the nozzle at a pressure equal to local atmospheric pressure. In traditional converging-diverging or bell nozzles, optimum expansion occurs at a single altitude, because the constant exit area dictates that the nozzle has a constant exit pressure. For these nozzles the expansion ratio ϵ is often chosen such that the nozzle perfectly expands at 2/3 of the rocket burnout altitude [5]. Below this altitude, the nozzle flow is over-expanded and above this altitude the nozzle flow is under-expanded. The main benefit of aerospike nozzles is the altitude adaptation capabilities. An aerospike nozzle operating in an over-expansion regime will have flow expansion approximately equal to ideal [3]. However, when an aerospike nozzle operates in an under-expansion regime it will behave as a conventional nozzle and will lose its altitude adaptation capabilities [3]. To ensure the nozzle always operates in an over-expansion regime, a pressure design ratio PR_d (defined as the ratio of chamber pressure P_{cc} to local atmospheric pressure P_{atm}) sufficiently greater than its maximum operating condition is chosen. With this in mind a pressure design ratio of 50 is chosen which is consistent with an altitude of 3.3 km. This is the approximate burn out altitude for a N2O-Paraffin rocket, similar to Defiance but with a slightly higher target altitude of 20.1 km. Although this exact nozzle could never see such a target altitude, the corresponding pressure design ratio was chosen to enforce similarity between Defiance and the lab scale model.

The nozzle exit Mach number was then calculated knowing the pressure design ratio,

$$M_e = \sqrt{\left(\frac{2}{\gamma - 1}\right)\left(\left(\frac{P_{cc}}{P_{atm}}\right)^{\frac{\gamma-1}{1}} - 1\right)} \tag{3.5}$$

With this, the expansion ratio of the nozzle was calculated,

$$\epsilon = \frac{1}{M_e}\sqrt{\left[\left(\frac{2}{\gamma+1}\right)\left(1 + \frac{\gamma-1}{2}M_e^2\right)\right]^{\frac{\gamma+1}{\gamma-1}}} \tag{3.6}$$

An NPS 3 SCH 40 pipe was chosen as the combustion chamber. The nozzle exit area is chosen geometrically to be equal to the combustion chamber inner diameter. This then yields an optimum throat area. In order to fulfill the nozzle requirement for chocked flow at the throat, the necessary propellant mass flow rate can be calculated through,

$$\dot{m} = \frac{p_{cc} A_t}{c^*} \tag{3.7}$$

Oxidizer and fuel mass flow rate is then calculated through knowing the total propellant mass flow rate and OF ratio.

Once oxidizer mass flow rate was established, the aforementioned similarity parameters were then used, along with the current Defiance parameters [9], in order to determine a scaled value for the inner port diameter of the fuel core and length of the fuel core followed from this result.

Chapter 4

Contour Design and Initial Analysis

The nozzle contour is important as it determines the velocity profile of the exhaust gas over the designed altitude range. Taking data computed in the engine parameters section, an initial nozzle contour as well as exhaust gas properties can be determined. A flow chart giving an overview of this stage of the design process is shown in Figure 4.1 below:

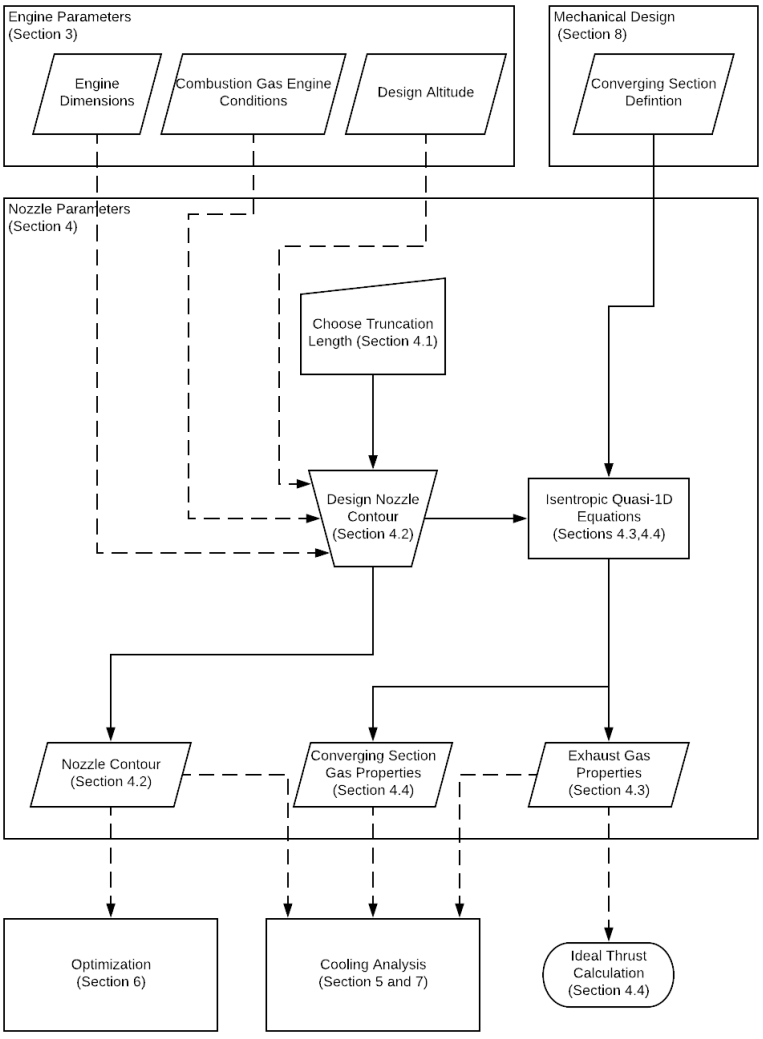

FIGURE 4.1: Nozzle Parameter Process Overview

4.1 Choose Truncation Length

Aerospike nozzles are typically truncated from their full ideal length to reduce both cooling and machining requirements. Aerospike nozzles are able to be greatly truncated due to the formation of an open-wake at the base of the nozzle that acts similarly to a physical full length nozzle base[3]. This open-wake formation drastically improves the thrust output of a truncated nozzle than what would be estimated under the assumption of quasi-one-dimensional isentropic flow. A table summarizing nozzle efficiency as a function of truncation length is shown below in Table 4.1:

TABLE 4.1: Table of Nozzle Efficiency vs. Truncation Length at $PR = 30$ [3]

% Length	η	C_F
10	0.76	1.07
20	0.86	1.09
100	0.982	1.40

Due to the challenges faced as a result of massive cooling requirements, a more greatly truncated nozzle was chosen. In specific, a 20% truncation length offers a reasonable trade off between efficiency and being more easily cooled and machined. Figure 4.2 shows the diminishing returns when the nozzle is truncated to less than 20% of its original length.

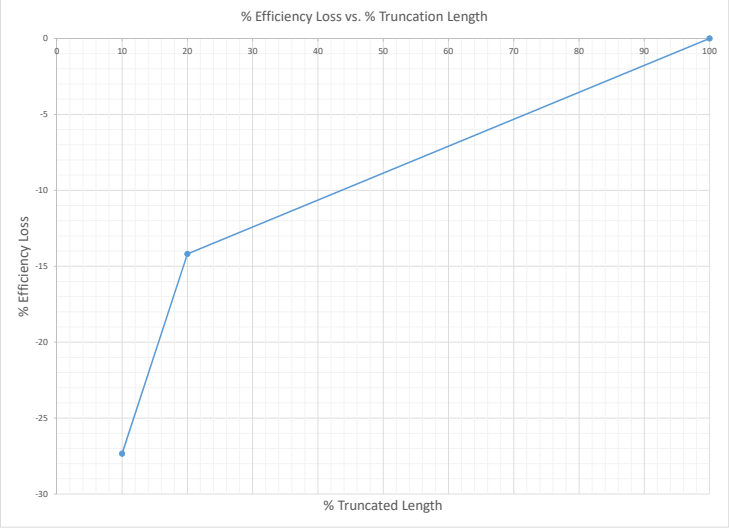

FIGURE 4.2: Efficiency Loss vs Truncated Length

In particular, truncating the nozzle from to 20% of its original length, results in a lost of 14% efficiency. Truncating the nozzle to 10% results in an efficiency loss of 27%. Having chosen a truncation length, the diverging section of the nozzle contour can be designed.

4.2 Design Nozzle Contour

Having chosen both a truncation length and design altitude, it is possible to design the diverging portion of the nozzle contour. For this purpose, the methods of Lee and Angelino stand out for their proliferation in contour design [3] [10] [11]. Lee chooses to step backwards through the expansion fan starting at the nozzle base using the stream function to define the contour [12]. Angelino defines the contour by expanding the combustion gas around the nozzle lip matching the characteristic line length with quasi-one-dimensional area relations [1]. Both methods, based on the same assumption of a centred Prandtl-Meyer expansion about the nozzle lip, produce functionally similar nozzle contours. For our purposes, Angelino's method was chosen due to the relative simplicity required for its implementation; a brief description of this method is given below.

First, consider the nozzle diagram given by Angelino [1] below:

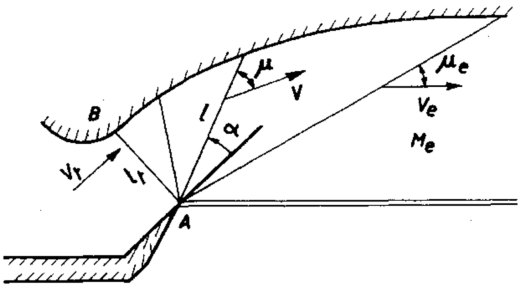

FIGURE 4.3: Aerospike Nozzle Diagram from Angelino [1]

Letting l be the characteristic line length and l_t be the characteristic line length at the throat, the continuity equation can be written as:

$$\frac{l}{l_t} = \frac{A}{A_t}\left(\frac{1}{\sin\mu}\right) = \epsilon M \tag{4.1}$$

Furthermore, if we let α be the angle of the characteristic line with respect to the combustion gas direction of travel at the throat we find the following geometric relation:

$$\alpha = \mu - \nu \tag{4.2}$$

The equation for an ideal nozzle contour point is now fully defined by the parameterization of equations 4.1 and 4.2 by the mach number. In short, the equation for our ideal plug nozzle can be found by solving the following equations:

$$\frac{l}{l_t} = M\epsilon(M) \tag{4.3}$$

$$\alpha = \mu(M) - \nu(M) \tag{4.4}$$

4.3 Exhaust Gas 1-D Flow Properties and Ideal Thrust

At this point in the nozzle parameter section of the design process, a nozzle contour based on isentropic quasi-one-dimensional flow has been determined and the mach number in its wake is known. Figure 4.4 below shows the mach number contour plot under these assumptions for our lab scale nozzle. Note that Figure 4.4 calculates the exhaust gas properties for the full length nozzle as opposed to the truncated nozzle. This is because the full length nozzle contour provides a better approximation for the nozzle under the assumptions of isentropic quasi-one-dimensional flow [3].

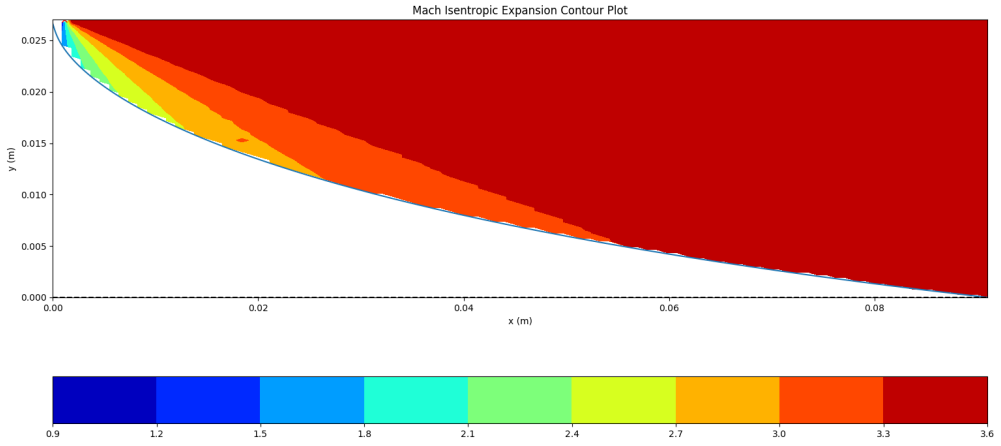

FIGURE 4.4: Mach Contour Plot for 1-D Isentropic Flow

As we know both the mach number at every point in the combustion exhaust and the chamber conditions, we can estimate the other flow properties of note from isentropic stagnation equations [13].

$$1 + \frac{\gamma - 1}{2}M^2 = \frac{T_c}{T} = \left(\frac{p_c}{p}\right)^{\frac{\gamma-1}{\gamma}} = \left(\frac{\rho_c}{\rho}\right)^{\gamma-1} \tag{4.5}$$

Figure 4.5 below plots the temperature, pressure, and density for our lab scale nozzle under the aforementioned assumptions.

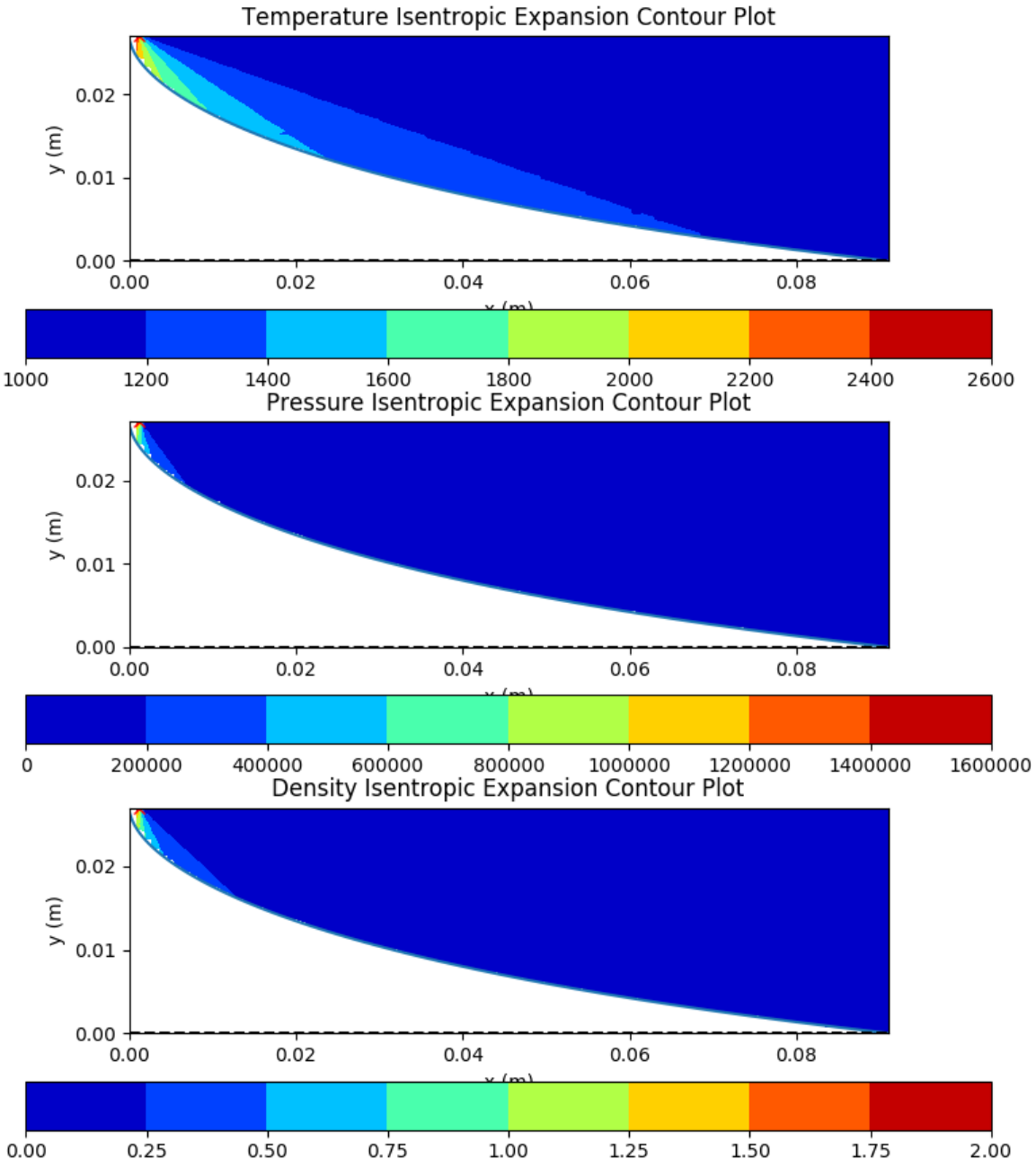

FIGURE 4.5: Mach Contour Plot for 1-D Isentropic Flow

From these fundamental flow properties, it is possible to estimate the ideal thrust output of the nozzle contour [13].

$$T = \dot{m}_e V_e + (p_e - p_\infty) A_e \tag{4.6}$$

For our lab scale nozzle, we found the ideal thrust to be approximately 120N.

The nozzle contour and exhaust gas properties are passed to the cooling section, while the nozzle contour is passed to the optimization section. The ideal thrust calculation is used as an upper bound for our engine's force output.

4.4 Converging Section Gas Properties

The converging section geometry is primarily determined by mechanical constraints. As Anderson notes, the definition of contour of the converging section "can be somewhat arbitrary (within reason)" [13]. As long as the converging section of the nozzle smoothly transitions from the chamber conditions to choked at the nozzle throat, the nozzle will behave in a predictable manner [13].

Furthermore, because we know the conditions at the nozzle throat, the gas conditions within the converging section of the contour can be determined using quasi-one-dimensional isentropic area relations [13].

$$\frac{T_2}{T_1} = \left(\frac{p_2}{p_1}\right)^{\frac{\gamma-1}{\gamma}} = \left(\frac{\rho_2}{\rho_1}\right)^{\gamma-1} = \frac{1+\frac{\gamma-1}{2}M_1^2}{1+\frac{\gamma-1}{2}M_2^2} \tag{4.7}$$

$$\frac{A_2 M_2}{A_1 M_1} = \left(\frac{2+(\gamma-1)M_2}{2+(\gamma-1)M_1^2}\right)^{\frac{\gamma+1}{2(\gamma-1)}} \tag{4.8}$$

It is important to note that because the converging section is driven by a static source on one side and is choked on the other, this system is over-determined and cannot be simply solved by equations 4.7 and 4.8. Having said this, these equations do still provide a reasonable estimate for flow conditions for over-determined systems in the case that area changes are gradual. These converging section flow properties, along with the nozzle contour and diverging section flow properties, are passed to the cooling section for the purpose of cooling analysis.

Chapter 5

Cooling System Analysis

Managing the high heat flux of an aerospike nozzle is a major design challenge. A rocket nozzle will experience high heat load at the throat where flame temperature can reach up to 2000 to 3000 K. In addition, the surface area of an aerospike nozzle at the throat is significantly larger than a traditional bell nozzle of the same expansion ratio. Thus, the tolerable erosion rate on a traditional nozzle may pose significant enlargement of the throat area on an aerospike nozzle. This can lead to decrease in performance or even nozzle failure [14]. Thus, it is crucial to design a reliable cooling system.

Only a few type of materials can maintain structural integrity at a flame temperature of 2000 to 3000 K. Examples are ceramics, composites and other exotic materials. Ceramics such as graphite can experience high erosion rate and composite material enforced with silica fiber can be costly to manufacture. If active cooling were to be used, then the nozzle can be manufactured using metals which are more versatile and readily available than other exotic materials. Thus, the first step in designing the cooling system is to evaluate the possibility of using active cooling to manage the high heat load of the nozzle.

The coolant used in this case will be the oxidizer, nitrous oxide (N_2O) wguke nozzle will be made out of copper. Nitrous oxide has been proven to be a suitable coolant in regenerative and dump cooling applications for rocket nozzles [15] [16]. Copper has been chosen due to its high heat conductivity and malleability.

The detail design process flowchart for cooling analysis is shown in Figure 5.1. This section outline the first part of the cooling analysis, which includes heat flux, coolant flow-rate and coolant pressure drop calculations.

5.1 Heat Flux Prediction

An active cooling system can be used to maintain the nozzle at a steady state temperature. This is done by flowing a coolant through the inside of the nozzle, effectively cooling the nozzle wall. The qualitative temperature variation across the nozzle wall is shown in Figure 5.2.

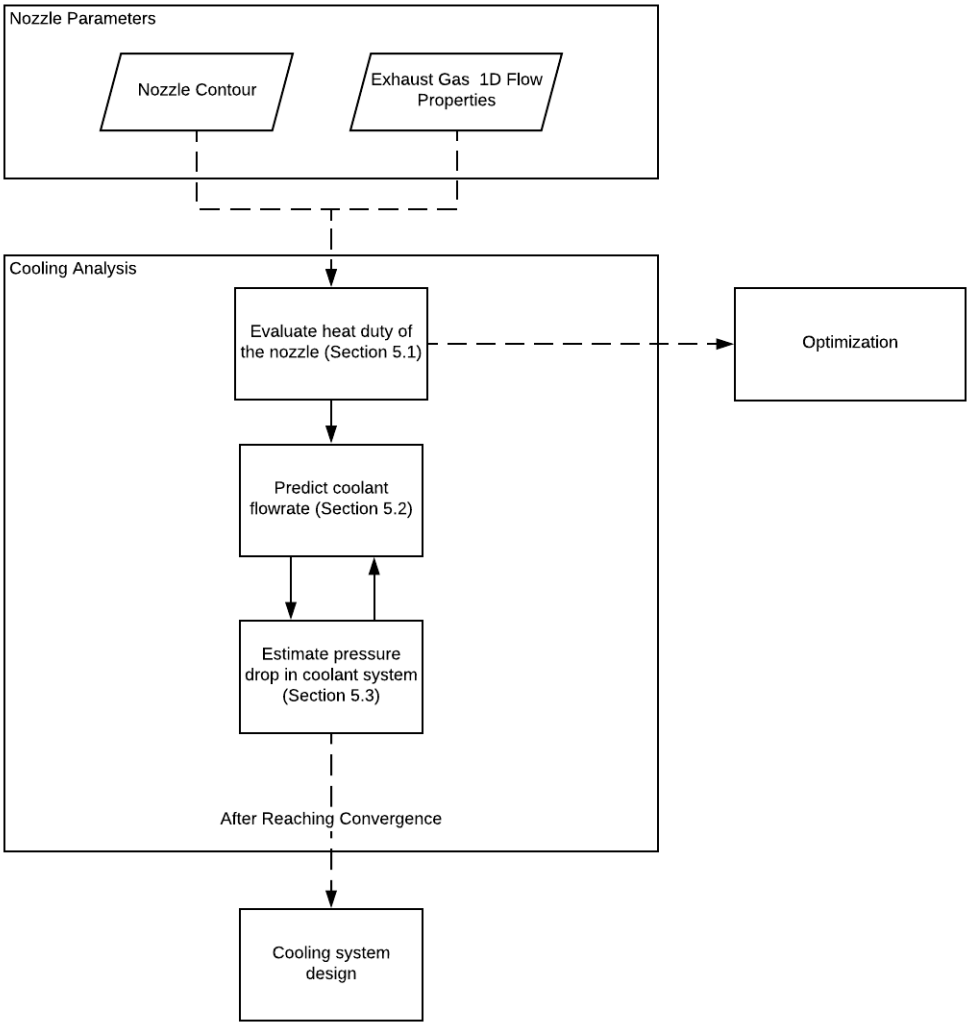

FIGURE 5.1: Cooling analysis process overview

In this scenario, the nozzle temperature must be maintained below 700 K. This temperature is selected based on reference [16], where the strength of the copper at 700 K is about 65-75% of its strength at room temperature, which is an acceptable level for short term rocket applications. The heat flux prediction calculation in this case will target a constant nozzle surface temperature of 400 K to yield a conservative prediction.

In this fuel oxidizer system, the dominating mode of heat transfer is convection, and radiative heat transfer is only significant in solid propellant systems [17]. To determine the heat flux, it is critical to determine the convective heat transfer coefficient on the combustion gas side, h_g, in the equation 5.1 below.

$$q_{conv} = h_g(T_{\infty g} - T_{wg}) \tag{5.1}$$

Semi-empirical formulas developed by Mayer is used to evaluate the convective heat transfer coefficient [2]. Mayer's method is more applicable to external expansion nozzles compared to

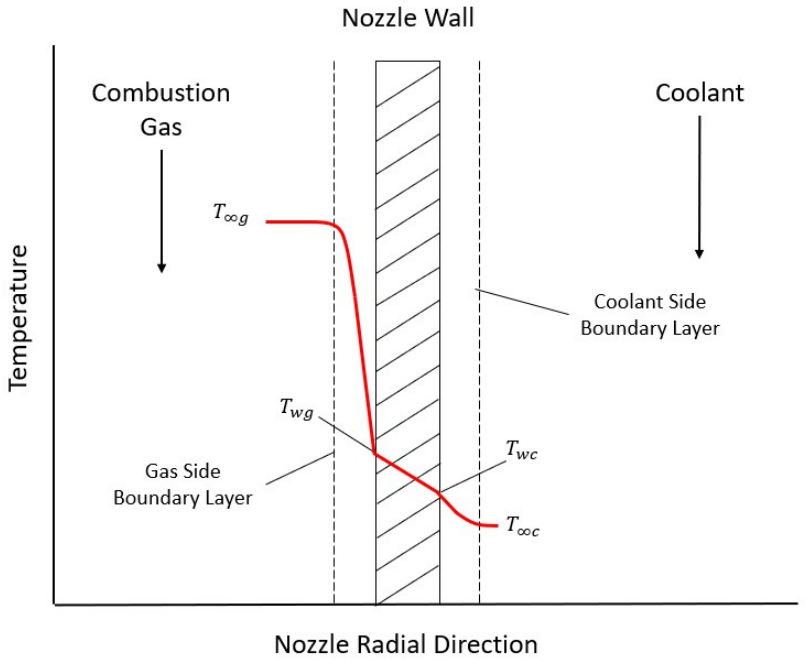

FIGURE 5.2: Temperature profile across nozzle wall

the more commonly used Bartz's method [18]. It was also found through several calculation iterations that Mayer's method gives an overall high heat flux than Bartz's method, resulting in a more Conservative heat flux prediction.

Mayer does not assume fully developed flow along the nozzle wall, but instead, conduct a energy balance on the boundary layer as shown in Figure 5.3. The main assumptions of Mayer's method are:

1. Isentropic combustion gas flow
2. Boundary surface at constant temperature (steady state).

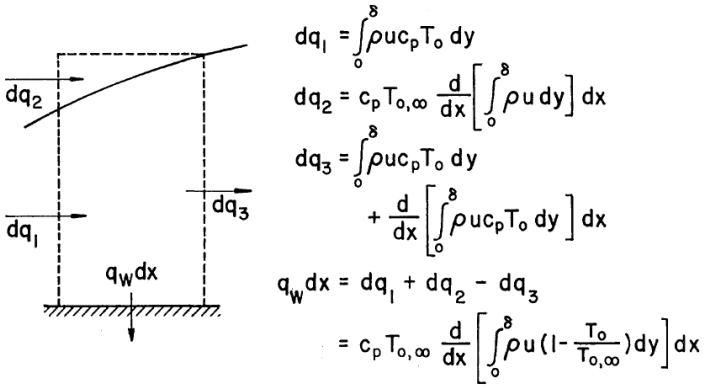

FIGURE 5.3: Sketch of control volume for driving energy-integral equation for boundary layer elements of width dx [2]

Using the energy balance, the convective heat transfer coefficient for a flat plate can be solved for by taking the integral across the curvilinear surface, s, as shown in equation 5.2.

$$h_2(s) = \frac{0.0296\beta^{5/4}Pr^{-2/3}\rho_\infty C_{p,\infty}U_\infty}{(\int_0^s \beta^{5/4}\rho U_\infty \mu_\infty^{-1} ds)^{-1/5}} \tag{5.2}$$

A geometry transformation is then used to to compute the heat transfer coefficient for an asymmetric nozzle, shown in equation 5.3. The total heat flux can then be computed by taking the integral across the length of the nozzle using equation 5.1.

$$h_3(s) = h_2(s)\left[\frac{r^{5/4}\int_0^s \beta^{5/4}\rho_\infty U_\infty \mu_\infty^{-1} ds}{\int_0^s (r\beta)^{5/4}\rho U_\infty \mu_\infty^{-1} ds}\right]^{1/5} \tag{5.3}$$

The input to Mayer's method are the nozzle contour, exhaust gas 1D flow properties and exhaust gas properties from NASA CEA. The detail list of input parameters are shown in Table 5.2 and 5.1, and the values for the test stand nozzle are listed as appropriate. Because Mayer's method was developed using constant in the British unit system, all parameters were converted to the British units. For the 1D gas properties, sufficiently small step size is needed as Mayer's method depends on numerical integration. For a given nozzle, the step size can be decreased until no significant difference can be seen in the resulting heat flux. 1850 nodes were used in total for the test stand nozzle. The detail calculation procedure can be found in Mayer's paper [2].

TABLE 5.1: Exhaust gas properties from NASA CEA

Parameter	Value	Units
Pr	0.56	
C_p	0.412	BTU/lb R
γ	1.27	
c	5.24E-07	lb/ft s
w	0.548	

TABLE 5.2: Nozzle contour and 1D exhaust gas flow properties

Node	x (in)	s (in)	r (in)	M	U (ft/s)	ρ (lb/ft^3)	$T_{\infty g}(R)$
1	0	0	0.083	0.34	406	0.199	5028
2	0.0015	0.083	0.34	0.339	405	0.199	5028
⋮	⋮	⋮	⋮	⋮	⋮	⋮	⋮
1850	1.87	0.183	0.046	2.82	2432	0.013	2625

The resulting total heat flux of the test stand nozzle is 41.9 kW which includes both the converging and diverging sections. The heat transfer coefficient along the nozzle is shown in Figure 5.4, and it can be observed that the heat transfer coefficient is highest at the throat. These values correspond to the one computed using ANSYS FLUENT® in reference [19].

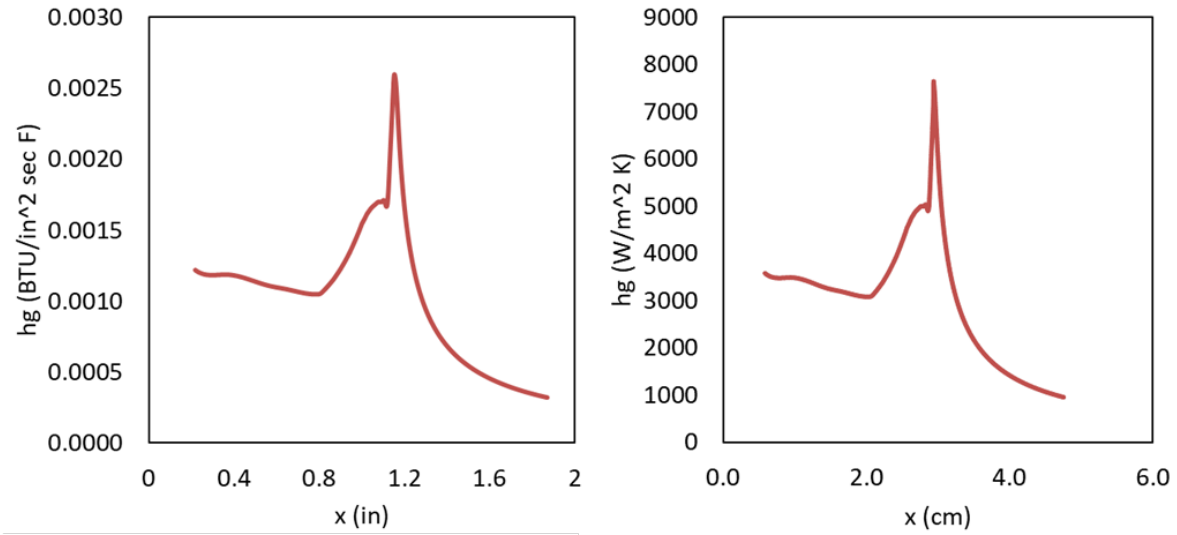

FIGURE 5.4: Convective heat transfer coefficient along the nozzle length in British units (left) and Metric units (right)

5.2 Coolant Flow-rate Prediction

An important step in designing an active cooling system is the sizing of the coolant flow rate. The representative diagram of the dump cooling and active cooling system is shown in Figure 5.5. In the regenerative cooling system, the oxidizer is first routed to the nozzle as a coolant and then directed into the combustion chamber. Whereas in the dump cooling system, the two nitrous oxide lines are separate and the coolant is directly ejected out of the nozzle.

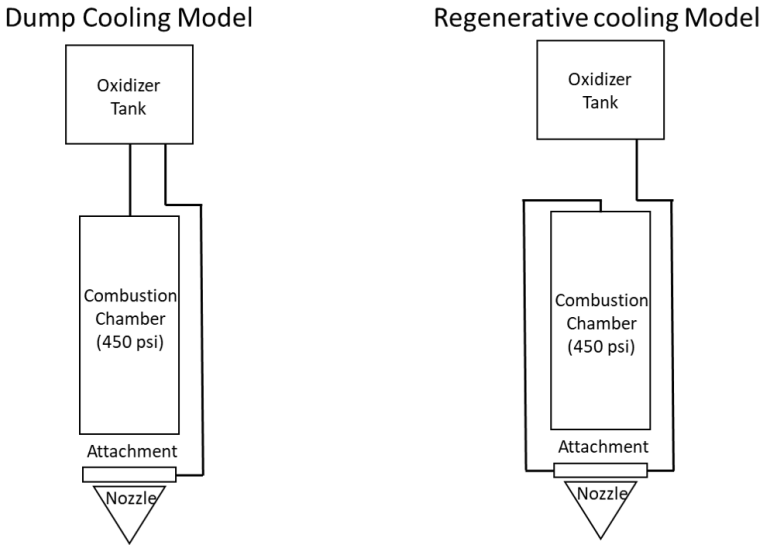

FIGURE 5.5: Dump cooling (left) and regenerative cooling (right) system diagrams

For the dump cooling system, the coolant flow rate is determined independent of the oxidizer flow rate. On the other hand, the regenerative cooling system, the coolant is recycled and the

analysis focuses on determining if the oxidizer flow rate has enough cooling capacity. If the cooling capacity is not sufficient, then the engine parameters will need to be updated. In most cases, it is satisfactory.

For both systems, an iterative calculation approach is taken. The coolant flow rate depends on the pressure drop of the system. The pressure drop, in turn, depends on the coolant flow rate. So an iterative calculation is needed until both side converges. The pressure drop calculation is outlined in section 5.3.

All properties of nitrous oxide are are based on the NIST (National Institute of Standards and Technology) Thermophysical Properties of Fluid Systems implemented through the CoolProp® codes. Specifically, the coefficient for the equations of state were taken from Lemmon's paper in reference [20].

The nitrous oxide in this case is in its sub-critical state, meaning its latent heat of vaporization is available for cooling. However, nitrous oxide in its vapour phase may undergo exothermic decomposition upon heating. This run away reaction can lead to catastrophic failure and pose a significant safety concern. Normally, this reaction occurs at temperatures above 520 C, but the presence of impurities can lower this temperature to 200 C [21]. As such, an nozzle exit quality of 0.4 is chosen to size the coolant flow rate. This is due to a higher vapour to liquid ratio may cause dry-out and overheating of nitrous oxide vapour [22].

The pressure enthalpy curve of nitrous oxide is shown in Figure 5.6. The cooling capacity of nitrous oxide depends on the pressure it enters the nozzle. If an initial guess of 34.4 bar (500 psi) is used, then the cooling capacity will be 54.43 kg/kJ for a target exit quality of 0.4. The corresponding coolant flow rate can be calculated using equation 5.4 and is determined to be 0.77 kg/s. This method of calculation assumes that there is no pressure drop in the nozzle. Pressure drops in cooling channels will be further explored in section 7.2.

Upon iterative calculation, convergence is achieved where the coolant flow rate is 0.72 kg/s and the pressure at the nozzle is 38.3 bar (556 psi). The oxidizer flow rate for this system is 0.9 kg/s, meaning that this system is suitable for regenerative cooling. The possibility of regenerative cooling will be further explored in section 7.

$$\dot{m}_{coolant} = \frac{q_{conv}}{\Delta h_{vap}} \tag{5.4}$$

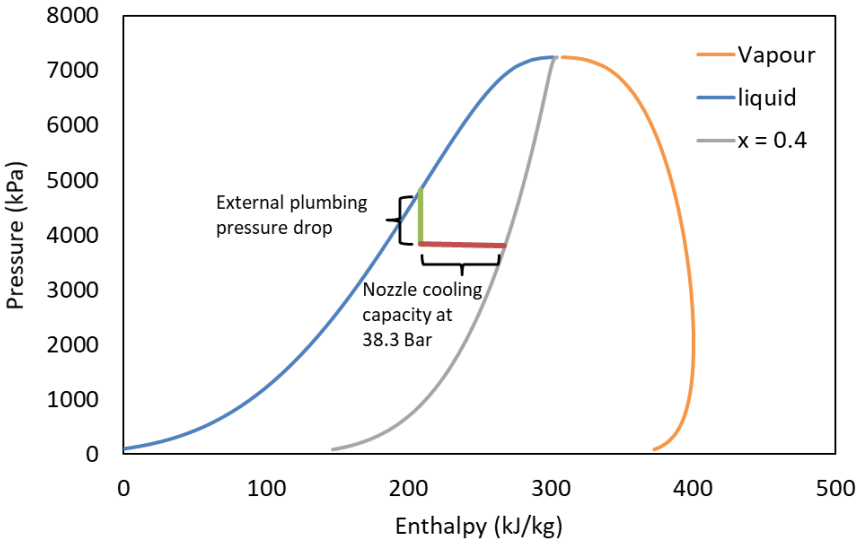

FIGURE 5.6: Pressure enthalpy graph of nitrous oxide

5.3 Pressure Drop Prediction

The process of determining the pressure drop on the system is iterative to calculate the coolant requirement and respective pressure drop on the system.

The following figure show cases the representative system in AspenPlus. The REFPROP method was employed to perform the calculations of two phased flow and model the behaviour of the liquid-vapor mixture throughout the pipe and fittings. It was assumed that the system is in steady state equilibrium between the vapor and liquid. The method of REFPROP in ASPEN-PLUS was chosen as it is based on the NIST Reference Fluid Thermodynamic and Transport Properties. It offers thermodynamic and transport properties of nitrous oxide, hydrocarbons, refrigerants and other industrially important fluids. For its thermodynamic properties, equations of stat explicit in Helmholtz energy, the modified Benedict- Webb-Rubin equation of state and an ECS (extended corresponding states) model is implemented [23].

The general procedure for determining pressure drop in the piping is as follows:

1. Determine the length of pipe required and number of fittings
2. Find the k (coefficient of resistance) for each fitting
3. Determine the pipe roughness factor based on metal used
4. Input values in Aspen Plus
5. Run through simulations and assess if the output pressure is acceptable

In the following example, this method was applied to the test stand. The system can be simplified into two pipe components on Aspen consisting of metal tubing, fittings, bends and valves that are specified in the set-up/configuration.

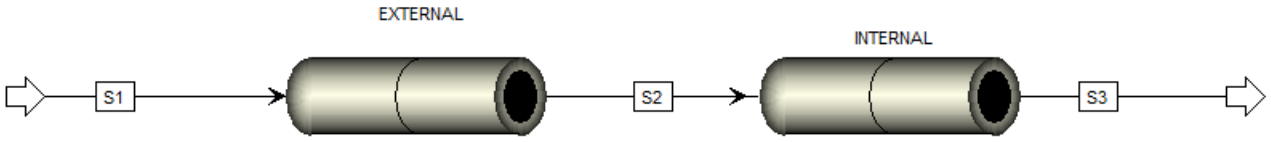

FIGURE 5.7: Aspen Plus Layout

In the figure, the external pipe represents a system with a 65 cm length pipe with a 1.0922 cm inner diameter, 1 gate valve, 2 90 degree elbows and a diameter reduction to 0.7 cm inner diameter. Two fittings and a gate valve were used with a respective K (coefficient of resistance) of 1.8. The internal pipe represents the small tubing that enters the nozzle.

To ensure a sufficient mass flow rate of nitrous being supplied to the nozzle, analysis of the pressure drop was conducted on the coolant line of the system. A temperature of 18 degrees C and pressure of 700 psi was used as the input for the desired mass flow rate of 0.72 kg/s.

The pressure at each segment of the pipe can be seen below in Figure 5.7. With the respective test stand configuration, 0.72kg/s of nitrous oxide can be supplied to the nozzle at a pressure of 556 psi.

The system was designed to avoid choking of the nitrous within the design restrictions of the coolant pipe diameter insert. The smaller scale nozzle faced more challenges with higher pressure drop along pipe constrictions and relatively larger flow rates. However scale-up of the system will decrease this impact and allow for the potential feasibility of regenerative cooling.

	Units	S1	S2	S3
Description				
From			EXTERNAL	INTERNAL
To		EXTERNAL	INTERNAL	
Stream Class		CONVEN	CONVEN	CONVEN
Maximum Relative Error				
Cost Flow	$/sec			
− MIXED Substream				
Phase		Liquid	Mixed	Mixed
Temperature	K	291.15	285.456	281.439
Pressure	psi	700.125	613.139	556.839

FIGURE 5.8: Stream Pressures

This method can be applied in the scale-up of the system to determine the pressure drop of larger test stands and rockets.

Chapter 6

Nozzle Parameters Optimization

Iterative computational optimization was identified by UTAT as an important development goal as the design process of the group continues to evolve. This section outlines two method for iterative optimization supported by computationally inexpensive algorithms. The framework provided below can be extended to optimize over a greater number of input parameters than was examined here with relative simplicity. Unfortunately, time constraints meant that these algorithms could not be implemented for the purpose of optimizing the lab scale engine.

6.1 Construction and Computation of Cost Function

For both optimization methods that will be discussed here, the first step is to construct a cost function parameterized by the design variables of interest. For the lab scale model, we chose to construct two different cost functions of varying complexity. The first cost function consists of weighted sum of the thrust and heat duty paramaterized by the design altitude and truncation amount. Letting C = the cost function, alt_d = the design altitude, and tr = the truncation amount this cost function is given in Equation 6.1 below.

$$C(alt_d, tr) = \alpha * thrust(alt_d, tr) + \beta * heatduty(alt_d, tr) \tag{6.1}$$

Where α and β are hyperparameters to be chosen by the individual performing the optimization. The second cost function we chose to explore again consisted of a weighted sum of the thrust and heat duty but was this time parameterized by the finite contour points. This cost function is given in Equation 6.2 below.

$$C(contour) = \alpha * thrust(contour) + \beta * heatduty(contour) \tag{6.2}$$

Where, again, α and β are hyperparameters and the contour is given by the spline interpolation of the points $(x_0, r_0, x_1, r_1, ..., x_n, r_n)$ with $(x_0 < x_1 < ... < x_n)$.
It is important to note that despite having relatively similar forms, the two cost functions are extremely different in nature. In specific, the cost function given by equation 6.1 has two input

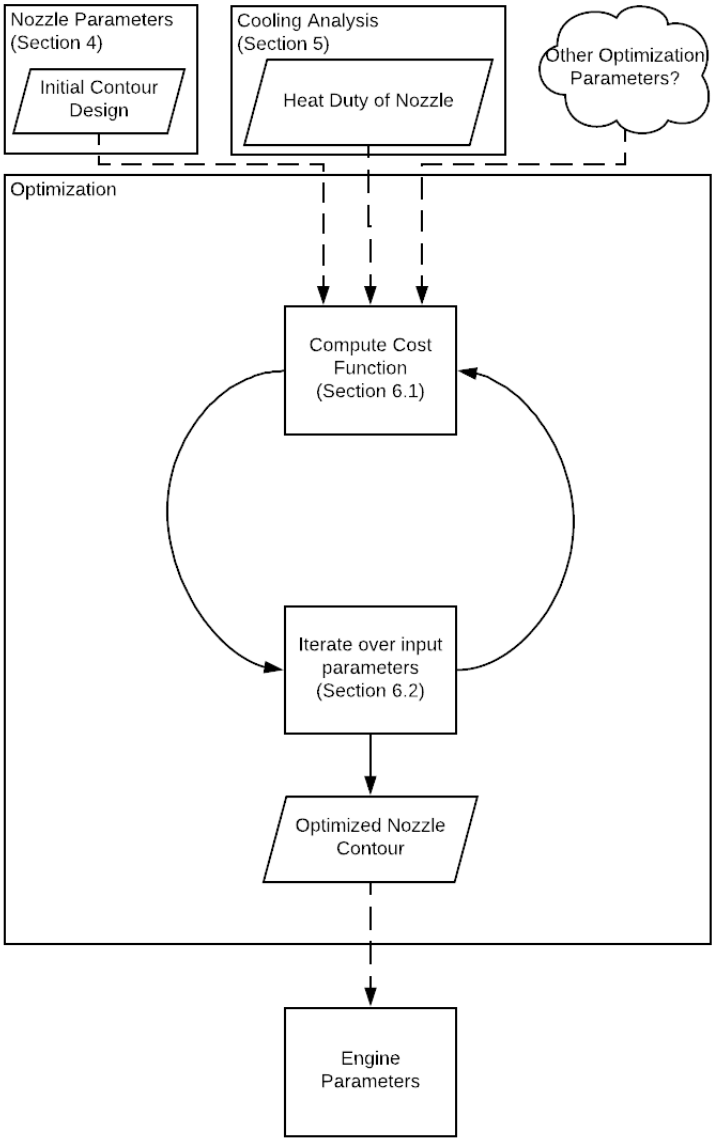

FIGURE 6.1: Optimization Process Flowchart

parameters while the cost function given by equation 6.2 has n input parameters; for our purposes n being on the order of 100 provided a fine enough resolution that its discretization was not noticeable.

Before moving forward, a brief discussion of the evaluation of the cost function is necessary. We have mentioned how to calculate the heat duty in Section 5.1. In order to predict how the thrust output will change with different contour shapes, a more accurate model will be required than what was employed in Section 4. Typically, a finite difference approach appears to be the natural choice for flow prediction. However, because we wish to employ an interactive method for minimizing the cost function, the computational cost of the finite difference approach makes

this method unfeasible. For this reason, we have implemented the method of characteristics by using three-dimensional irrotational equations of flow. As Anderson points out, for supersonic flow, the the method of characteristics can require far fewer mesh points than the finite difference method when aiming for the same accuracy in supersonic flow [13].The section to follow introduces the method of characteristics as well as providing some results we found with the method.

First, it should be repeated that we implemented the method of characteristics using the equations of three-dimensional irrotational equations of flow. In the broadest sense, the algorithm starts at a location where the flow properties are known and solves for the other flow properties by computing the intersection of constant property characteristic lines. This builds up a "characteristic mesh" where the flow properties are known at each intersecting point of the mesh [24].

An example characteristic mesh is shown in Figure 6.2

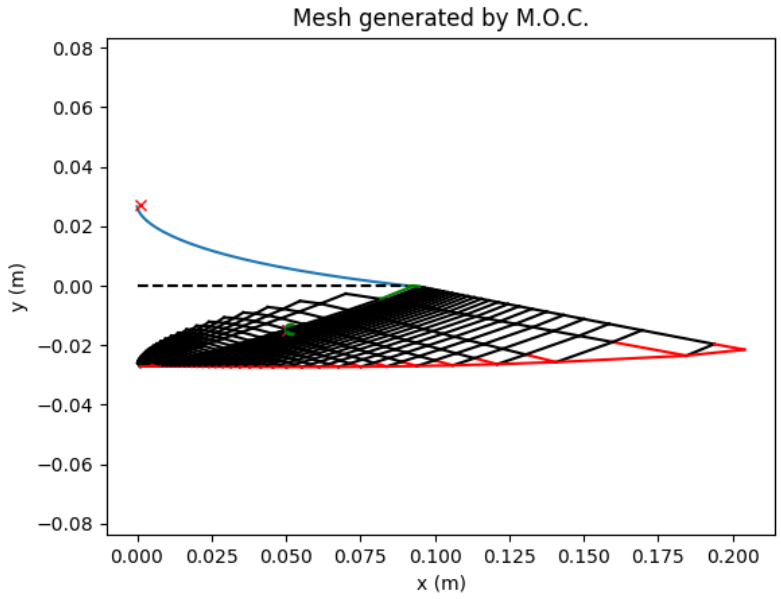

FIGURE 6.2: Characteristic Mesh Example

It should be noted that in Figure 6.2 only 30 expansion waves emanating from the nozzle throat were chosen to increase the clarity of the mesh. For estimating flow properties, approximately 120 expansion starting from the nozzle throat will be used.

A full description of the equations used in the fluid solver here can be found in *Comparisons of Experimental Free-Jet Boundaries with Theoretical Results Obtained with the Method of Characteristics* [24]. Using this algorithm, mach contour and vector velocity plots at both the design altitude (Figures 6.3 and 6.5) and at sea level (Figures 6.4 and 6.6) have been generated for the full length nozzle.

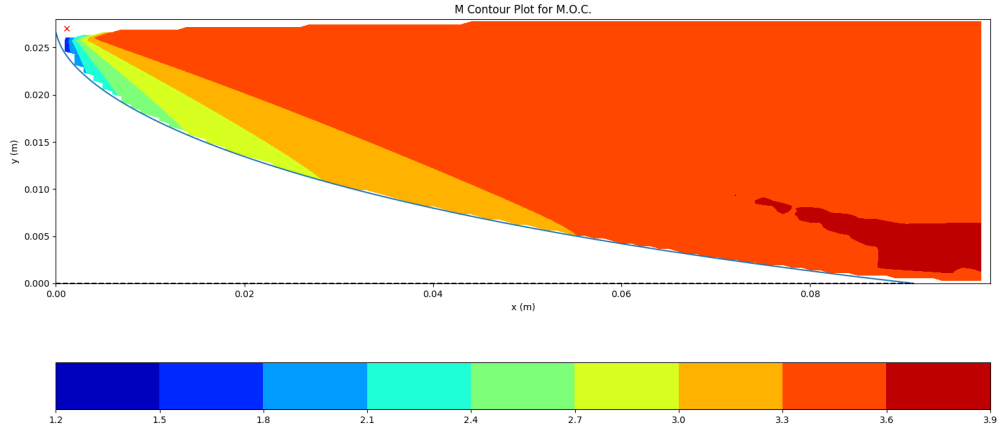

FIGURE 6.3: Mach Contour for Full Length Nozzle using M.O.C. at Design Altitude

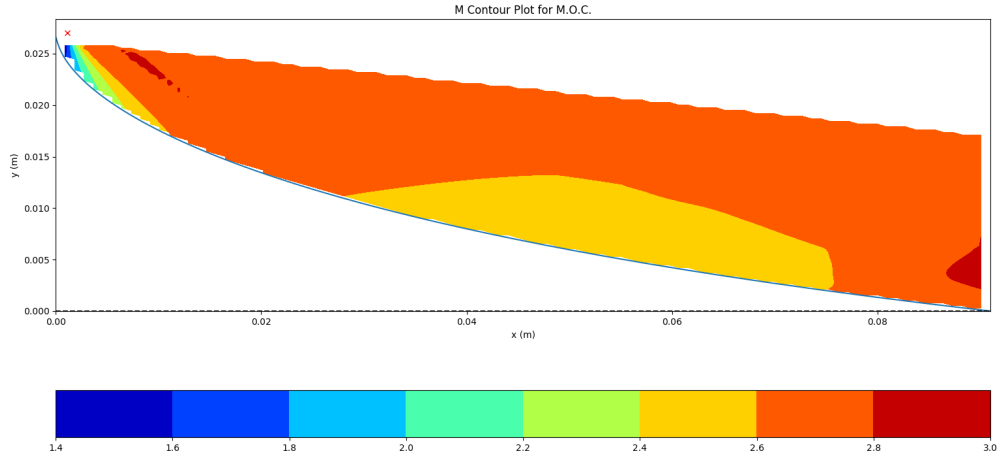

FIGURE 6.4: Mach Contour for Full Length Nozzle using M.O.C. at Sea Level

We see that the results for the design altitude mostly agree with was found using quasi-one-dimensional isentropic equations but notice that additional two dimensional complexity arises for the sea level prediction. This ability to accurately predict the flow at varying design altitudes greatly increases the the utility of optimization options available.

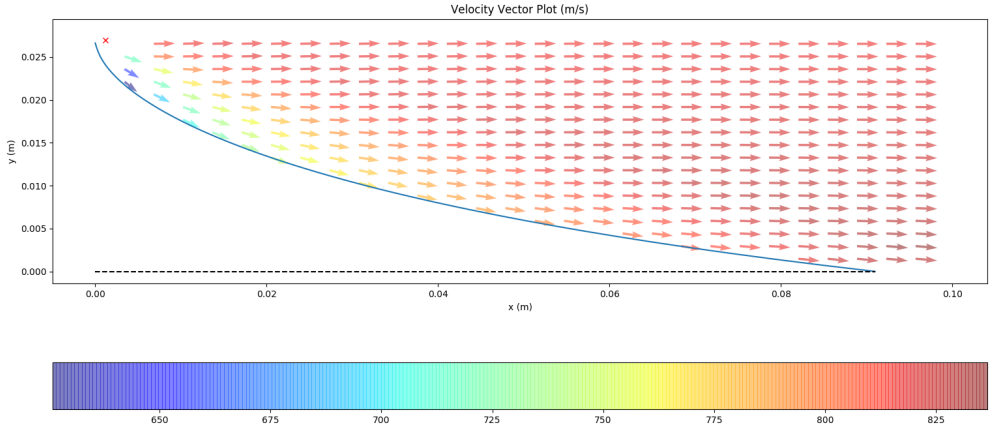

FIGURE 6.5: Velocity Vector Plot for Full Length Nozzle using M.O.C. at Design Altitude

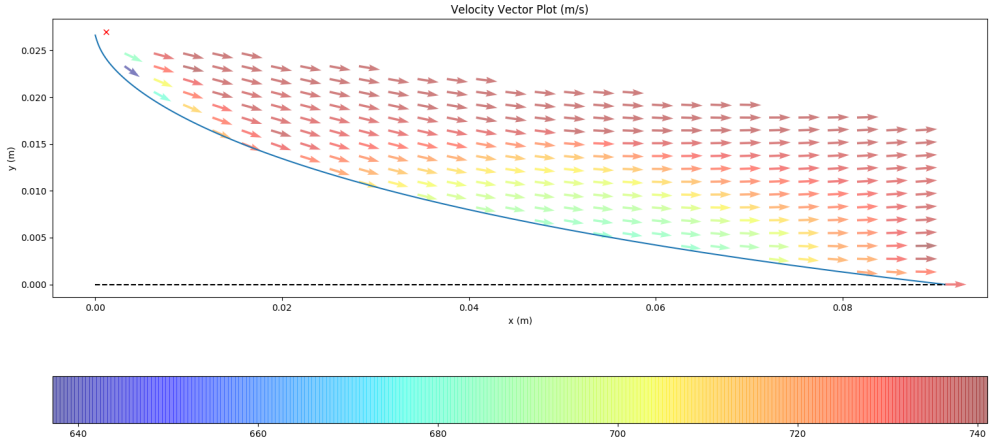

FIGURE 6.6: Velocity Vector Plot for Full Length Nozzle using M.O.C. at Sea Level

In order to estimate the flow properties of our truncated nozzle, a method for estimating the pressure at the base of the nozzle is required. For this, we chose to use the empirical model developed by the University of Rome. Their model was shown to be more accurate at estimating plug nozzle base pressure than methods developed by Fick et al.[**?**] and Rocketdyne [3]. If we let p_{atm} by the atmospheric pressure and M_{atm} be the atmospheric mach number, the following

equation for estimating the base pressure can be applied.

$$p_b = p_{atm}\left(0.05 + \frac{0.967}{1 + \frac{\gamma-1}{2}M_{atm}^2}\right)^{\Phi} \tag{6.3}$$

with Φ being given by:

$$\Phi = \frac{-0.2\phi^4 - 5.89\phi^2 + 20179.84}{\phi^4 + 20179.84} \tag{6.4}$$

where ϕ is the angle of the nozzle contour at the throat. Using this nozzle for base pressure, mach contour and velocity vector plots have been created for the truncated nozzle at both the design altitude (Figures 6.7 and 6.9) and sea level (Figures 6.8 and 6.10).

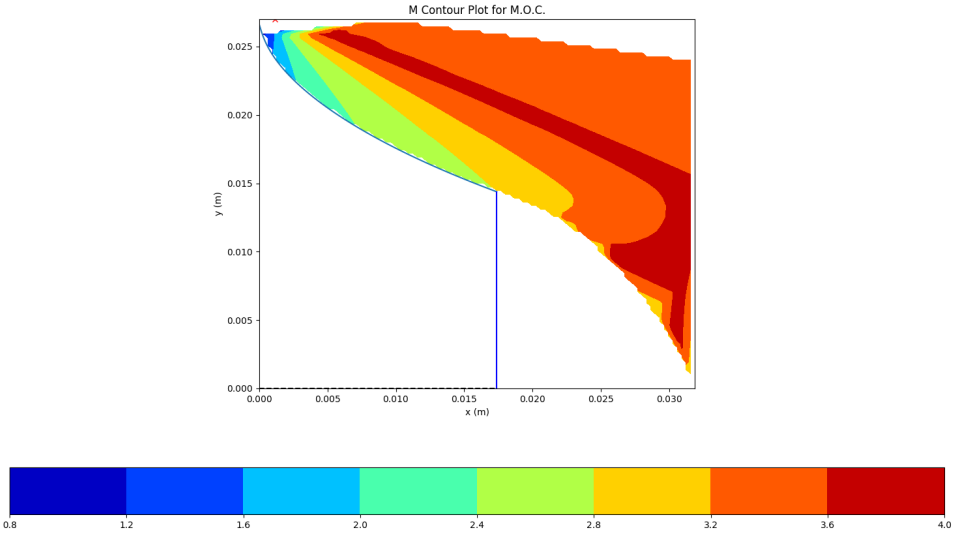

FIGURE 6.7: Mach Contour for 20% Length Nozzle using M.O.C.

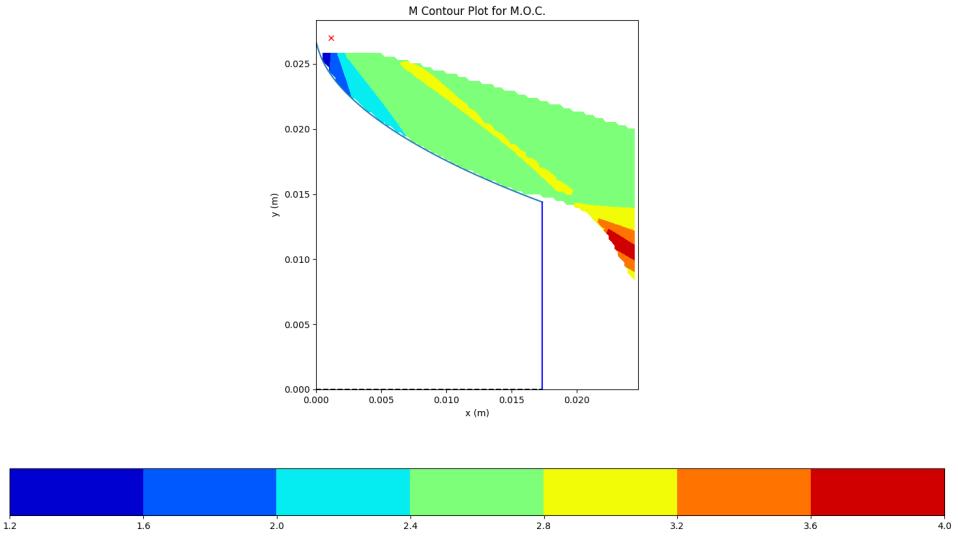

FIGURE 6.8: Mach Contour for 20% Length Nozzle using M.O.C.

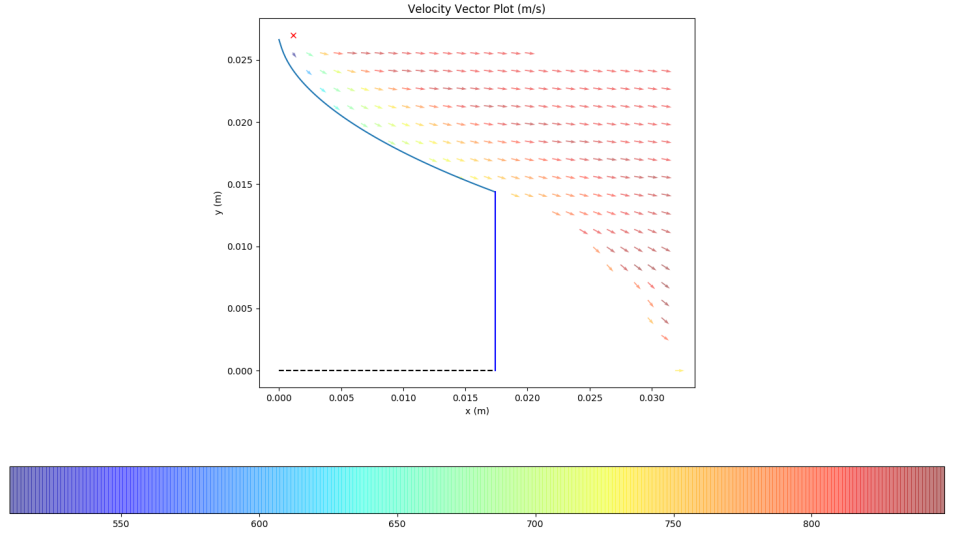

FIGURE 6.9: Velocity Vector Plot for 20% Length Nozzle using M.O.C.

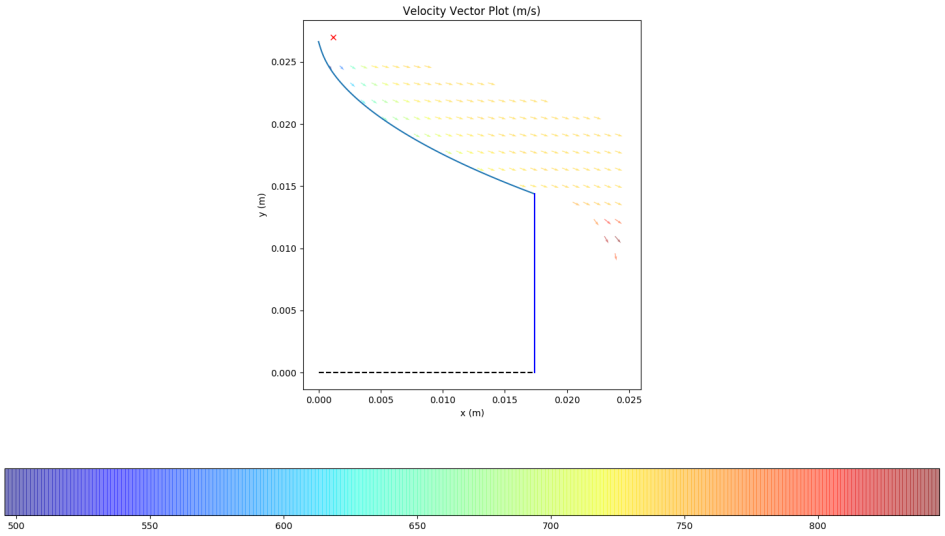

FIGURE 6.10: Velocity Vector Plot for 20% Length Nozzle using M.O.C.

It can be seen that the empirical base relation was able to predict the formation of an open wake relatively well. The method is also able to capture the two dimensional complexity introduced by both the truncation and altitude difference.

6.2 Iterate over input parameters

Now that a cost function has been developed that evaluates the nozzle based on functions parameterized by the chosen design variables, algorithms are able to be implemented to optimize over the design space.

For the first cost function that was developed (equation 6.1), a gradient based optimization algorithm is a good choice for optimization. Using a standard optimization toolbox (such as those provided with Matlab or SciPy) a local minimum can be found with relative ease. Choosing hyper parameters judiciously will heavily affect the results.

For the second cost function that was developed (equation 6.2), the large number of design space variables makes gradient based algorithms unfeasible. In this case, a method for understanding the design space is necessary. For this response surface methodology was investigated. It has been shown that genetic algorithms perform better than response surface methods in optimization problems where the cost function is relatively expensive to evaluate [25]. For this reason,

a genetic algorithm framework for optimization such as DEAP is suggested by the team in this case and should be investigated to develop UTAT's design methodology moving forward.
To summarize, two optimization methods were investigated for iterative optimization of the the nozzle contour. The first is relatively easy to implement but is limited by the low number of design variables it can optimize over. The second method for optimization is able to optimize over many more input variables and so is ideal for optimizing the shape of the contour to a greater resolution.

Chapter 7

Cooling Strategy

This section covers the second half of the cooling system design process, which is the selection of cooling strategy based on the calculation results in section 6.

After obtaining the heat flux flux and coolant flow rate with the optimized nozzle contour, the cooling strategy can be selected. This decision is based on the following factors: the firing time, pressure drop of the system and other design considerations. The following paragraphs describes the selection process with reference to Figure 7.1.

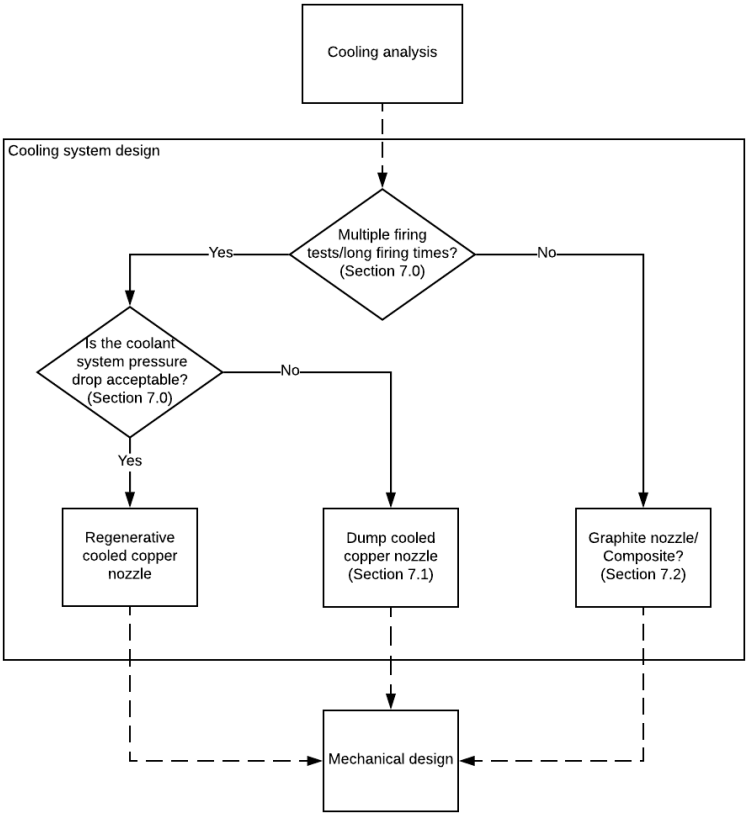

FIGURE 7.1: Cooling system design process overview

The first factor to consider is the desired firing time and firing frequency. Due to the erosion rate of ceramic and composite material, a nozzle with no cooling can only be fired for a certain amount of time before a significant drop in performance will be observed. As such, if it is desired

to fire the test stand repetitively for a long period of time, then the nozzle must be actively cooled. The erosion rate of graphite and performance degradation analysis is shown in Section 7.3.

The second factor to consider is the available pressure and pressure drop of the system. If active cooling must be used, and enough pressure is available to push the nitrous oxide from the tank to the nozzle and back into the combustion chamber, then regenerative cooling can be used. Otherwise, the nozzle must be dump cooled. With dump cooling, a separate tank and pressure line can be used to allow more pressure drop in the system.

Other design considerations are cost, environmental and safety which are covered in detail in Section 9.

For the test stand rocket nozzle, it is determined in Section 7.1 that extra pressure source of 800 psi is needed to achieve the desired chamber pressure given a regenerative cooling system. An extra pressure source is not easily accessible to UTAT, and over complicates the design. As such, regenerative cooling is considered to be out of the scope of this design. The approximate firing time for the test stand rocket is 4 seconds. As such, both copper nozzle with dump cooling and graphite nozzle with no cooling can be implemented. Both design are completed to give UTAT a detailed cost, environmental and safety analysis.

7.1 Regenerative cooling

Typically, the regenerative cooling method is more practicable and feasible in larger sized rockets due to the additional pressure losses along the system back into the combustion chamber. In this section, a detailed analysis of the regenerative cooling method will be assessed to identify the feasibility and key areas of concern.

Figure 7.5 illustrates the respective system in Aspen Plus.

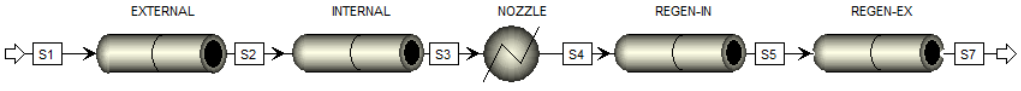

FIGURE 7.2: Aspen Plus Layout

The External Pipe is the segment from the oxidizer tank on the coolant line to the pipe insert right before entering the nozzle cooling channels. The internal pipe, is the 3 cm length tubing insert into the cooling channels. The heat exchanger represents the transfer of heat occurring the the nozzle while the regen-in and regen-ex are the respective piping leading the flow out of the cooling channels and into the combustion chamber.

Through the employment of the iterative process to determine pressure drop, the following scenario with a supercharged nitrous tank at 800psi could be accomplished with the following parameters.

The following pipe values are based off of Swagelok's metal tubing catalogue.

TABLE 7.1: Piping Parameters

Pipe	OD (in)	Wall Thickness (in)	ID (cm)
Internal Pipe	3/8	0.035	0.7747
External Pipe	5/8	0.035	1.0922

While pressures of 625 psi can still be obtained at the combustion chamber prior to the injector plate, the inner diameter of the piping insert to the coolant channels had to be increased to 3/8 inches which is physically impossible in this design as the nozzle size is only 2.14cm in radius. If the size of the cooling channels were not increased, the fluid would reach choking conditions with a Mach number exceeding 1.

	Units	S1	S2	S3	S4	S5	S7
Description							
From			EXTERNAL	INTERNAL	NOZZLE	REGEN-IN	REGEN-EX
To		EXTERNAL	INTERNAL	NOZZLE	REGEN-IN	REGEN-EX	
Stream Class		CONVEN	CONVEN	CONVEN	CONVEN	CONVEN	CONVEN
Maximum Relative Error							
Cost Flow	$/sec						
− **MIXED Substream**							
Phase		Liquid	Liquid	Liquid	Mixed	Mixed	Mixed
Temperature	K	291.15	290.962	290.932	294.938	294.248	286.295
Pressure	psi	800	768.729	763.759	763	751.246	625.411
Molar Vapor Fraction		0	0	0	0.210328	0.218588	0.294138
Molar Liquid Fraction		1	1	1	0.789672	0.781412	0.705862

FIGURE 7.3: Stream Pressures

7.2 Dump Cooling

7.2.1 External Cooling System

The dump cooling system is shown in Figure 7.4.A pressure of 556 psi can be obtained at the cooling channels for a 0.72kg/s flow rate. At this pressure, only 0.703 kg/s is required which provides a 2.4 % leeway in mass flow rate.

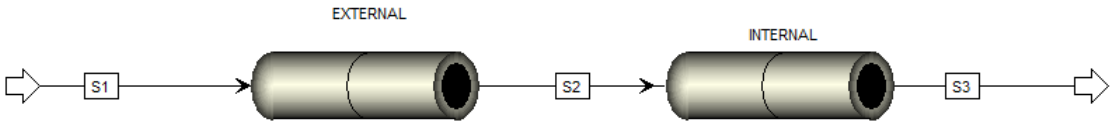

FIGURE 7.4: Aspen Plus Layout

TABLE 7.2: Piping Parameters

Pipe	OD (in)	Wall Thickness (in)	ID (cm)
Internal Pipe	5/16	0.035	0.61595
External Pipe	1/2	0.035	1.0922

The pipe size requirement for dump cooling on the "internal" section is much smaller than regenerative cooling making it a more feasible option in small scaled operations as the maximum size of the pipe is restricted by the nozzle throat diameter.

The stream pressures are listed below for the dump cooling system.

	Units	S1	S2	S3
Description				
From			EXTERNAL	INTERNAL
To		EXTERNAL	INTERNAL	
Stream Class		CONVEN	CONVEN	CONVEN
Maximum Relative Error				
Cost Flow	$/sec			
− **MIXED Substream**				
Phase		Liquid	Mixed	Mixed
Temperature	K	291.15	285.456	281.439
Pressure	psi	700.125	613.139	556.839

FIGURE 7.5: Stream Pressures

7.2.2 Internal Cooling Channels

The internal cooling channels are designed with performance, ease of manufacturing and ease of assembly in mind. A cross section of the copper nozzle is seen in Figure 7.6. The nozzle assembly is comprised of two parts, the inner nozzle and the outer shell. The two parts are designed such that there is a gap in between to allow coolant flow when assembled. This results in an annular coolant flow path shown in Figure 7.7.

The main advantages of this design are:

- Maximizes the surface area of contact between the coolant and the nozzle wall; the coolant is in contact with the nozzle wall in all radial direction

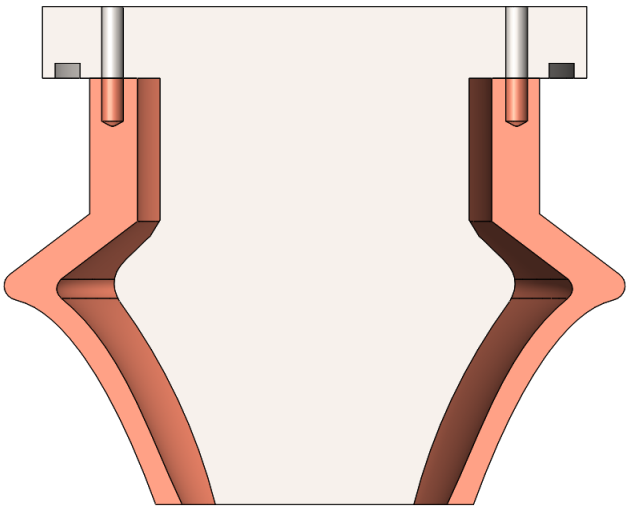

FIGURE 7.6: Copper nozzle cooling channels side view

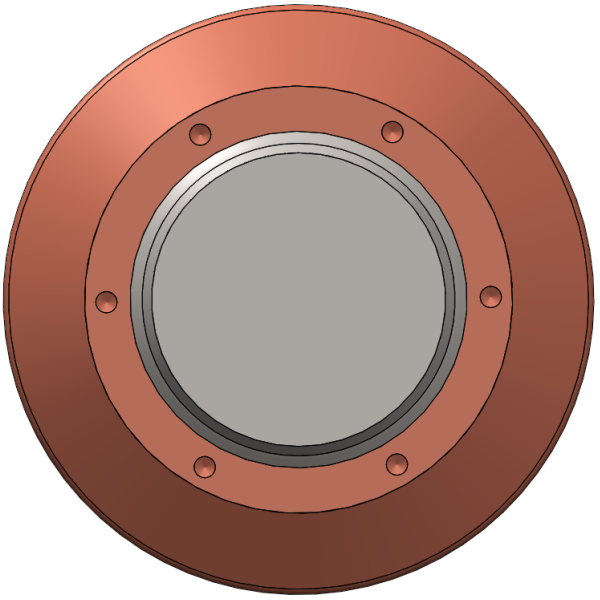

FIGURE 7.7: Copper nozzle cooling channels top view annular ring

- No machining of complected cooling channels; simple annular geometry
- Ease of assembly; two nozzle parts with one inside the other

Heat Transfer

A key design parameter for this configuration is the size of the annular gap. To maintain the nozzle at a steady state temperature, the heat transferred to the nozzle must equal the heat

taken away by the coolant. With reference to equation 7.1, because the temperature of the nozzle wall and the temperature of the coolant cannot be changed, the only parameter that can be designed is the heat transfer coefficient. This parameter depends on coolant flow rate, gap size and coolant pressure.

$$q_{conv} = h_g(T_{\infty g} - T_{wg}) = h_c(T_{\infty c} - T_{wc}) \tag{7.1}$$

The cooling channel gap should be sized to be sufficiently small to give a high heat transfer coefficient, but cannot be so small that it limits manufacturing or results in excessive pressure drop.

The prediction of heat transfer coefficient for two phase boiling flow is difficult, but has been widely studied in literature and several empirical correlation have been developed. The Shah correlation developed through the analysis of 780 data points and over 19 independent studies can be applied to a wide variety of geometry using the equivalent hydraulic diameter [26] [27]. For annular flow specifically, equation 7.2 and 7.3 are recommended by Shah [27].

$$Gap > 4mm,\ D_{HYD} = \frac{4 \times flow\ area}{wetted\ perimeter} \tag{7.2}$$

$$Gap < 4mm,\ D_{HYD} = \frac{4 \times flow\ area}{heated\ perimeter} \tag{7.3}$$

The basic principle of Shah's correlation is that the two phase heat transfer coefficient, h_c, is related to the liquid phase heat transfer coefficient, h_{liq} through the factor ψ as shown in equation 7.4. The correlation is based on three dimensionless numbers: the boiling number, the convection number and the Froude's number. The liquid heat transfer coefficient is obtained by using a Dittus-Boelter correlation.

$$\psi = \frac{h_c}{h_{liq}} \tag{7.4}$$

In reference [28], it was found that the Shah correlation over predicts the heat transfer coefficient for nitrous oxide when compared to experimental results. A modified boiling number is then introduced ($Bo_{eff} = 0.35Bo$) to more accurately predict the heat transfer coefficient for nitrous oxide, reducing the prediction error from 68% to 13% [28]. The detail calculation procedure for the Shah correlation with modifier boiling number is outlined in Appendix B.

The Shah model is only applicable to the nucleate boiling regime and is more accurate at low vapour quality. With reference [28] being the only paper with experimental data on nitrous oxide, an assumption is made that nozzle cooling channels will operate in the nucleate boiling regime by keeping the nitrous oxide at low vapour quality (below 0.4 as stated in Section 5.2).

Using the Shah correlation and the modified boiling number, an annular gap of 6mm is sized for the test stand nozzle. The resulting coolant heat transfer coefficient in shown in Figure 7.8,

the temperature of the copper nozzle assuming one dimensional heat transfer and the change in vapour quality are shown in Figure 7.9.

The temperature of the nozzle wall has been computed assuming only one dimensional heat conduction in the radial direction. This results in the worse case temperature profile at the throat. It can be seen that the nozzle does not exceed the maximum design temperature of 700 K at any location. In reality, with three dimensional heat transfer by conduction, the temperature profile will be more uniform approaching a constant temperature of around 450 K through out the nozzle.

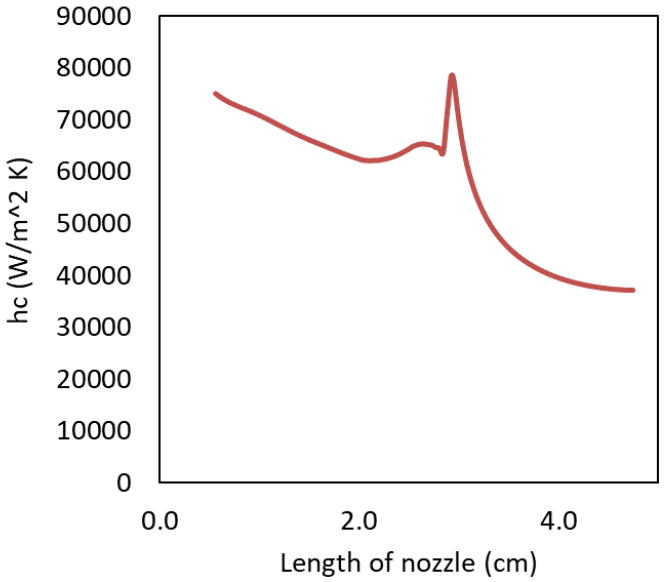

FIGURE 7.8: Heat transfer coefficient of nitrous oxide

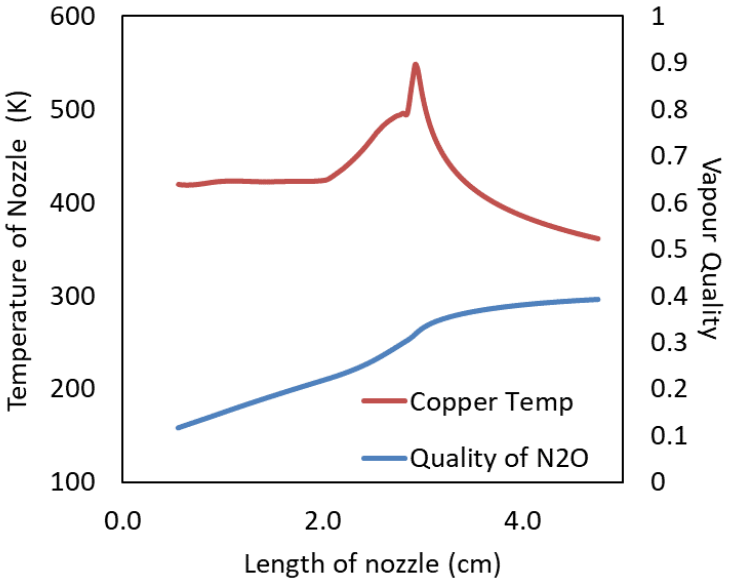

FIGURE 7.9: Nozzle surface temperature and nitrous oxide vapour quality

Pressure Drop

Based on similar cooling channel design for nitrous oxide in reference [17] and [19], the pressure drop inside cooling channels have not been reported to be significant given the short length of the channels. Nevertheless, the pressure drop has been calculated according to the homogeneous flow method outlined in reference [29], based on thermal hydraulics analysis of nuclear reactors.

Based on the homogeneous flow model, the total pressure drop is the sum of the gravitational pressure drop, the acceleration pressure drop and the frictional pressure drop as per equation 7.5.

$$\Delta P_{total} = \Delta P_{fric} + \Delta P_{acc} + \Delta P_{grav} \tag{7.5}$$

The frictional pressure drop of a boiling channel is greater than that for a single phase channel with same length and mass flow rate. As such, an average two phase multiplier factor is applied to calculate the frictional pressure drop. All detail formulas can be found in reference [29]. The resulting pressure drop of the 3cm annular channel is 25.6 kPa (3.72 psi).

7.2.3 Summary

All calculation results of the copper nozzle with the dump cooling system configuration is summarized in Table 7.3 below.

TABLE 7.3: Nozzle Design Parameters Summary

Parameter	Value	Units
Nozzle Throat Diameter	2.92	cm
Nozzle Length	4.75	cm
Annular Cooling Channel Gap	6.0	mm
Heat Flux	41.9	kw
Coolant Flow rate	0.72	kg/s
Coolant Inlet Pressure	38.3	bar
Cooling Channel Pressure Drop	25.6	kPa

7.3 Passive Cooling

An alternative to active cooling methods would be passive cooling or the selection of a insulator material that could withstand such high temperatures.

7.3.1 Thermosets

Ablation, the process of pyroysis through an external applied heat source and exposure to high temperature leads to charring of the object's surface which acts as a thermal insulator. In this

scenario, thermosets, specifically resins can be used as a potential alternative to maintaining the nozzle structure without the design of cooling channels.

A resin system with carbon fiber is more easily accessible but has a lower service temperature around 2000 °C while a silica fiber system can withstand up to 5000 K for short periods [30]. While silica fiber offers better thermal resistance, the manufacturing process present more safety hazards associated with handling fiberglass. The health effects from fiberglass exposure are dependent upon the size and type of exposure. Larger fibers cause skin, eye and upper respiratory tract irritation. Proper PPE such as gloves and a mask would need to be worn to prevent contact or inhalation of the fibers [31].

The manufacturing of phenolic resin systems poses a significant challenge since there are no available vendors to manufacture the fiber-resin system in the desired nozzle shape. This would require us to develop a manufacturing process that maintains a uniform and high quality as well as molds, which can cost up to $5,000. During this process, a mold of the nozzle would have to be made using CNC-milling with a block of aluminum that can be vacuum sealed and cured in an oven. The phenolic resin which exists as a liquid would then have to be poured into the mold with the fiber material being wrapped around tightly.

As this process is all by hand, the uniformity of the resulting product is very difficult to maintain and thus its desired high thermal properties would be compromised. Overall, the manufacturing process of fiber resin systems are very complex and require expertise to manufacture the product to desired standards. As seen in the table below, carbon fiber has a higher ablative efficiency whereas silica fiber has a higher insulation index and less tendency to ablate.

UTAT is currently exploring the feasibility of using carbon fiber in the design of a bell nozzle as it is more readily available and the results from such project would help guide future development of nozzles using ablative materials.

7.4 Graphite

Graphite nozzles have conventionally been used for non-cooling methods of nozzle design. Due to the high thermal resistance of graphite, it can operate at temperatures of up to 3650 °C. [**?**]

To develop a model for to describe the erosion rate, both theoretical and experimental must be conducted. In the paper on "Numerical Analysis of Nozzle Material Thermochemical Erosion in Hybrid Rocket Engines," the thermochemical model was developed to solve the following[7]:

- Turbulent Reynolds averaged Navier–Stokes equations used for gaseous flow in nozzle

- Thermodynamic properties of individual species approximated by seventh-order polynomials
- Mixture properties for conductivity and viscosity derived from Wilke's rule
- Diffusion model based on effective diffusion coefficients
- 1-D heat conduction

The results of this model highlight the following dependencies of nozzle erosion rates[7]:

- High oxygen content oxidizers such as oxygen and nitrogen tetroxide can significantly increase the erosion rate
- Fuel choice does not have any significant impact on the erosion rate
- Flame temperature and type of oxidizing species has an impact
- Water vapor is the oxidizing species with the most significantly impact contributing to over 50% of erosion rate for all propellant combinations
- Oxidizer rich conditions (O/F) produce a small reduction in erosion rate due to the oxygen content and the exothermic reaction with graphite
- Fuel rich conditions can reduce erosion rate significantly
- Wall radiation is important at low pressures and negligible at high temperatures

Based on these conclusions, the following graph for of the erosion rate can be applied to this scenario.

The literature values for graphite erosion from Figure 7.8 indicate a range of approximate 0.03 mm/s to 0.05mm/s for nitrous oxide. With an erosion rate of 0.05mm/s and a 4 second burn time, the radius of the nozzle at the throat would decrease by 0.2mm after each run.

Suppliers typically prefer not to work with graphite as a manufacturing material as it is abrasive and causes high tool wear rates [32].

As was discussed above, throat erosion for graphite nozzles results in reduced thrust overtime. To estimate this loss in thrust mach area relations are first used to calculate the exhaust gas properties (see equation 4.8). Having determined the exhaust gas properties, the thrust can be determined using the one-dimensional ideal thrust equation. (see equation 4.6). Figure 7.11 below shows how the thrust can be expected to change over a single run for both the best and worst case erosion rates.

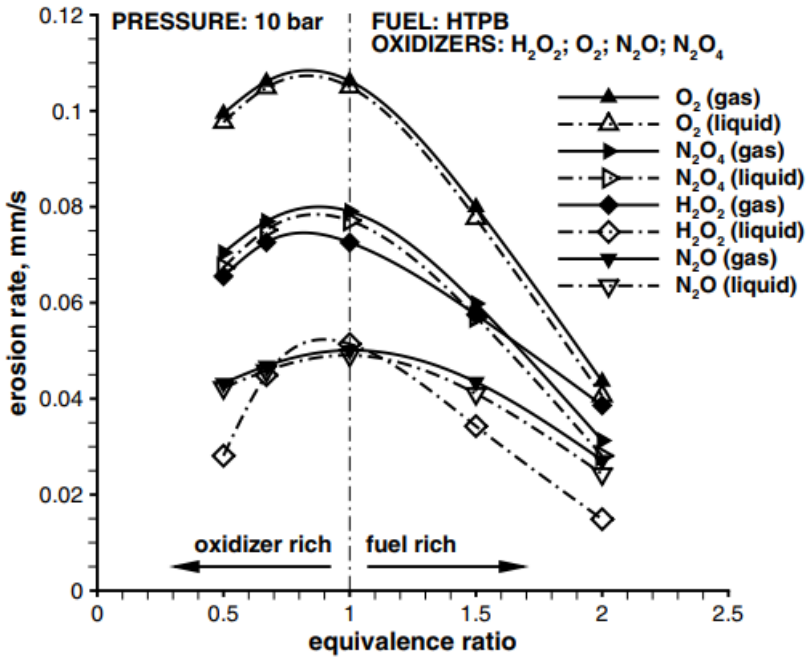

FIGURE 7.10: Nozzle throat erosion and equivalence ratio for graphite nozzle

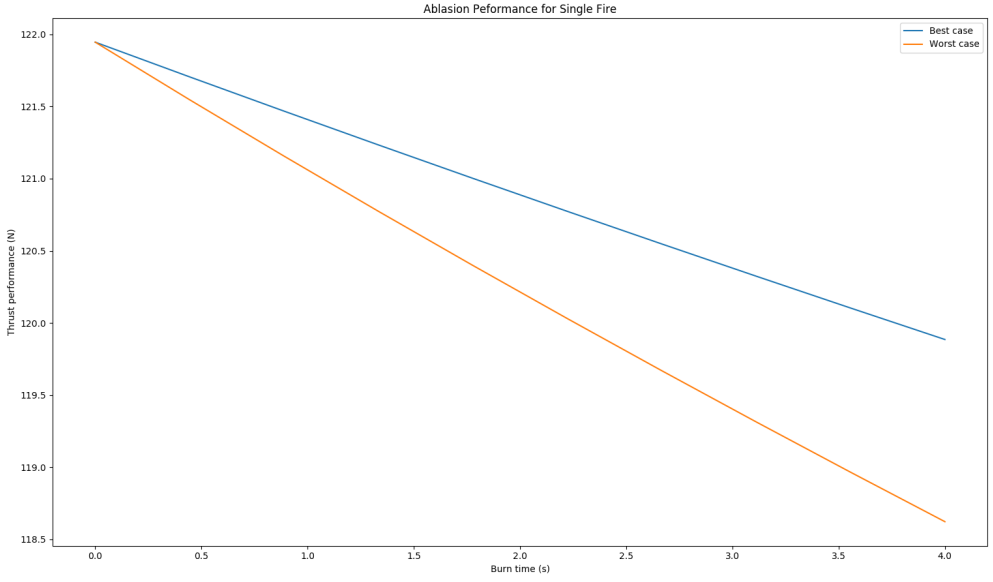

FIGURE 7.11: Nozzle Thrust with Single Fire

A 10% reduction in thrust is considered undesirable in terms of engine performance. As such, based on Figure 7.9, the nozzle can be used 3 to 5 times based on worst case to best case erosion rates.

Chapter 8

Mechanical Design

This chapter covers the detailed mechanical design of the rocket. Using the data obtained from the previous chapters, including nozzle contour design and cooling channels design, two types of nozzles are generated.

8.1 Copper Nozzle with Dump Cooling

As can be seen in the drawing below, the dump cooled copper nozzle design includes five parts: ① Graphite Base, ② Inner Steel Nozzle, ③ Graphite Front Fixture, ④ Copper Outer Nozzle and ⑤ Graphite Lip.

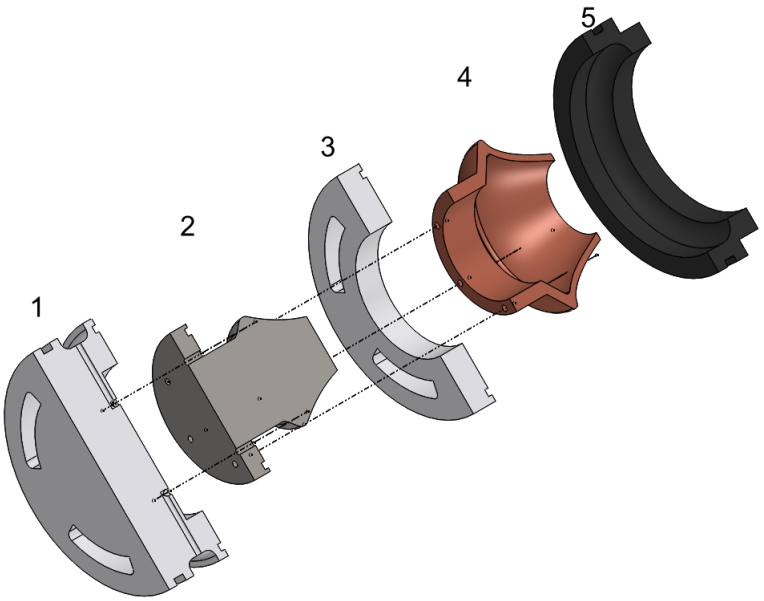

FIGURE 8.1: Exploded View of Complete Nozzle Assembly

The assembly process starts from part ① to part ⑤. Firstly, parts ② ③ ④ are combined together and six bolts are used to attach the inner nozzle with the outer nozzle.

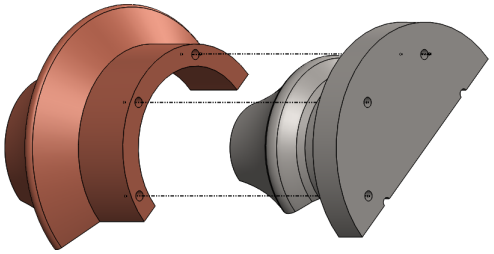

FIGURE 8.2: Inner and Outer Nozzle Assembly

Then this sub-assembly is placed onto the graphite base. Finally, the complete assembly is slid into the combustion chamber and fixed by the retaining ring, which is fixed at the annular slot on the graphite base ①. The cooling channels will be connected to two tubes outside of the rocket. Note that 5 O-Rings will be placed accordingly in order to seal the design.

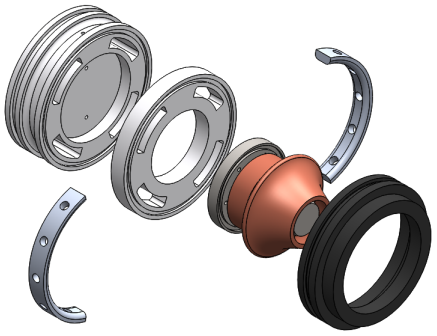

FIGURE 8.3: Complete Exploded View of the Assembly

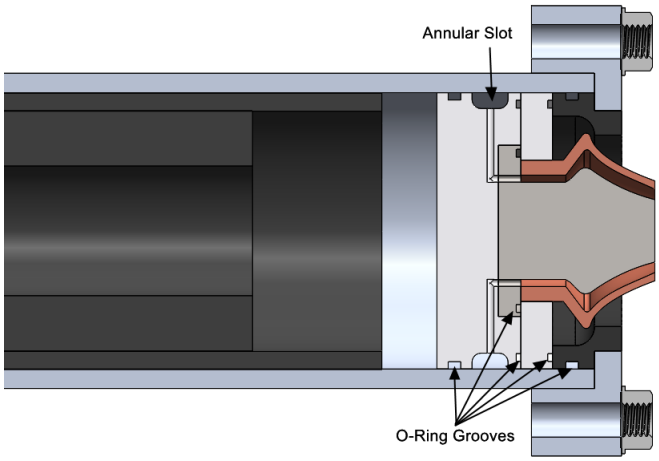

FIGURE 8.4: Complete Assembly in the Combustion Chamber

① and ③ are covers made of graphite that are used to protect the metal parts from the high temperature combustion gases. The stainless steel inner nozzle has a thick neck where the cooling performance is least effective. This part is sandwiched between two graphite pieces so that the surfaces of the inner nozzle is not exposed to the hot gases.

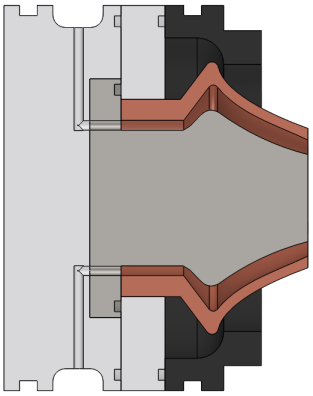

FIGURE 8.5: Detailed Cross-section of the Cooling Channel

8.2 Graphite Nozzle

The mechanical design and analysis of nozzles involves the careful interplay of manufacturing feasibility, cost, and safety factor against failure. The geometry must always be created keeping in mind how exactly it will be manufactured, this will dictate the feasibility of tolerances required, minimum corner radius and such.

After multiple rounds of iterative design and analysis the final graphite nozzle is seen in figure 8.6. The design underwent close to 20 iterations in order to simplify and optimize its geometry to maximize its safety factor, and ease manufacturing.

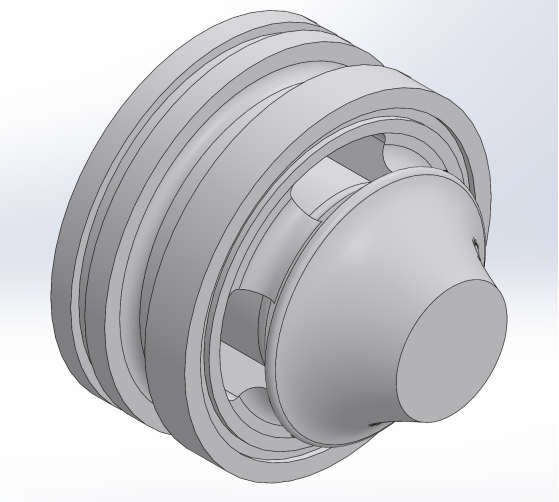

FIGURE 8.6: Final Graphite Aerospike Nozzle

Rocket nozzles need undergo rigorous failure analysis as they typically experience the high pressure, low speed gases of the combustion chamber as well as the high speed, low pressure gases typical of the diverging nozzle region. The complex curves in the diverging region alone render simple failure analysis obsolete and requires the finite element method to be employed. ANSYS Mechanical was selected as the solver of choice to carry out all FEA tasks in this project.

Boundary conditions and Mesh

Three separate pressure loads were employed in order to model the decreasing pressure of the gases as they accelerate. A pressure of 250 psi was applied to the diverging portion of the nozzle. This value is the pressure of the nozzle at the first point of the diverging region as calculated using the method of characteristics. As can be seen in the method of characteristics plots, the pressure along the diverging region of the nozzle drops rapidly to atmospheric pressure (15 psi). Thus, this additional loading ensures a built in safety factor for the design. Above the diverging region of the nozzle a pressure of 450 psi, equal to that of the combustion chamber is applied. Lastly an atmospheric pressure of 15 psi was applied at the nozzle base for completion. The main pressure loading on the nozzle body can be seen in Figure 8.7 and 8.8.

Fixed support boundary conditions were employed at the portion where the retaining ring is mounted. Additionally, fixed supports were placed in the region of the nozzle corresponding to the combustion chamber retainer. Cylindrical supports were placed in the regions in contact with the combustion chamber, and with the inner radial region of the nozzle retaining ring. The application of the fixed and cylindrical supports respectively can be seen in figures 8.9 and 8.10.

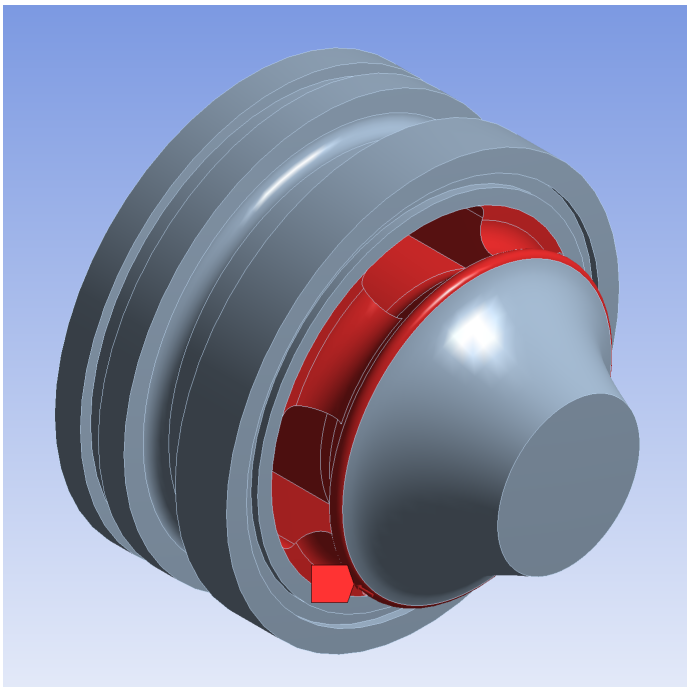

FIGURE 8.7: 450 PSI pressure loading for FEA simulation

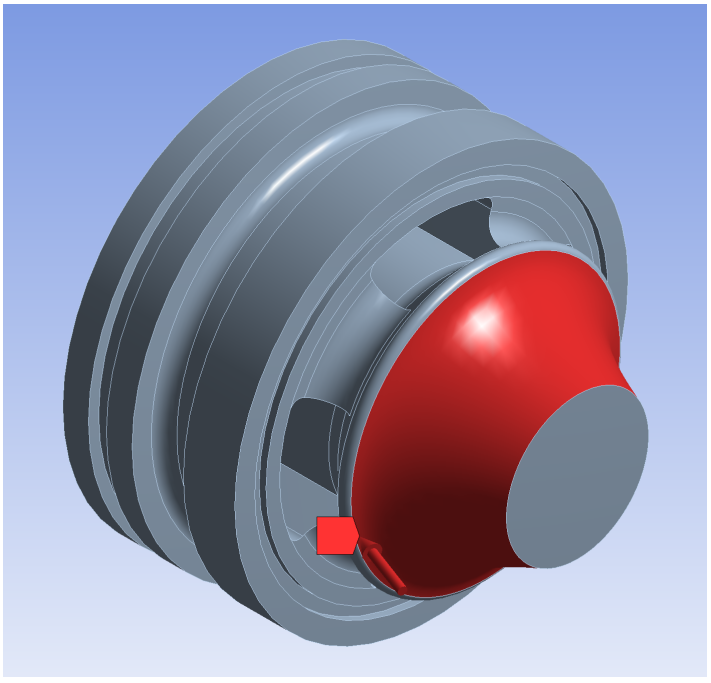

FIGURE 8.8: 250 PSI pressure loading for FEA simulation

The mesh used contains 245,157 tetrahedral elements with an average orthogonal quality of 0.84. The mesh was refined at the areas of interest and can be seen in figure 8.11.

FEA Challenges

The results of the the FEA analysis must be interpreted with care as there are two issues which make an accurate FEA analysis challenging. The most important of the two is the fact

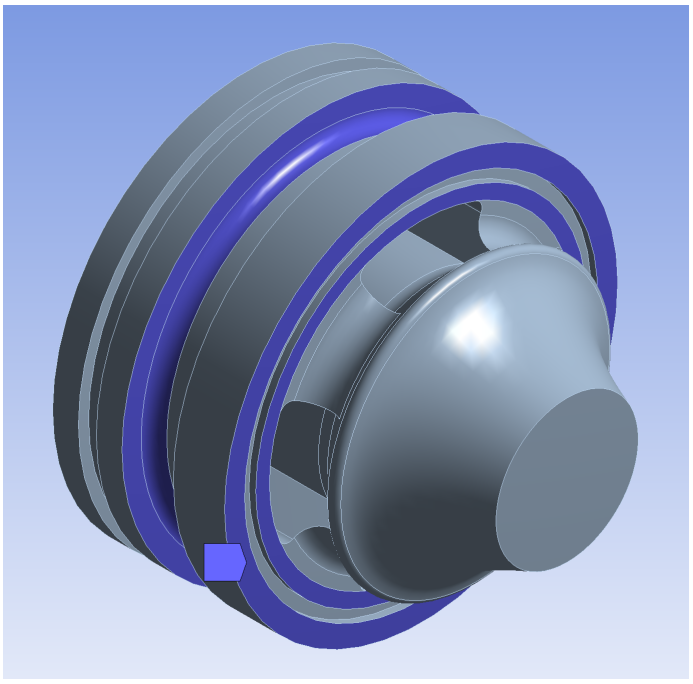

FIGURE 8.9: Fixed support constraint for FEA simulation

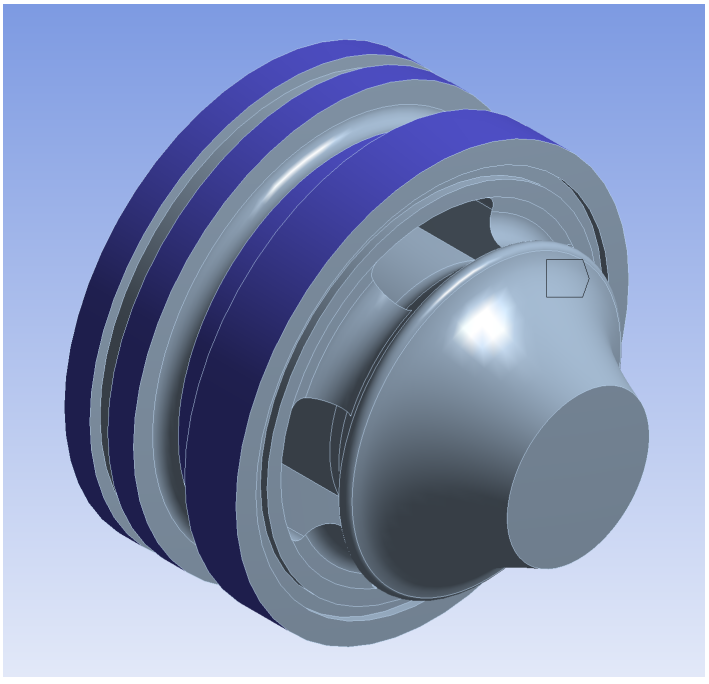

FIGURE 8.10: Cylindrical support constraint for FEA simulation

that it is not possible to obtain an equivalent stress from the stress tensor while analyzing brittle materials, as such it is not possible to evaluate it against the set of standard material properties given for most materials [33]. One failure criterion which has been used extensively for brittle materials is the Maximum Normal Stress criterion, using the maximum principal stress to evaluate the results.

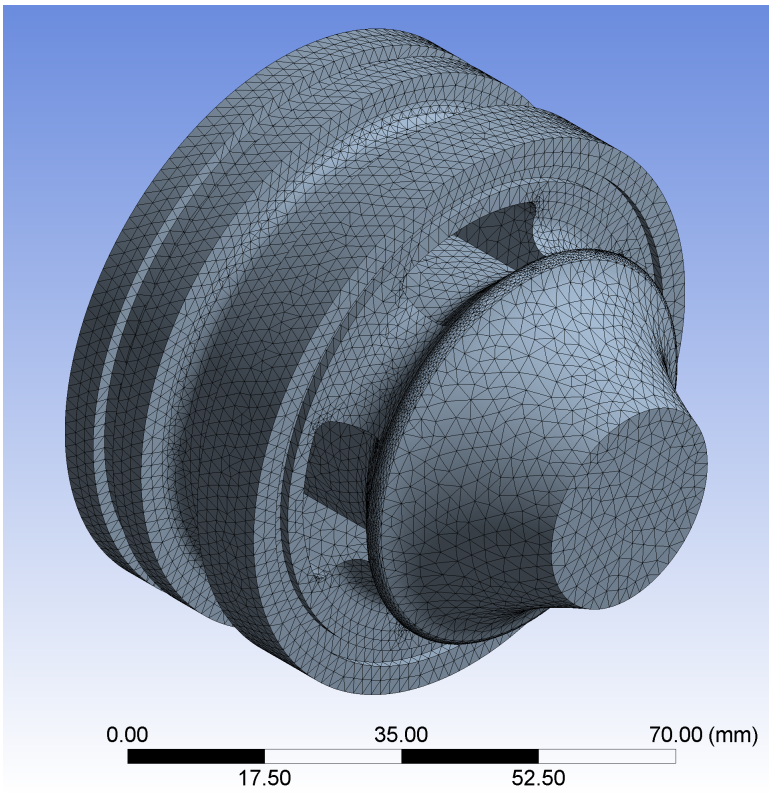

FIGURE 8.11: Aerospike Nozzle Mesh for FEA analysis

Additionally, graphite unlike many standard manufacturing materials such as aluminum, or stainless steel has many different grades whose mechanical properties vary immensely. As such a reasonable assumption must be made for the input material properties of the graphite. The material properties were obtained from Graphtek, a popular supplier of graphite stock to machine shops. We used an average from the graphite stock mechanical properties they provide [34].

FEA Results and discussion

Cross-sectional views of the maximum principal stress along two different planes can be seen in Figures 8.12 and 8.13. As seen in Figure 8.12, the maximum principal stress was predicted at the upper left corner of the figure. This result can be neglected as this point is not under direct contact with the flow, given that an EPDM (ethylene propylene diene monomer rubber) liner will be covering this section. Additionally, the CAD model which was used to run this FEA did not have chamfers or fillets at every discontinuity. Being a sharp discontinuity, the simulation predicts a significant stress concentration at the corner leading to the high stress seen. The true area of concern in this nozzle, as can be seen in the FEA results, is the region connecting the converging portion of the nozzle with the region immediately upstream of the converging section. The curve which connects these two sections underwent extensive iteration, as maximizing the angle of curvature would reduce the stress in the region but could also impact the subsonic acceleration of the fluid as it approached the throat. This region contained the

minimum safety factor for the entire geometry at 1.70, as evaluated with the maximum principal stress and the tensile yield strength.

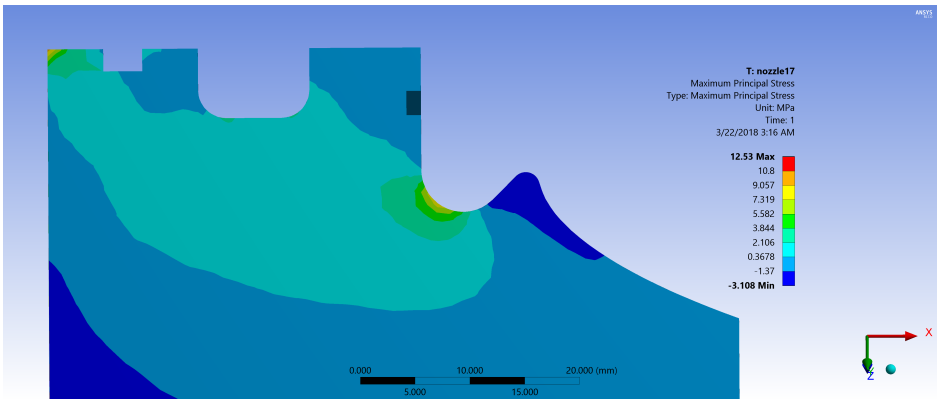

FIGURE 8.12: Maximum principal stress through cross-section in Aerospike Nozzle

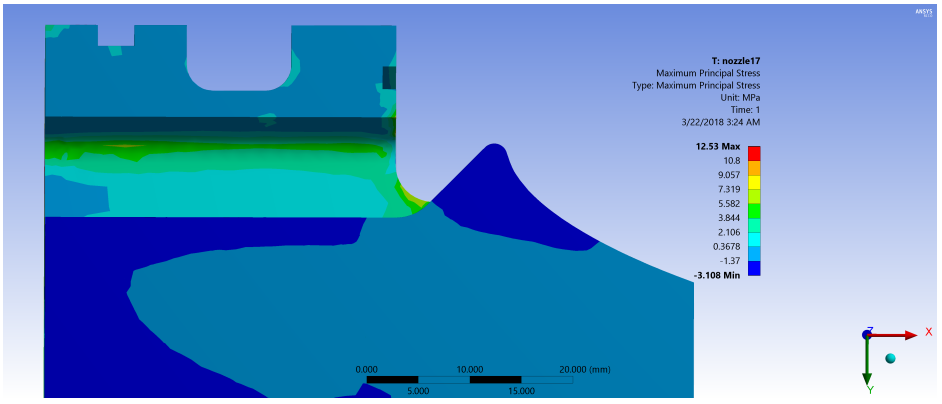

FIGURE 8.13: Maximum principal stress through flow channel cross-section in Aerospike Nozzle

Another region of interest was the distance between the bottom plane of the retaining ring groove and the parallel plane downstream of it. Stress concentrations close together interact resulting in accelerated failure [35], as these two regions contain stress concentrations as a result of the curved corners they posses, increasing their separation distance would be beneficial. However, in order to minimize manufacturing cost and weight, the separation distance would need to be kept within the smallest reasonable range possible while maintaining structural integrity.

Chapter 9

Test Stand Design

The main components of the test stand are the structural supports, the oxidizer feed system and the engine. The test stand design outlined in this section is applicable for both an engine with a graphite or copper nozzle. The only difference being that the copper nozzle will have an additional coolant line.

A cost analysis and hazard analysis of the test stand will also be covered in this section. All analysis considers both the copper and graphite nozzle.

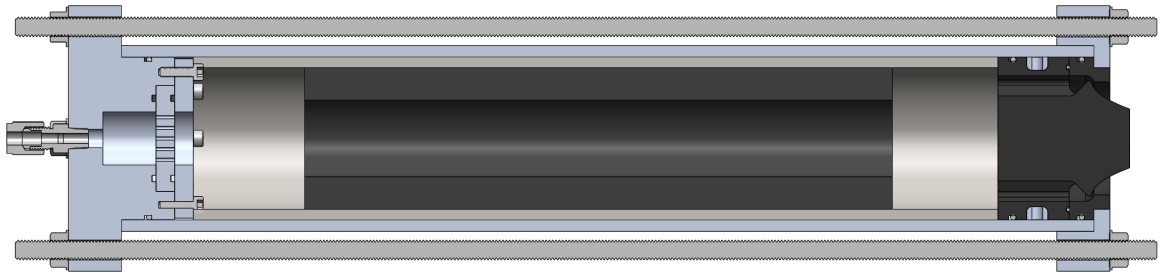

FIGURE 9.1: Final engine configuration with the graphite nozzle

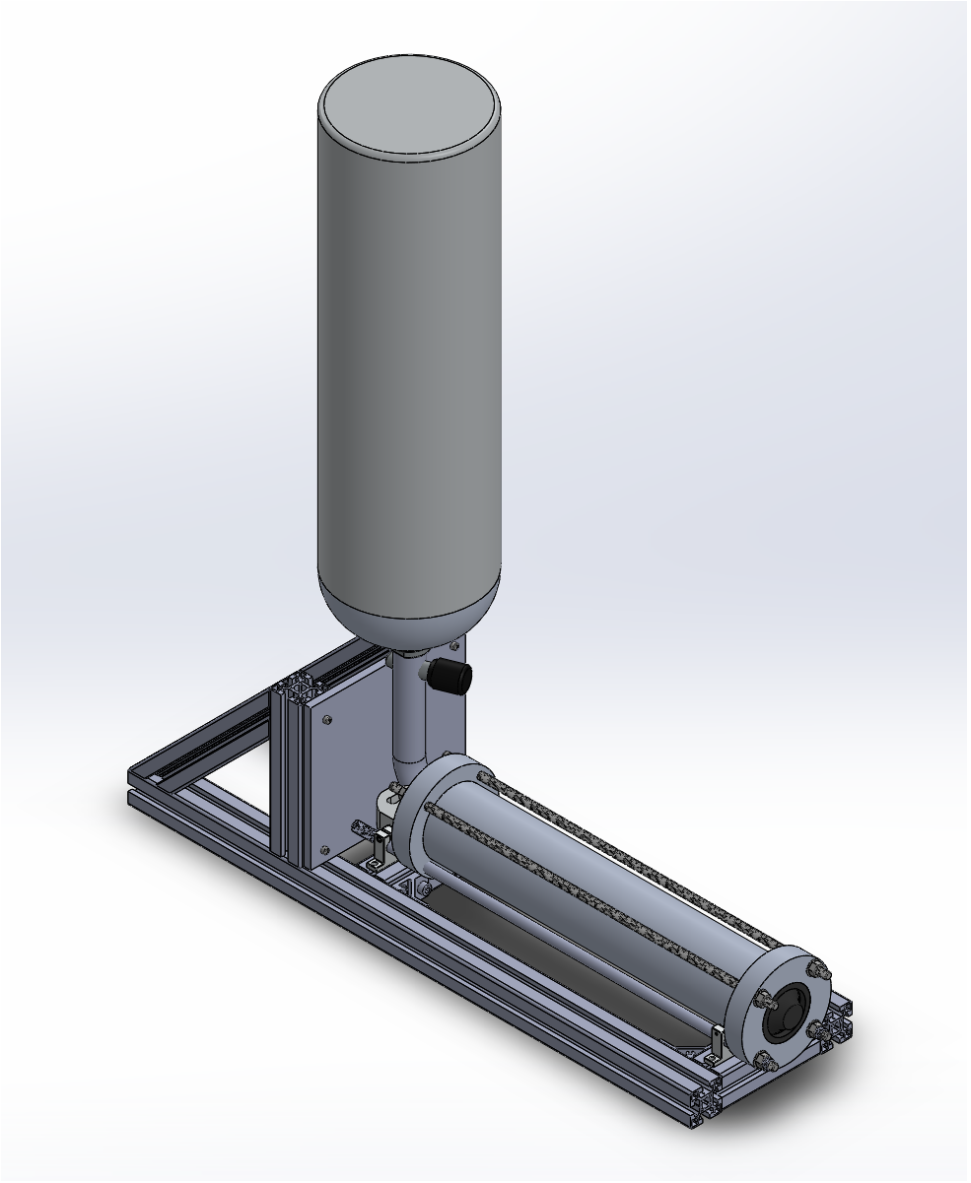

FIGURE 9.2: Engine mounted and mock feed system

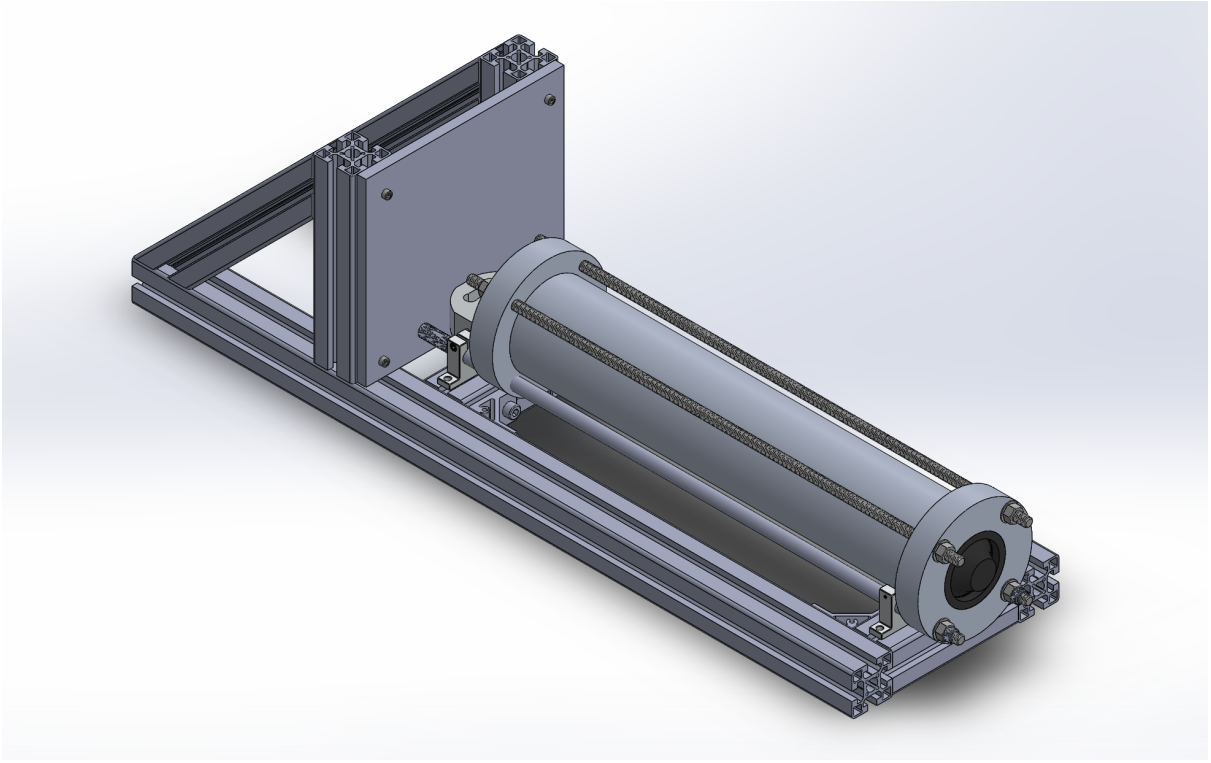

FIGURE 9.3: Test stand with engine mounted

9.1 Structural Support

The structural support for the test stand has two important functions. They are to prevent the engine from leaving a specified area and to provide a means of measuring engine thrust output.For the lab scale test stand, the measuring of engine thrust is accomplished through a standard strain-based load cell.

In order to measure the engine thrust, the engine and anchor block must be able to move independently of one another. Typically, this ability to move is accomplished by placing the engine on wheels [36] [37]. We chose to place the engine on rails to prevent unexpected lateral movement.

Due to the low ideal thrust output of the lab scale engine of 120N (12.2kg or 27lbs), little structural analysis was required. Please refer to Figure 9.2 for the design drawings of the test stand.

9.2 Oxidizer feed and Coolant system

The following figure outlines the feed system and the cooling system of the test stand. For both systems, a 10 lb nitrous oxide compressed gas tank will be used as the oxidizer source. The highest flowing CGA (Compressed Gas Association) approved bottle valve on the market has been selected to ensure low pressure drop. A bottle opener will be installed on the valve for remote actuation during start up and shut down. Burst disk cap are installed on the tanks for pressure relief during emergency.

The tank is connected to the engine chamber and nozzle using stainless steel pipes sized in section 7. A check valve is placed along the line to ensure no back flow in case of system over pressure. For the coolant system specifically, a reducer has been placed before the entrance to the nozzle to reduce the pipe diameter from 1/2" to 5/16".

Pressure and temperature measurement devices are placed at strategic locations to measure key operating parameters.

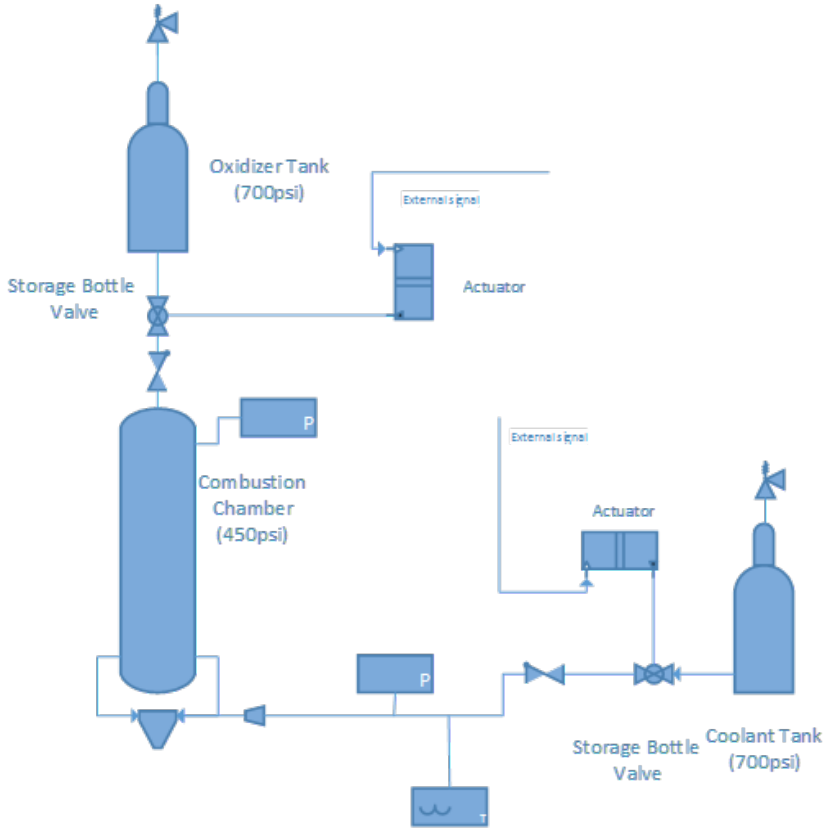

FIGURE 9.4: Feed and Coolant System

9.3 Cost analysis

This section outlined the cost analysis of the test stand, engine and nozzle. Misumi USA is the preferred vendor for most engine parts and plumbing due to its sponsorship relationship with UTAT. However, the full price of all items are listed in tables C.1 to C.4 for comparison purposes. The overall cost of the two different nozzle and cooling system are listed in tables 9.1 and 9.2 below. The team has worked with Graphite Sales Inc. to reduce the cost of the graphite components. The lead time is three weeks for the graphite components, and two weeks for the metal components.

TABLE 9.1: Nozzle cost comparison

Graphite Nozzle			
Component	Vendor	Quantity	Cost
Graphite Nozzle	Graphite Sales Inc.	1	$ 446.82
Graphite Nozzle Lip	Graphite Sales Inc.	1	$ 221.22
		Total	**$ 668.04**
Copper Nozzle			
Component	Vendor	Quantity	Cost
Inner Stainless Steel Nozzle	Xometry	1	$ 573.58
Outer Copper Nozzle	Xometry	1	$ 484.86
Graphite Attachment	Graphite Sales Inc.	3	$ 1,002.06
		Total	**$ 1,486.92**

TABLE 9.2: Cooling system cost comparison

Graphite Nozzle with no Cooling	
System	Cost
Feed System	$ 911.34
Support Structures	$ 426.42
Other Engine Components	$ 272.63
Nozzle	$ 668.04
Total	**$ 2,278.43**
Copper Nozzle with Active Cooling	
System	Cost
Feed System	$ 911.34
Support Structures	$ 426.42
Other Engine Components	$ 272.63
Cooling System	$ 922.52
Nozzle	$ 1,486.92
Total	**$ 4,019.83**

Based on the worst case erosion rate described in Section 7.4, a graphite nozzle can be fired twice at 4 seconds each before an unacceptable drop in performance is observed. The upfront

cost of an active cooling system is, however, significantly higher than that of a graphite nozzle with no cooling. As such, from a cost perspective, the copper nozzle with active cooling system is worth considering only if more than 10 test at 4 seconds each are planned (or more than 40 seconds of total firing time are planned).

9.4 Safety Analysis

The main safety concern with hot fire testing is the risk associated with using nitrous oxide, using high pressure equipment, the combustion reaction itself and open flames

There are four primary hazard associated with nitrous oxide:

1. It is a high vapour pressure gas at room temperature (700-800psi). To mitigate this hazard, all pipes and containers are sized to provide significant strength over the pressure. The pipe and fitting sizing follows the manufacturer's recommended maximum operating pressure and the compressed gas tank has been pre-approved by the CGA for nitrous oxide gas services. Also, because liquid nitrous expended when heated, sufficient ullage is present in storage tanks to account for temperature fluctuations.

2. The nitrous oxide's strong oxidizing qualities pose a hazard if any hydrocarbon contaminates the system.To mitigate this hazard, a strict regiment of inspecting and cleaning with an industrial strength decrease is implemented. Any parts with complex geometry that the team cannot clean themselves, such as valves, will be purchased with pre-approval for oxygen service.

3. Under high temperature or pressure, nitrous can decompose into nitrogen and oxygen in a very exothermic reaction, resulting in a runaway pressure spike potentially leading to explosion. With pure liquid nitrous oxide, this decomposition is unlikely [38]. However, contaminants such as rust or hydrocarbons can greatly increase the likelihood of decomposition [21]. Thus, the primary mitigation approach is to ensure a high level of cleanness as described in part 2.

4. Nitrous oxide is an anaesthetic, with the possibility of causing euphoria and unconsciousness after prolonged exposure. TO mitigate this, the tanks will be filled remotely using UTAT's fill system or at a conventional race car shop. The tanks will also be stored outside where the concentration due to leak will be low.

To mitigate the risk associated with open fire and high temperature equipment, all testing will be conducted at a safe distance away from any structures or personnel. All valves will be remotely actuated, and data will be collected remotely. The cooling system has been sized conservatively to provide extra factor of safety as outlined in Section 5.

HAZOP on Feed System

A hazard and operability study (HAZOP) is a systematic approach to identifying and evaluating the risks of a system on the personnel and equipment.The operational process will be reviewed to determine if deviations from the normal conditions could lead to undesired consequences. In the following section the potential causes, consequences and existing safeguards of each deviation will be listed. Additional mitigation measures will be taken if the residual risk is above threshold.

The areas of concern for process deviations are pressure, flow, temperature, thrust, power loss and the wrong material. The HAZOP study conducted outlines the key areas of concern with process safety risk and it can be seen that the system has an overall low risk. The potential for nitrous contamination with hydrocarbons or oils will be mitigated by regular maintenance and cleaning of the parts with the appropriate PPE.

Probability	Severity of Impact/Consequences			
		Minor	Moderate	Major
	Frequent	Medium	High	High
	Likely	Low	Medium	High
	Remote	Insignificant	Low	Medium

FIGURE 9.5: Risk Matrix

UTAT Test Stand HAZOP							
Paraffin-Nitrous Hybrid Rocket Engine							
Deviation	**Cause(s) [Initiating Events]**	**Consequence [worst case]**	**Existing Safeguards**	**Probability**	**Consequence**	**Risk Ranking**	**Recommendations**
High Pressure	Tank temperature > 18 C in oxidizer tank	Higher pressure in combustion chamber. Reactor could burst at 3000 psi leading to fatal inury from nitrous explosure or jet fire	Temperature maintaining sleeve for tank, pressure relief valve	Remote	Moderate	Low	
High Pressure	Tank temperature >18 C in coolant tank	Higher pressure in coolant chamber. Reactor could burst at 3000 psi leading to fatal inury from nitrous explosure or jet fire	Temperature maintaining sleeve for tank, pressure relief valve	Remote	Moderate	Low	
High Pressure	Mass flow rate is too high at injector inlet	High reaction rate in combustion chamber, runaway reaction		Remote	Moderate	Low	
Low Pressure	Oxidizer Tank temperature < 18 C	Not enough pressure drop	Temperature maintaining sleeve for tank	Likely	Minor	Low	
Low Pressure	storage bottle valve actuation failure on oxidizer line	Low reaction rate		Likely	Minor	Low	
Low Flow	Not enough nitrous in oxidizer tank	Low reaction rate		Likely	Minor	Low	Check mixture quantity prior to conducting experiments
Misdirected Flow	High Pressure in combustion chamber	Reverse flow two phased mixture, compressed gas tank explosion with flying debris	Check valve, bust disk on tank	Remote	Moderate	Low	
High Temperature	Tank temperature > 18 C in oxidizer tank. External environment too hot	External environment too hot, additional heat supplied. Reactor could burst at 3000 psi leading to fatal inury from nitrous explosure or jet fire	Temperature maintaining sleeve for tank, pressure relief valve	Remote	Moderate	Low	
Low Temperature	Tank temperature < 18 C in oxidizer tank due to external temperature	Coolant mass flow rate not sufficient leading to nozzle damage	Temperature maintaining sleeve for tank	Likely	Minor	Low	
Wrong Material	Nitrous contamination with hydrocarbons or oils in pipe/ valves	Runaway Reaction		Likely	Moderate	Medium	Regular maintenance and cleaning of parts
High thrust	Uncontrolled combustion reaction, unexpected force due to flame path blockage	Rocket eject out of the test stand, uncontrolled direction of the flame	High safety factor for test stands structural support compared to predicted thrust	Remote	Moderate	Low	All personel stand at a safe distance and structural integrity check before any test
Power Loss	Faulty electronics, damaged equipments	Cannot open feed line, cannot close feed line, cannot record any data	fail close actuator, small nitrous tank volume	Remote	Moderate	Low	Test all electronics before firing, have back up power supply on site

FIGURE 9.6: HAZOP of the Combustion System

UTAT Test Stand HAZOP							
Paraffin-Nitrous Hybrid Rocket Engine							
Copper Nozzle Specific Risks							
Low Pressure	Coolant Tank temperature < 18 C	Coolant mass flow rate not sufficient leading to nozzle damage		Likely	Minor	Low	
Low Pressure	storage bottle valve actuation failure on coolant line	Coolant mass flow rate not sufficient leading to nozzle damage		Likely	Minor	Low	Check mixture quantity prior to conducting experiments
Low Flow	Not enough nitrous in coolant tank	Coolant mass flow rate not sufficient leading to nozzle damage		Likely	Minor	Low	
Low Temperature	Tank temperature < 18 C in coolant tank due to external temperature	Not enough pressure drop	Temperature maintaining sleeve for tank	Remote	Minor	Low	
Misdirected Flow	High Pressure in nozzle cooling channels	Backflow of coolant, nozzle damage, compressed gas tank explosion with flying debris	Check valve, bust disk on tank	Remote	Moderate	Low	
Power Loss	Faulty electronics, damaged equipments	Cannot open coolant line, cannot close coolant line (nozzle damage)	fail open actuator	Remote	Moderate	Low	Test all electronics before firing, have back up power supply on site
Graphite Nozzle Specific Risks							
High flame temperature	Uneven/high erosion rate on graphite nozzle causing nozzle failure	Nozzle eject out of the engine as a high velocity projectile		Remote	Moderate	Low	All personnel stand at safe distance and not directly below engine

FIGURE 9.7: HAZOP of the Cooling System

Chapter 10

Environmental Life Cycle Analysis

The environmental and safety impacts will be assessed in the following section to identify the key areas of concern and provide a comprehensive overview of the project's impacts through a Life Cycle Assessment (LCA).

10.1 Environmental

Nitrous oxide has a global warming potential that is 265 times higher than CO2. Thus, it will be one of the key contributors to this project's environmental assessment.

In the system, the mass flow rate of the coolant is 0.72kg/s. Assuming no leakage of the nitrous oxide from the combustion line, the total CO2 equivalent of exhaust gases can be determined by taking into consideration the coolant gas being dumped out and the combustion products from the NASA CEA.

The following figure shows the NASA CEA results exiting at the nozzle.

Table 10.1: NASA CEA combustion results

Chemical	Mol Fraction
CO	2.55E-01
CO2	5.22E-02
H	7.48E-07
H2	1.89E-01
H2O	7.18E-02
NO	3.93E-11
N2	4.31E-01
O	1.53E-14
OH	4.94E-09

As can be seen through analysis of the NASA CEA combustion products, the primary contributor to green house gas emissions is the nitrous being dumped out to cool the nozzle. This far exceeds the CO2 emissions due to the high global warming potential equivalence factor. Thus minimizing the burn time even by one second would significantly decrease the environmental impacts of the project [39].

An approximate burn time of 4 seconds as opposed to 8 seconds which was the full scale launch of the UTAT record breaker would decrease emissions by 50%. At 0.72kg/s of coolant release rate for 4 seconds, 735kg of CO2 equivalent would be released into the atmosphere. This is a rate of 184kg/s of CO2 equivalent from the nitrous oxide.

On average, a passenger vehicle emits 411 grams of CO2 per mile driven[40]. Thus one 4 second engine test run would release a CO2 quantity equivalent to driving a car for 1788 miles.

An LCA was conducted as a complete "Cradle to Grave" analysis of the product. Specifically, it consists of pre-manufacturing, manufacturing, transportation, use and disposal processes. For this design, the transportation and disposal process are inconsiderable hence the environmental impact of these two processes are not addressed here. The dump cooling nozzle, made of copper, steel and graphite, and the graphite nozzle are compared in this section, regarding to the material selection, coolant use and fuel use. Since both designs require almost the same amount of fuel to drive the rocket hence the same amount of emission is produced, the impact from these two sectors can be considered as equivalent. To improve the comparability of the analysis, 2 parameters are used to evaluate the performance of the two designs - Cumulative Energy Demand (CED) and Greenhouse Gas Emissions (GHG). The conventional units are used here - BTU for energy consumption and carbon dioxide equivalent in kg for greenhouse gas emission.

Table 10.2: Material Used Comparison

	Dump Cooling Nozzle	Graphite Nozzle
Graphite Used (kg)	231.1	363
Copper Used (kg)	0.036	0
Stainless Steel Used (kg)	0.077	0
Coolant Used	2.88	0

Table 10.3: CED Comparison

	Dump Cooling Nozzle	Graphite Nozzle
Graphite Energy Used (BTU)	623.97	980.1
Copper Energy Used (BTU)	22.968	0
Stainless Steel Energy Used (BTU)	8701	0
Total CED (BTU)	9347.9	980.1

Table 10.4: GHG Emission Comparison

	Dump Cooling Nozzle	Graphite Nozzle
Graphite GHG (kg)	0.136	0.214
Copper GHG (kg)	0.005	0
Stainless Steel GHG (kg)	1.9	0
Coolant GHG (kg)	735	0
Total GHG Emission (kg)	737.04	0.214

According to the comparison, the Dump Cooling Nozzle has significantly worse performance in both CED and GHG Emission sections. Even though the Dump Cooling Nozzle has better performance and more practical significance, the relatively severe environmental impact it brings cannot be neglected if this design is selected as the preferable one.

Chapter 11

Nozzle Verification

Throughout the design and optimization process a series of lower-fidelity, simplified relations, such as the Method of Characteristics (MOC) or empirical relations for base pressure were utilized for the purpose of rapid prototyping and evaluation. Such low fidelity methods must be validated and for this purpose, the finite difference, computational fluid dynamics (CFD) method was the natural choice for high accuracy flow prediction.

The software chosen to perform the CFD analysis with was OpenFOAM. An open source C++ based CFD toolbox, it readily includes a variety of solvers written to handle differing fluid cases.

OpenFOAM has a variety of default compressible fluid solvers, including both density based solvers as well as pressure based solvers [41]. Of these the two solvers best suited for trans-sonic and supersonic compressible flows are sonicFoam, a pressure-based solver, and rhoCentralFoam, a density-based solver. SonicFoam uses a PISO (Pressure-Implicit with Splitting of Operators) algorithm and was originally developed for use with incompressible flows though later adapted for compressible flows. RhoCentralFoam on the other hand is a density-based solver that uses central-upwind schemes proposed by Kurganov and Tadmor [42]. The two solvers have been extensively used for supersonic compressible flow simulations and have thus been subject to studies comparing their performance [43] [44].

Some notable conclusions are as follows:

1. sonicFoam requires a mesh 3 times as dense in order to obtain results of comparable quality using rhoCentralFoam.
2. For identical meshes sonicFoam requires a longer computation time.
3. Prediction of Mach number, pressure and temperature has been shown to be better in rhoCentalFoam compared to sonicFoam.

For these reasons rhoCentalFoam was the solver of choice for the CFD simulation.

Boundary Conditions

A summary of the boundary conditions applied can be seen in Figure 11.1. At the inlet, combustion chamber conditions were enforced including a chamber pressure of 450 psi and a temperature of 2831.47 K. Sea level free stream conditions were enforced with an atmospheric pressure and temperature of 101325 and 298 K respectively. Additionally the free stream outlet had a wave transmissive outflow condition, allowing waves to exit the domain without being reflected. No slip boundary conditions were specified at the nozzle and combustion chamber regions. No inlet or outlet numerical boundary conditions for velocity were provided in order for the flow to be pressure driven and thus induced by the pressure difference between the combustion chamber and the atmosphere.

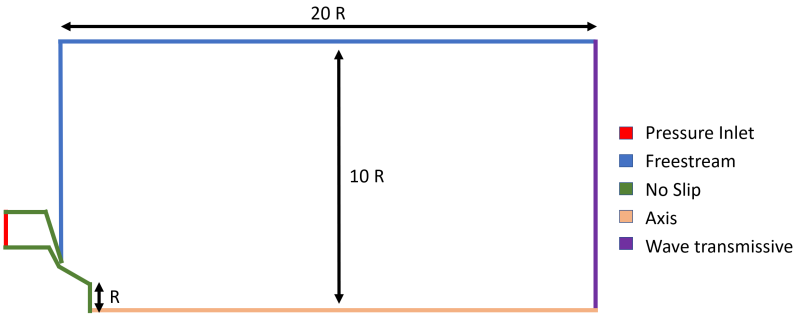

FIGURE 11.1: Boundary conditions for CFD analysis summarized

Thermophysical Models

The fluid was modelled as a pure mixture without chemical reactions. Seeing as viscosity is a strong function of temperature, and there is a wide range of temperatures present in the simulation domain, a Sutherland transport model was used to account for the temperature dependence of dynamic viscosity. The coefficients of the Sutherland model were found using curve fitting functions in Matlab, utilizing three data points, the chamber, throat and exit plane as determined by NASA CEA data. Constant values for specific heat c_p (at constant pressure) and molecular weight MW were chosen and taken at the throat as determined using NASA CEA.

The compressibility of the gas was determined using the gas constant and temperature as $\psi = (RT)^{-1}$. Based on the compressibility and changes in pressure, the density was then determined using the ideal gas law.

Turbulence modelling

The most common RANS turbulence models:

1. Standard and extended $k - \epsilon$
2. $k - \omega$ shear-stress transport (SST) model
3. $v^2 - f$ and realizable $v^2 - f$ models

For the purposes of shock wave position and flow separation in nozzle problems the $k - \omega$ SST and realizable $v^2 - f$ models give the best results. However as the $k - \omega$ SST model has two fewer transport equations, it is computationally cheaper to implement. As such, turbulence was modelled using a high Reynolds $k - \omega$ SST model. A turbulence intensity of 5% was used and a turbulent length scale of 3.8% percent the hydraulic diameter of the combustion chamber was chosen as recommended by industry [45].

Geometry and Mesh

The geometry of the CFD domain was created in Solidworks. A detailed mesh of 912,120 hexahedral elements was created, as seen in Figure 11, with an average orthogonal mesh quality is 0.91. This mesh is biased towards the diverging portion of the nozzle and towards the symmetry plane where the plume will extend. A detailed portion of the throat region can be seen in Figures 11.3.

FIGURE 11.2: Final hexahedral mesh for CFD

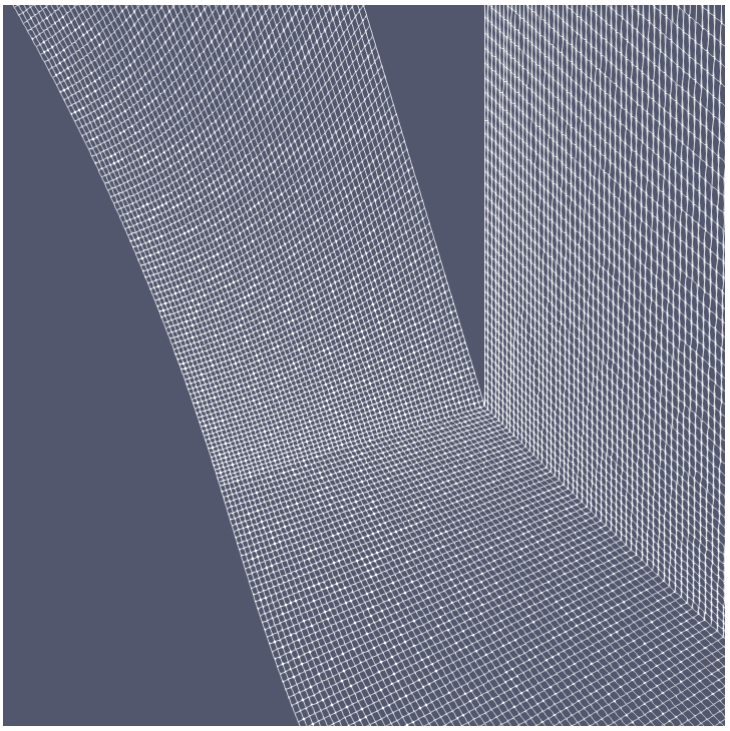

FIGURE 11.3: Final hexadral mesh for CFD, Throat Detail

Initial simulation

As a general rule, for the initial time-step all fluid conditions at the boundaries of the domain must be well defined. In addition to this often it is required to provide an initial "guess" for the solution of the flow field, something which can often prove difficult when faced with ch alleging geometries or complex fluid conditions. A poor initial guess for the flow field could cause the solution to diverge rapidly, or experience oscillations which are not able to be damped out preventing the solution from reaching steady state. Initializing supersonic flow is particularly challenging and simply allowing a pressure difference to accelerate the flow from stagnant conditions in a nozzle will simply cause choking to occur at the throat and the flow will not transition to supersonic [46]. In this simulation the flow was initialized as many shock tube problems are, with a sharp separation of upstream and downstream conditions located directly at the throat as seen in Figure . As the computational domain is quite large, approximately 10 times the characteristic radius in width and 20 times the characteristic radius in length, as seen in Figure 11.1, the full development of the nozzle plume would be require the bulk of the simulation time. In order to minimize the time until a steady solution, the previously discussed coarse mesh was utilized and the Courant number was dropped to 0.1 in order to assure stability in the initial development of the solution. After 0.0035 seconds the flow appeared to have reached steady state as marked by the residuals all dropped below $1e^{-6}$ and flattened out. The flow field developed through the entire computational domain but the coarse nature of the mesh meant that flow structures in the plume could not be accurately resolved.

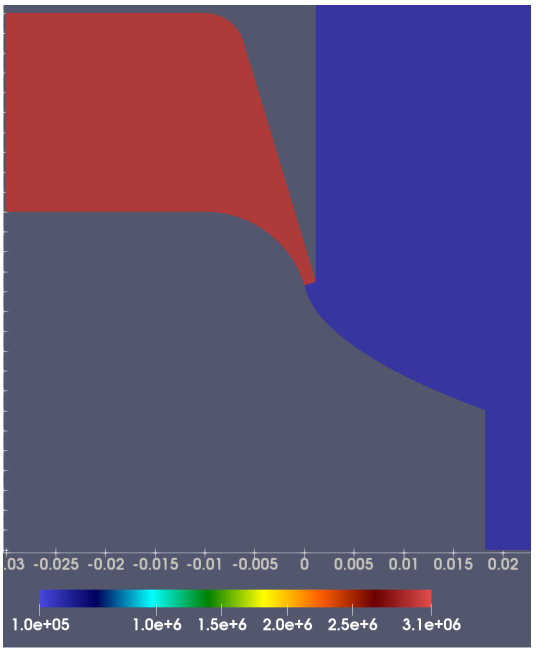

FIGURE 11.4: Initial conditions for pressure field (Pa)

Detailed simulation

The initial solution generated could not fully resolve the detailed features of the flow field a‘s the mesh utilized was too coarse. The solution of the 0.0035s time-step was then interpolated to the finer mesh thus providing an excellent initial guess of the entire flow field. As the flow field was already developed and thus initialization stability concerns were not relevant any longer the Courant number was increased to 0.5 in order to speed up the computation. The solution was allowed to advance a further 0.0005s until 0.0040s at which time the solution had become sufficiently stable and the flow structures had become fully resolved.

Discussion

Plots of the Mach number and temperature for the final simulation can be seen in Figures 11.6 and 11.7 respectively. The generation of these plots have two important consequences, they serve to validate the method of characteristics technique for determining flow characteristics near the nozzle curves, as well as provide information about the plume past the diverging section. The property plots generated using the method of characteristics are of exceptionally high quality for a full length aerospike nozzle, they get however progressively worse as the truncation of the aerospike increase, particularly near the base region of the nozzle where MOC fails and one must use empirical relationships. The CFD simulation however is able to predict with confidence this base region. It can be seen when comparing Figure 11.6 and 6.8 that the empirical relations for the base region predict a relatively small open wake region near the base of the nozzle when compared to the CFD results. Additionally, the empirical prediction gets progressively worse further away from the nozzle and begins to predict Mach numbers much higher than present in

the CFD. It would appear that the empirical relations work best at sea level as the region where the non-physical Mach numbers appear becomes larger at the design altitude when compared to sea level as seen in Figure 6.7.

Despite the shortcomings discussed, the empirical relation remains an acceptable prediction of the open wake region near the base for the purposes of rapid results when performing optimization, care must be taken however when interpreting the results increasingly far from the base of the nozzle and at increasingly high altitudes.

A numerical Schlieren plot was created by taking the first derivative of density with respect to space in order to study the flow features. The flow features were compared against past experimental data and the results matched up closely. The most notable flow features are labelled in figure 11.5.

Detailed plots of the most important variables, namely Mach number, temperature, pressure and density, along the diverging section of the nozzle can be found in Figures 11.8, 11.9, 11.10, 11.11 respectively.

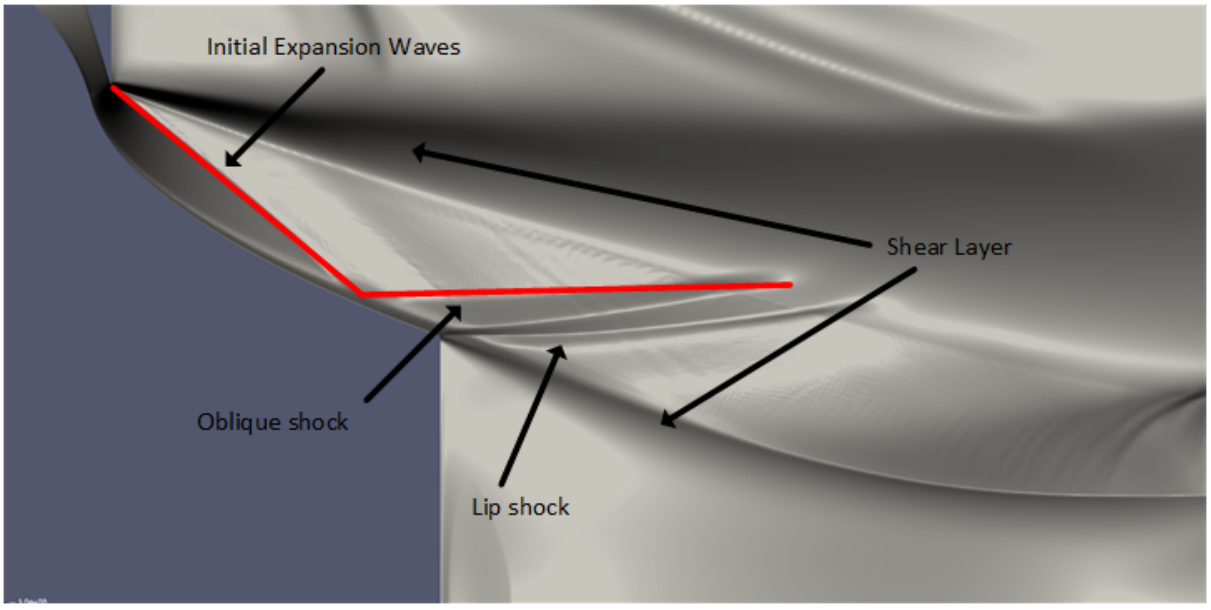

FIGURE 11.5: :
Schlieren CFD with Labelled Flow Features

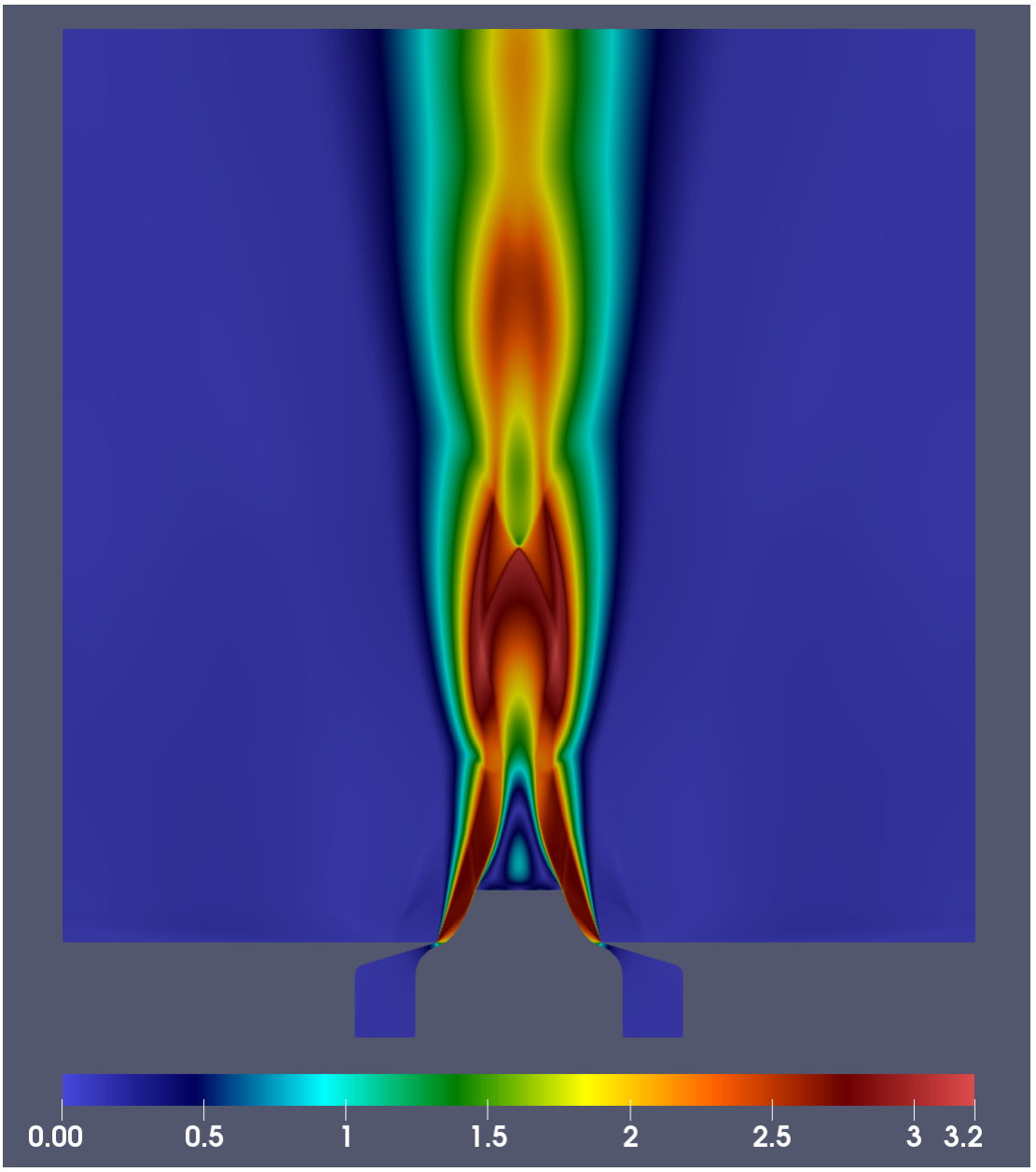

FIGURE 11.6: Mach contour at sea level (Ma)

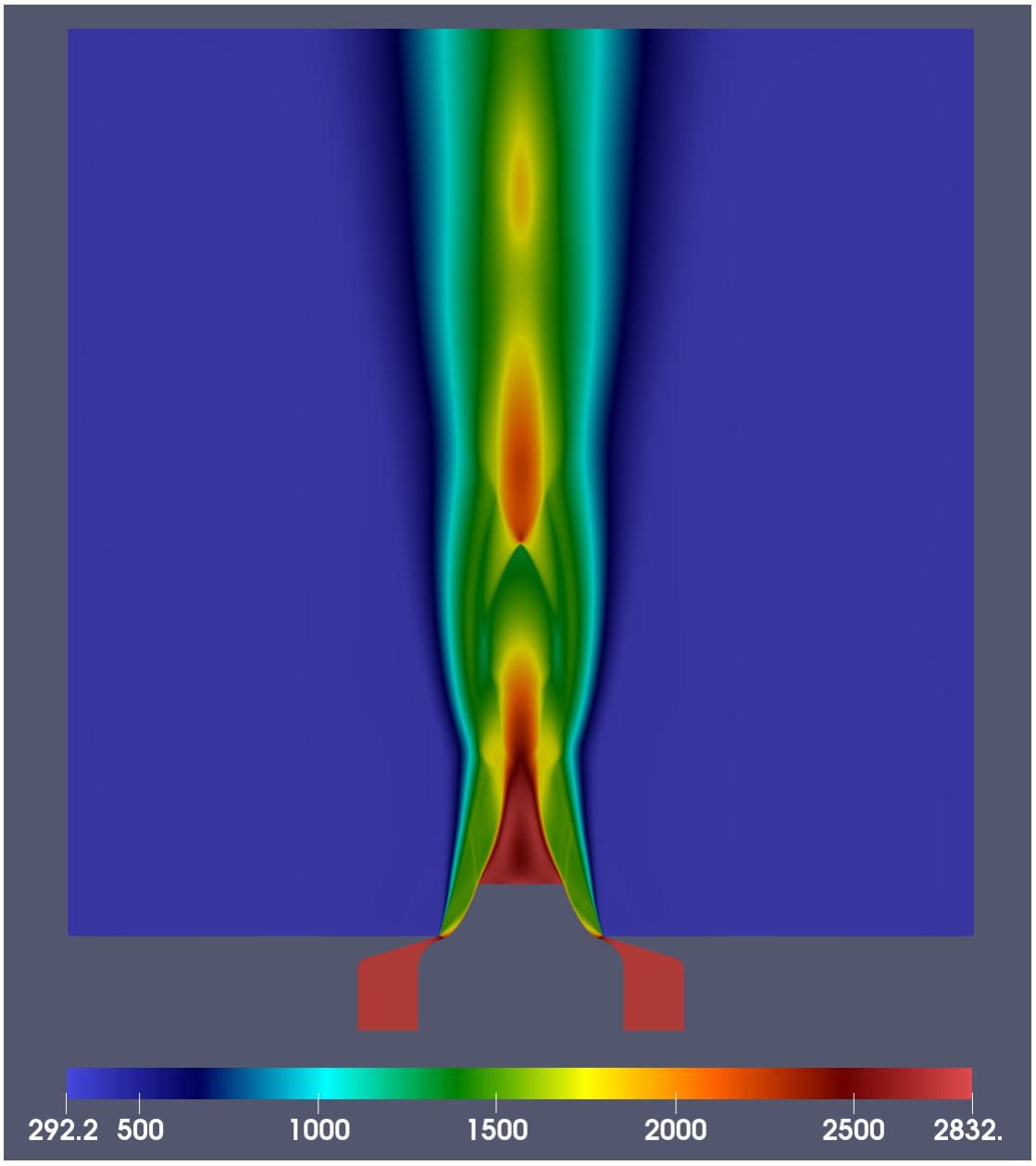

FIGURE 11.7: Temperature contour at sea level (K)

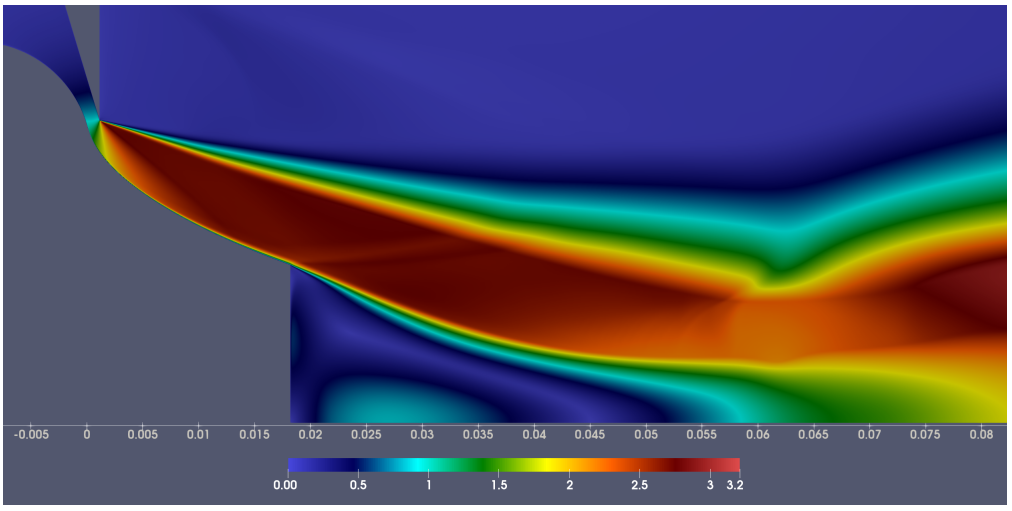

FIGURE 11.8: Mach contour at sea level along diverging and open wake region (Ma)

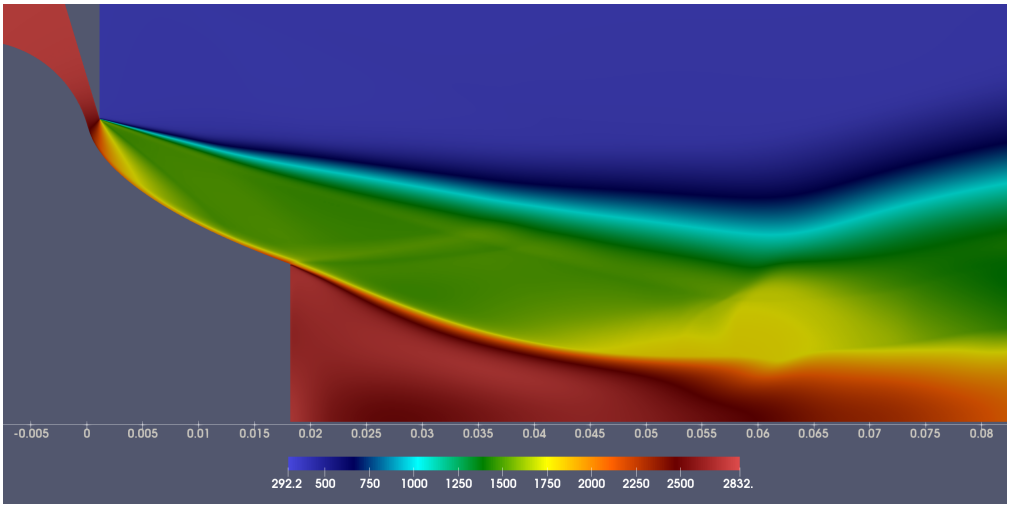

FIGURE 11.9: Temperature contour at sea level along diverging and open wake region (K)

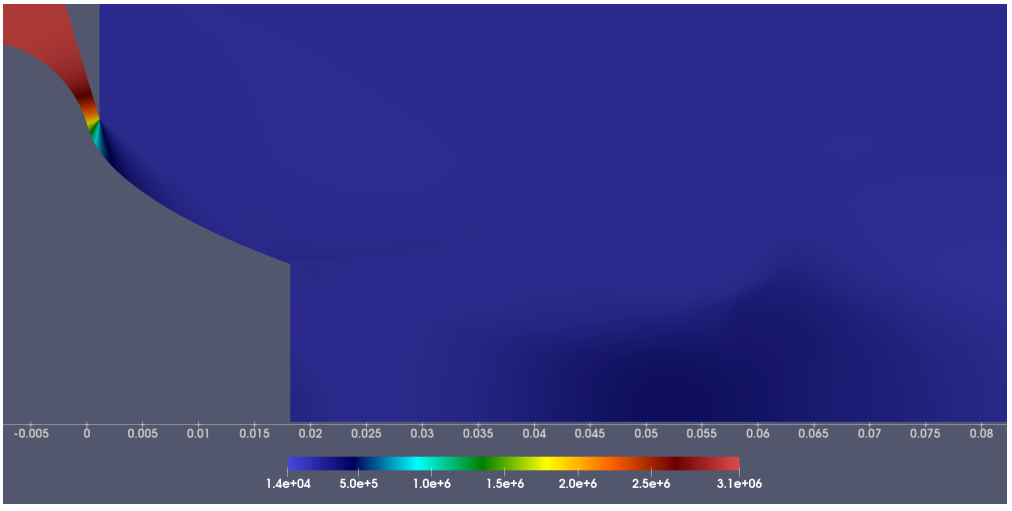

FIGURE 11.10: Pressure contour at sea level along diverging and open wake region (Pa)

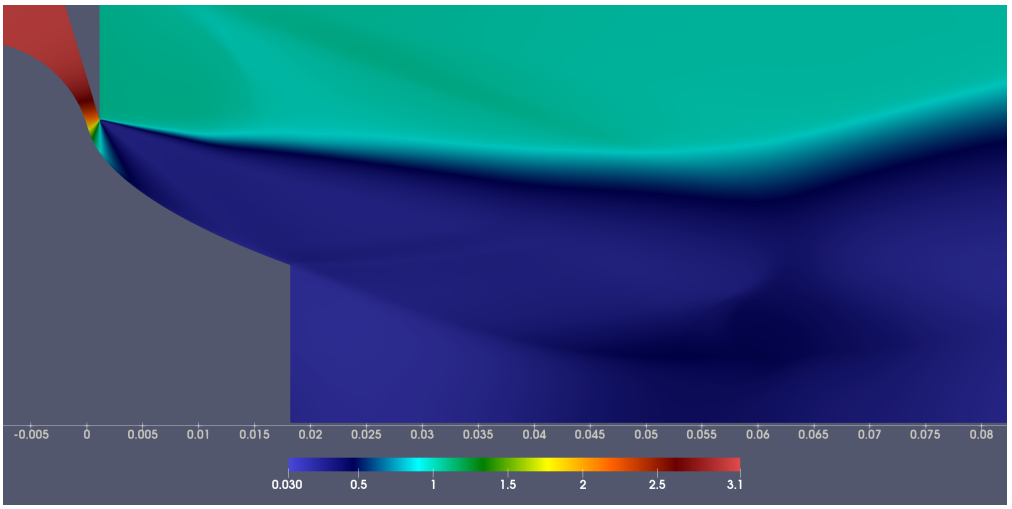

FIGURE 11.11: Density contour at sea level along diverging and open wake region (kg/m^3)

11.1 Bell Nozzle Performance Comparison

Finally, having designed an aerospike nozzle, we are able to compare its performance to that of a conventional bell nozzle designed for a similar altitude. Onofori et. al provides experimental data for an aerospike nozzle truncated to 20% of its original length compared to a conventional bell nozzle (see Figure 11.12 below).

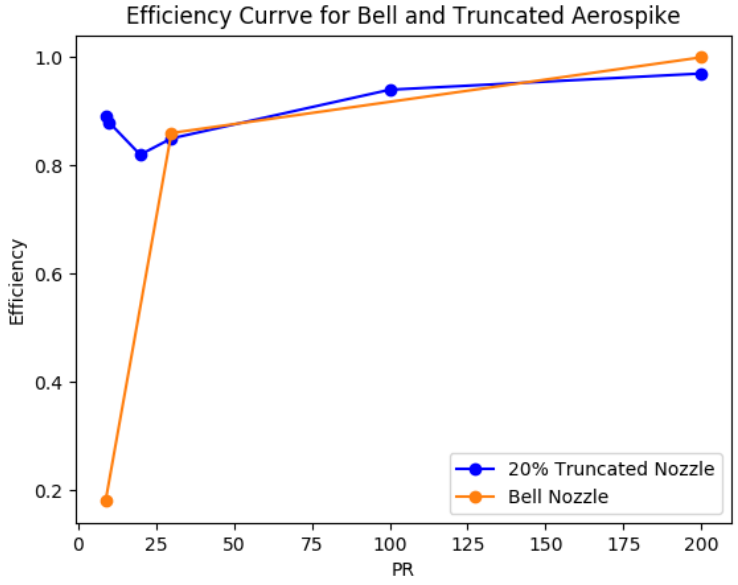

FIGURE 11.12: Experimental η Curves for Bell and Aerospike Nozzle [3]

Taking the average value of the efficiency curves over their flight range, we find that the average thrust efficiency of our aerospike nozzle would be approximately 92%. Similarly, the average

efficiency of a conventional bell nozzle designed for the same altitude would have an efficiency of 88%. Using this average efficiency coefficient, it is possible to estimate the maximum apogee of the UTAT record breaker rocket assuming it was using an aerospike as opposed to a bell nozzle. This was done through an in-house MATLAB simulation which determines the burn time, associated thrust and resulting altitude. As can be seen in figure 11.13 if Defiance utilizes a bell nozzle the apogee at for the current engine configuration is 47,800 feet, with an aerospike the apogee becomes 51,200 feet. The improved efficiency the aerospike brings translates to a 7.2% increase in apogee, an immense boost in performance. The associated thrust profile for the liquid N_2O and gaseous N_2O phases of the burn, for the two separate nozzles can be seen in figure 11.14.

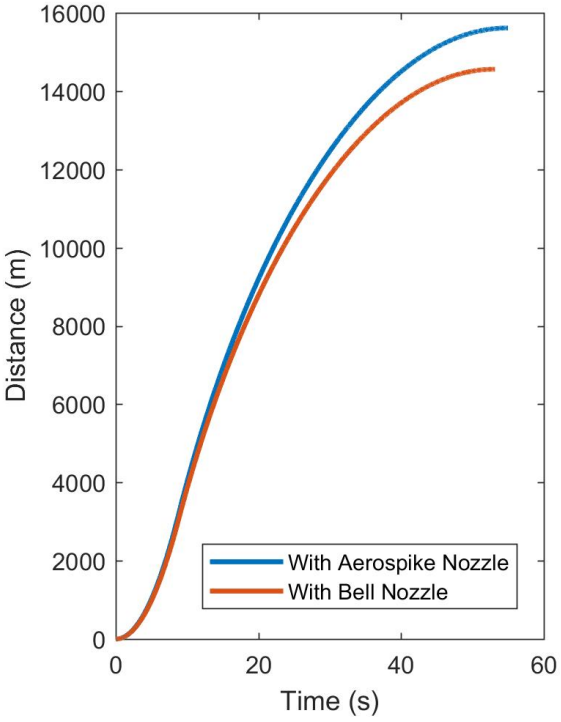

FIGURE 11.13: Defiance Flight Profile for Differing Nozzles

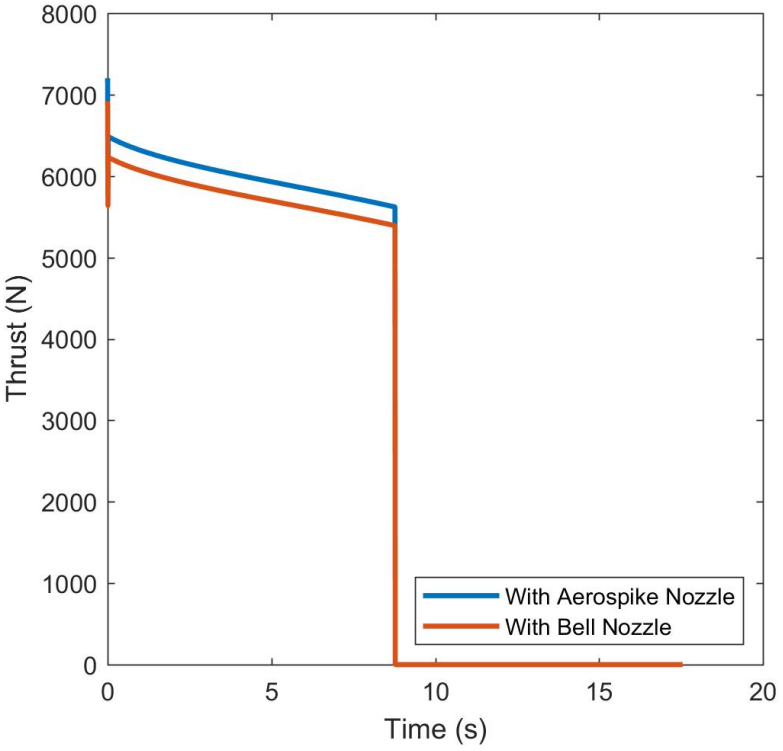

FIGURE 11.14: Defiance Thrust Profile in Flight for Differing Nozzles

Chapter 12

Conclusion

With reference to section 1.2 , the following evaluation is made against each of the objectives outlined at the start of the report:

1.1 The aerospike nozzle is able to expand and accelerate the combustion gas resulting in a predicted thrust of 120 N, and a nozzle efficiency of 92 % averaged over all altitudes.

1.2 The test stand engine is designed with similitude scaling factor in mind, and is a scaled down version of the current UTAT rocket, Defiance.

1.3 The graphite nozzle can only be re-used 3 to 5 times giving a predicted erosion rate of 0.03 mm/s to 0.05 mm/s, which is less than the current UTAT graphite bell nozzle that can be used for 7 to 8 times. The copper nozzle however, is reusable beyond 7 to 8 times under normal operating conditions.

2.1 A HAZOP analysis analysis has been conducted, and all risk related to using nitrous oxide, high temperature and high pressure equipment are reduced to medium or below. Safety factor are built into the heat flux prediction, coolant prediction and mechanical design through the use of FEA.

3.1 All mechanical design components are manufacturable. Specifically, the team worked with the machine shops to reduce the cost of graphite components. The machine shop initially reported cost of over $3000, and the team were able to reduce the price down to $668.

3.2 All testing equipment, if possible, were sourced from Misumi USA to reduce cost as UTAT has a sponsorship relationship with this vendor. All components that can be salvaged from previous UTAT test stand will be re-used. Simple metal parts such as flanges will be manufactured in house at the University to reduce cost.

4.1 CFD analysis using OpenFOAM and FEA analysis using ANSYS have been used to predict nozzle and engine performance.

4.2 Only two variables were used in the optimization algorithm, given more time, more engine variables could have been incorporate to give a more complete optimization.

4.3 Unfortunately, due to the high cost, UTAT did not have enough resources to support the construction of a test stand. No testing data were collected.

4.4 Average efficiency of our nozzle was found to 92 %, a conventional bell nozzle would have an average efficiency of approximately 88 %.

4.5 All calculation methods outlined in this report can be applied to any rocket size. However, the exact range of scalability has not been determined.

5.1 The copper nozzle with active cooling performs significantly worse in terms of environmental impact due to the release of nitrous oxide for cooling during testing. The firing time has been designed to be only 4 seconds to reduce the release on un-burned nitrous oxide.

In this report, the design process of a hybrid rocket aerospike nozzle for a test stand application was outlined in detail. The design process started with the engine requirements, followed by the nozzle contour design, cooling system design, optimization and mechanical design. Two resulting designs were proposed: the copper nozzle with active cooling and the graphite nozzle with no cooling.

Cost, environmental and safety analysis were also conducted to offer additional design considerations. Nozzle performance was then evaluated using CFD and its performance was compared to a standard bell nozzle showing the increased performance. Using the methods outline in this report, UTAT will be able to make an informed decision on how to design an aerospike nozzle and the appropriate cooling system giving any test stand requirement.

Appendix A

Engine Parameters

Main design parameters	Cpstn	Rcrd			Combustion Chamber	Cpstn	Rcrd		
P_{ox} (kPa)	4826330.105	4826330.105			CC NPS	3	5		
P_{cc} (kPa)	3102640.782	3102640.782			CC SCH	40	10		
OF	4.5	4.5			CC OD (m)	0.089	0.141	5.562992126	
Me	2.90				CC Thickness (m)	0.005	0.003		
ε	5.29				CC ID (m)	0.058	0.134	5.75	
					Liner Thickness (m)	0.005	0.005	5	
Flight Design Paramters	Cpstn				CC Working ID (m)	0.047	0.123		
Target Altitude (ft)	30000								
Target Altitude (m)	9144				CC Full Length (m)	0.3048	1		
Cutoff Altitude (m)	1500.000048				Pre-Combustor Length (m)	0.047	0.140		
Patm (kPa)	84548.48945				Post-Combustor Length (m)	0.047	0.123		
PR (Pcc/Patm)	36.69658444				CC Component Length (m)		0.02311		
				Ratio of Specific Heats	γ	1.237	1.2343		
				Molar Mass of Combust	MW (g/mol)	23.113	23.103		
Mass & Flow Rates	Cpstn	Rcrd		*Combustion Flame Tem*	$T_{cc} = T_f$ (K)	2831.47	2825.98		
$G_{ox,\ initial}$ (kg/m^2-s)		700		*Combustion Efficiency*	η_{c^*}	0.9	0.9		
$\dot{m}_{ox}$ (kg/s)	0.899716548	2.8		*Nozzle Efficiency*	λ	1	0.9		
$\dot{m}_{fuel}$ (kg/s)	0.199937011	0.620240027		*Gas Constant*	R (J/kg*K)	360	360		
m_{ox} (kg)		22.8727626		*Characteristic Velocity*	c* (m/s)	1385.40	1385		
m_{fuel} (kg)		5.082836133							
$\dot{m}_{prop}$ (kg/s) Non-Ideal	1.099653559	3.411320148							
$\dot{m}_{prop}$ (kg/s) Ideal	0.989688203								
m_{prop} (kg)		27.95559873							
	Fuel Grain	Cpstn	Rcrd		Full Nozzle	Cpstn		Similarity Parameters	Rcrd
	Fuel Grain OD	0.047	0.123		Me	2.90		L∝ Dp	**9.986013986**
	Initial Port Ar	0.000414569	0.003987257		ε	5.29		$\dot{m}$ox / Dp	**39.16083916**
	Initial Port Di	0.022974905	0.0715		Ae (m2)	0.0026		Gox * Dp	50.05
	Final Port Diameter (m)		0.121057137		At (m2)	0.00049			
	Web Thickness (m)		0.024902968		At, Plug (m2)	0.0021			
					De (m)	0.058			
					Dt, Plug (m)	0.052			
	Grain Length	0.22942772	0.714		Truncated Nozzle	Cpstn			
					ε	4.29			
					Ae (m2)	0.0026			
					Ae, Plug (m2)	0.00049			
					At (m2)	0.00049			
Density of Parafin Wax	rho (kg/m3)	950	950		At, Plug (m2)	0.0021			
Regression Rate Coefficien	a0	0.000155	0.000155		De (m)	0.058			
Flux Exponent	n	0.5	0.5		De, Plug (m)	0.025			

FIGURE A.1: Summary of Engine System Parameters

Appendix B

Modified Shah Correlation

This section outlines the detailed calculation procedure for estimating nitrous oxide's heat transfer coefficient using Shah's correlations and a modified boiling number [27] [28].

The goal of this correlation is to estimate the two phase multiplier factor, ψ, that relates the single phase and the two phase heat transfer coefficient. The correlation make use of the three dimensionless numbers listed in equations B.2 - B.4. This correlation can also be used for channel geometry other than circular tubes by replacing D with D_{HYD}.

$$\psi = \frac{h_c}{h_{liq}} \tag{B.1}$$

$$Co = (\frac{1}{x} - 1)^{0.8}(\frac{\rho_g}{\rho_l})^{0.5} \tag{B.2}$$

$$Bo_{eff} = 0.35Bo = 0.35\frac{q"}{G\Delta h_{vap}} \tag{B.3}$$

$$Fr = \frac{G^2}{\rho_l^2 gD} \tag{B.4}$$

The liquid phase heat transfer coefficient can be computed using the Dittus-Boelter correlation.

$$h = 0.023\left[\frac{G(1-x)D}{\mu_l}\right]^{0.8} Pr_l^{0.4}\frac{k_l}{D} \tag{B.5}$$

The Shah correlation defines three region of boiling regime, the nucleate boiling regime (ψ_{nb}), the convective boiling regime (ψ_{cb}) and the bubble suppression regime (ψ_{bs}) where both bubble nucleation and convective effects are significant. The region in which the system operated depends on the convection and Froude's number outlined in equation B.6 - B.11 below.

$$N = \begin{cases} Co, & Vertical\ tubes\ and\ horizontal\ tubes\ with\ Fr_l \geq 0.04 \\ 0.38Fr_l^{-0.3}Co, & horizontal\ tubes\ with\ Fr_l \leq 0.04 \end{cases} \tag{B.6}$$

$$F = \begin{cases} 14.7, & for\ Bo \geq 11 \times 10^{-4} \\ 15.43, & for\ Bo < 11 \times 10^{-4} \end{cases} \tag{B.7}$$

$$\psi_{cb} = \frac{1.8}{N^{0.8}} \tag{B.8}$$

For $N > 1.0$,

$$\psi_{nb} = \begin{cases} 230Bo^{0.5}, & for\ Bo > 0.3 \times 10^{-4} \\ 1 + 46Bo^{0.5}, & for\ Bo < 0.3 \times 10^{-4} \end{cases} \tag{B.9}$$

For $0.1 < N \leq 1.0$,

$$\psi_{bs} = F\,Bo^{0.5} exp(2.74N^{-0.1}) \tag{B.10}$$

For $N \leq 0.1$,

$$\psi_{bs} = F\,Bo^{0.5} exp(2.74N^{-0.15}) \tag{B.11}$$

Depending on the value of N, the two phase multiplier is the max of the two calculated regimes.

$$\psi = max(\psi_{nb}, \psi_{cb}), \quad for\ N > 1.0 \tag{B.12}$$

$$\psi = max(\psi_{bs}, \psi_{cb}), \quad for\ N \leq 1.0 \tag{B.13}$$

For the test stand nozzle cooling channels, because there is a heat input to the coolant, the quality of the nitrous oxide changes along the length of the nozzle. Though small, there is also a frictional and acceleration pressure drop. This means that the heat transfer coefficient will not be constant along the length of the nozzle. A numerical approximation calculation is used where the heat transfer coefficient at every node along the axial direction of the nozzle is computed.

The cooling channels operate in the nucleate boiling regime for the converging section and then transition to the bubble suppression regime for the diverging section with an average convection number of 0.85 and an average two phase multiplier factor of 30.4.

Appendix C

Detail Bill of Materials

This section list the detailed bill of materials for all sub system of the test stand, engine and nozzle. The measurement devices such as load cells, pressure gauges and thermostats are not included in this list as UTAT can provide them for free. Electronics that are part of the avionic system are not included either as the current UTAT avionic system can be reused.

Table C.1: Support Structure Bill of Materials

Component	**Vendor**	**Part Number**	**Quantity**	**Cost**
T-Shaped - Base Mount Split	Misumi	U-SHPTM0.38-H0.75	4	$ 187.44
Connecting rod	McMaster-Carr	24" Overall Length, 3/8"-24 Thread	2	$ 22.60
Brackets	Misumi	GFBL8-4545-200	2	$ 72.50
Extrusion - 800mm	Misumi	HFS8-4545-800	2	$ 37.76
Extrusion - 200mm	Misumi	HFS8-4545-200	2	$ 12.76
Extrusion - 140mm	Misumi	HFS8-4545-140	4	$ 25.52
AL 6061 T6 plate 7x7inches	Metal Super Market	n/a	1	$ 28.00
Brackets - 8 series	Misumi	HBKTST8-SEC	8	$ 39.84
			Total	**$ 426.42**

Table C.2: Feed System Bill of Materials

Component	**Vendor**	**Part Number**	**Quantity**	**Cost**
Nirous Oxide	Holley	n/a	10lb	$ 100.00
Ntrrous Oxide Tank	Fastlan N2O system	PN 7048 (10lb)	1	$ 288.70
Safe Burst Disk	Fastlan N2O system	PN 7053	1	$ 38.72
Remote Bottle Opener	Nitrous Express	n/a	1	$ 110.00
1/2" Piping	Misumi	SKER12.7-100	30 cm	$ 39.42
Male Fittings	Misumi	SKTGK12.7-4	3	$ 87.69
Check valve	Misumi	CHT4V	1	$ 246.81
			Total	**$ 911.34**

Table C.3: Cooling System Bill of Materials

Component	**Vendor**	**Part Number**	**Quantity**	**Cost**
Nirous Oxide	Holley	n/a	10lb	$ 100.00
10lb Ntrrous Oxide Tank	Fastlan N2O system	PN 7048	1	$ 288.70
Safe Burst Disk	Fastlan N2O system	PN 7053	1	$ 38.72
Remote Bottle Opener	Nitrous Express	n/a	1	$ 110.00
1/2" Piping	Misumi	SKER12.7-100	3	$ 39.42
5/16" Piping	Misumi	SKER8-50	1	$ 11.18
Male Fittings	Misumi	SKTGK12.7-4	3	$ 87.69
Check valve	Misumi	CHT4V	1	$ 246.81
			Total	**$ 922.52**

Table C.4: Engine and Other Components Bill of Materials

Component	**Vendor**	**Part Number**	**Quantity**	**Cost**
Oil-Resistant Buna-N O-Ring	McMaster-Carr	No 2-040	1	$ 17.39
High-Temperature Silicone O-Ring	McMaster-Carr	No 2-037	1	$ 5.61
High-Temperature Silicone O-Ring	McMaster-Carr	No 2-127	1	$ 6.51
Retaining ring stock	n/a	3.25" OD, Aluminum 6061-T6 round bar, 1" long	1	$ 28.30
Nozzle assembly retainer stock	n/a	5.250" OD, Aluminum 6061-T6 round bar, 1.25" long	1	$ 29.36
Stainless Steel Helical Insert	McMaster-Carr	#18-8	1	$ 5.51
Black-Oxide Alloy Steel Socket Head Screw	McMaster-Carr	#10-32, 7/16" long	1	$ 13.04
Aluminum Washer	McMaster-Carr	#10	1	$ 5.52
Black-Oxide Alloy Steel Socket Head Screw	McMaster-Carr	#10-32, 5/8" long	1	$ 13.26
Injector assembly stock	n/a	5.250" OD, Aluminum 6061-T6 round bar, 2.25" long	1	$ 40.98
injector retainer stock	n/a	3.25" OD, Aluminum 6061-T6 round bar, 1" long	1	$ 21.94
Injector stock	n/a	2.125" OD, Aluminum 6061-T6 round bar, 1" long	1	$ 17.12
combustion chamber pipe	n/a	3" ID SCH 40 pipe, Aluminum 6061-T6, 18.5" long	1	$ 40.19
Aluminum Threaded Rod	McMaster-Carr	3/8"-16, 2' Long	2	$ 20.36
Steel Flange Nut	McMaster-Carr	3/8"-16	1	$ 7.53
Paraffin Wax	n/a		n/a	$ -
EPDM liner	n/a	0.2" thick	n/a	$ -
			Total	**$ 272.63**

Appendix D

Engineering Drawings of the Graphite Nozzle Design

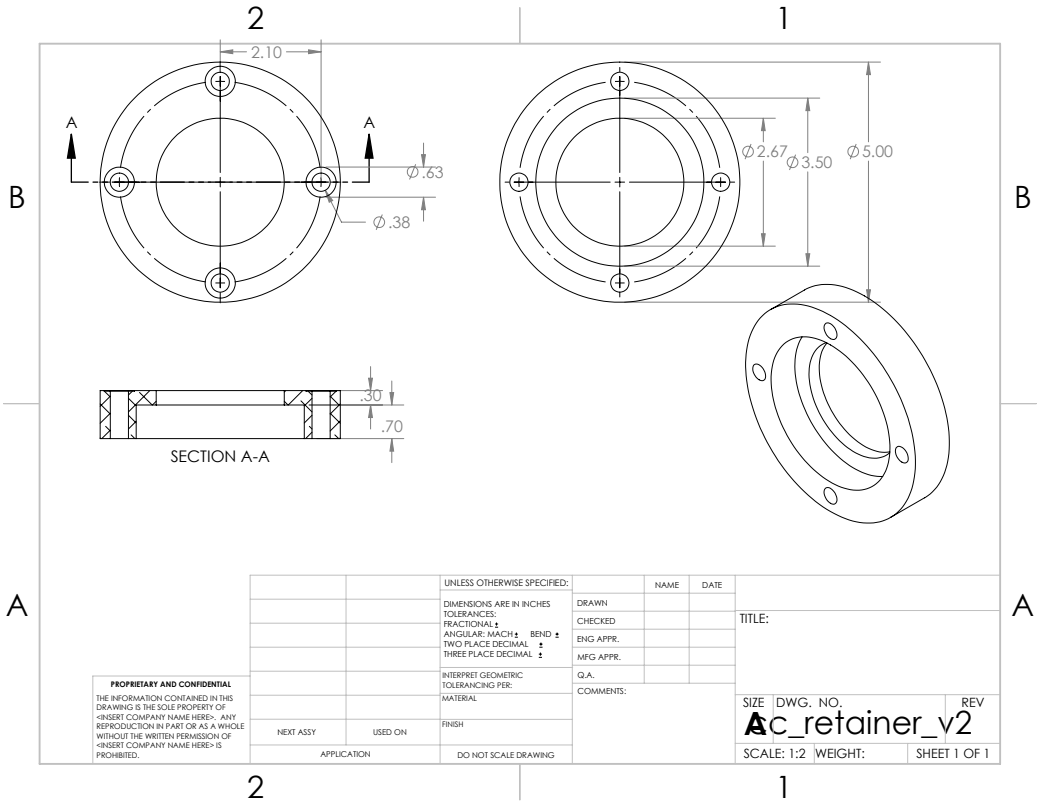

FIGURE D.1: Retainer of Combustion Chamber

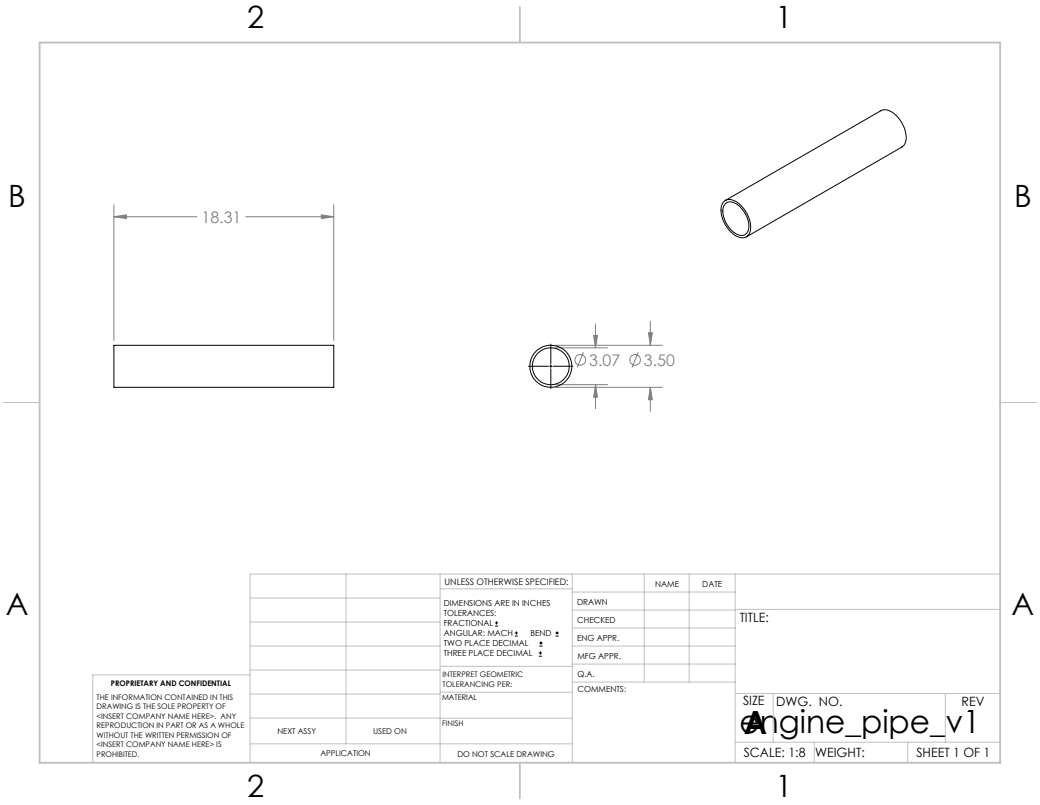

FIGURE D.2: Engine Pipe

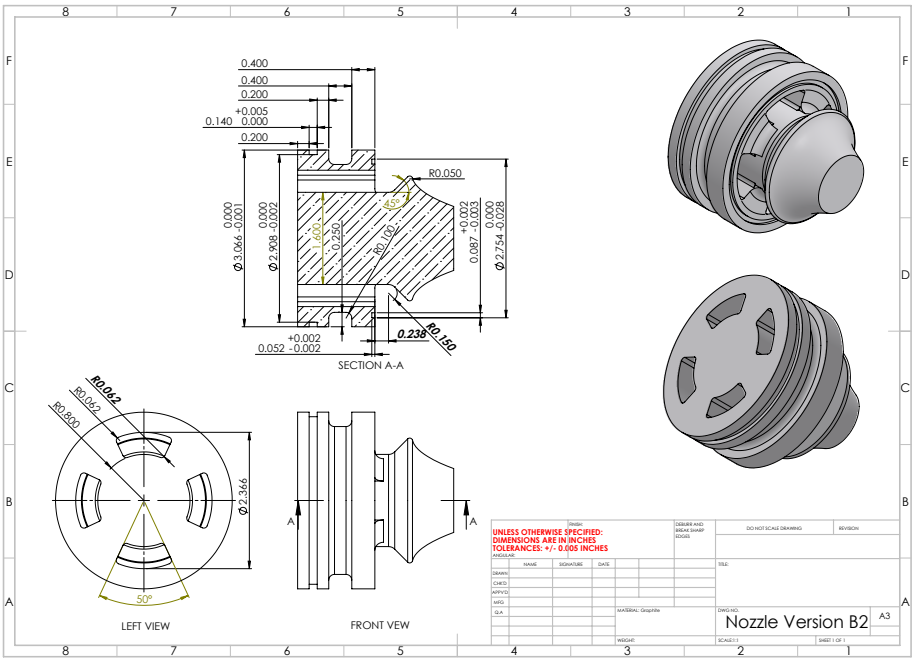

FIGURE D.8: Graphite Nozzle Version 2

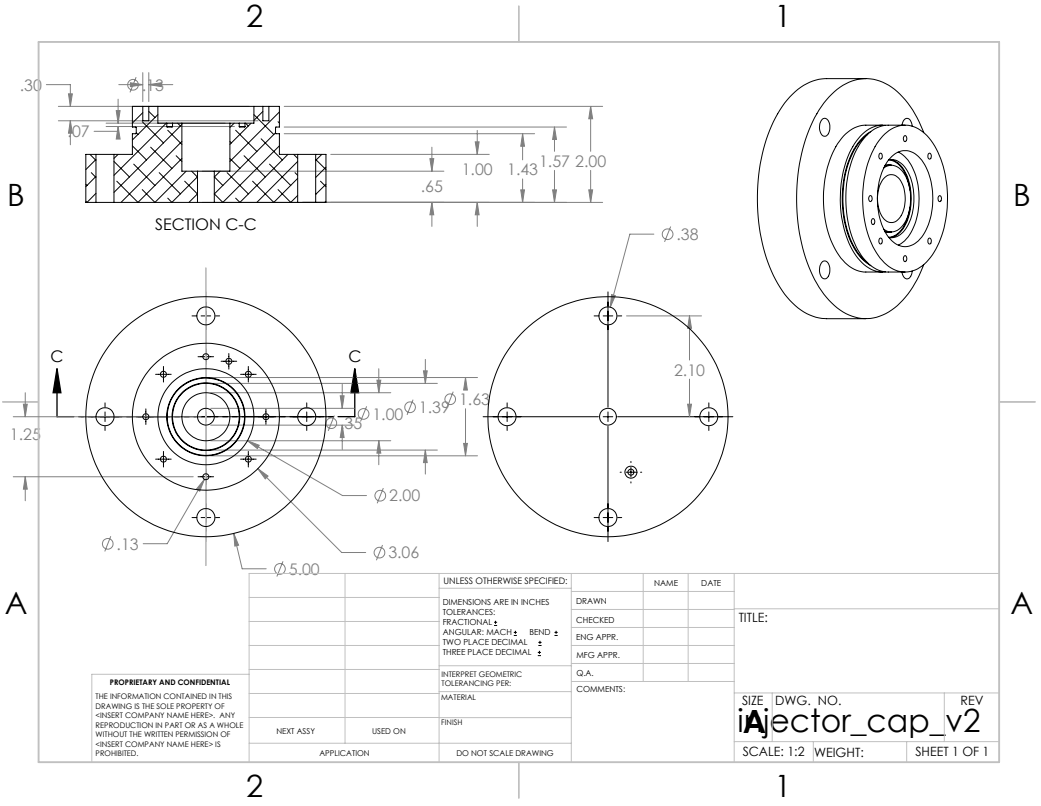

FIGURE D.3: Injector Cap

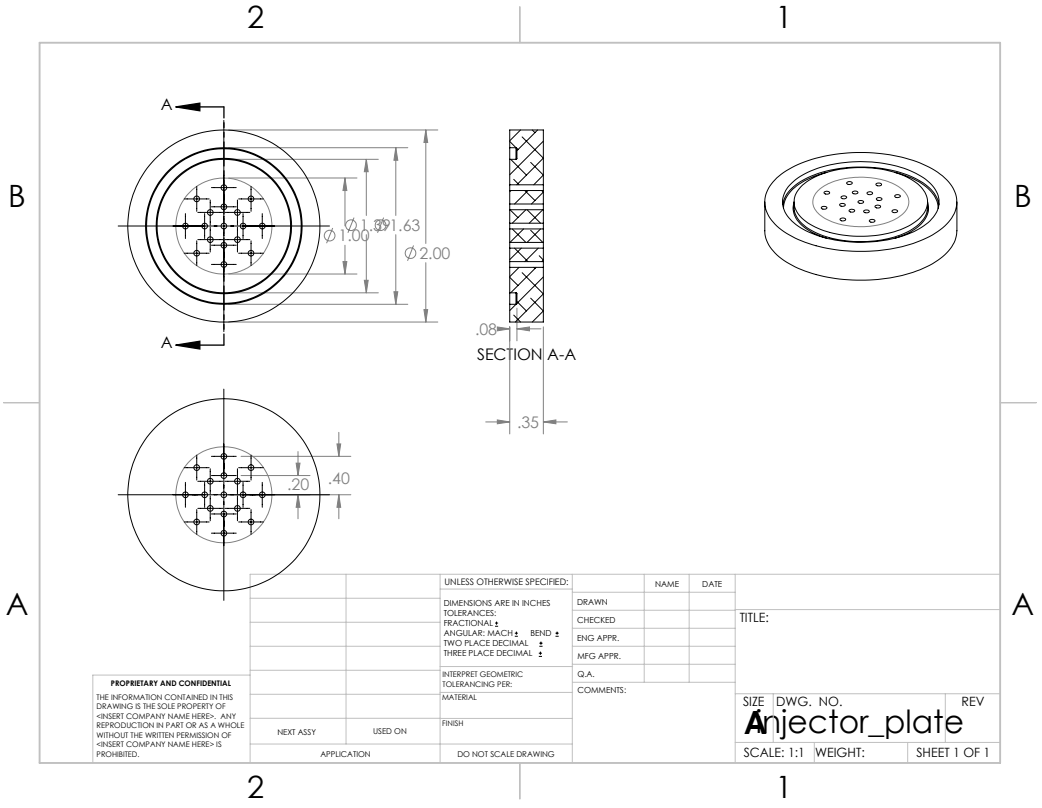

FIGURE D.4: Injector Plate

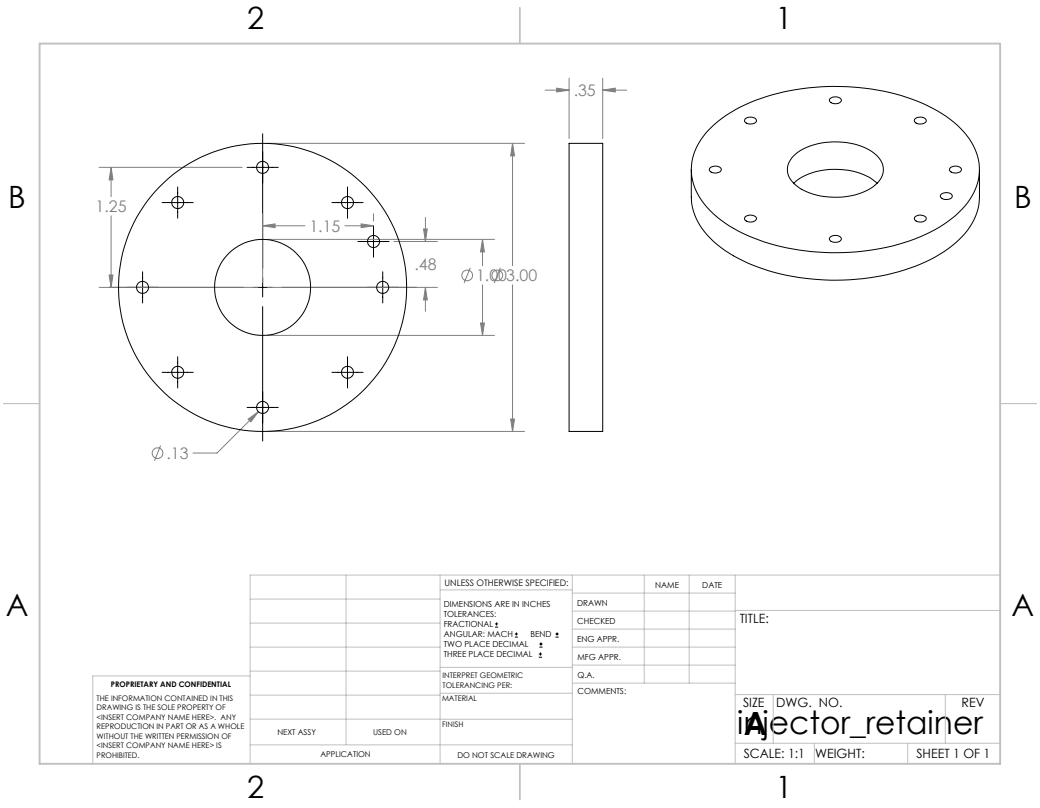

FIGURE D.5: Injector Retainer

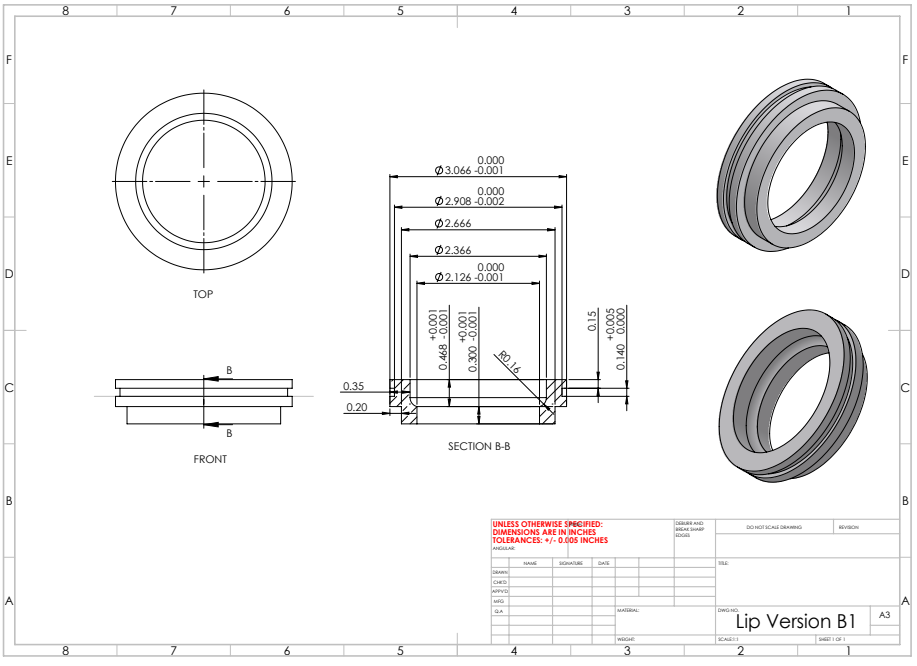

FIGURE D.6: Graphite Lip

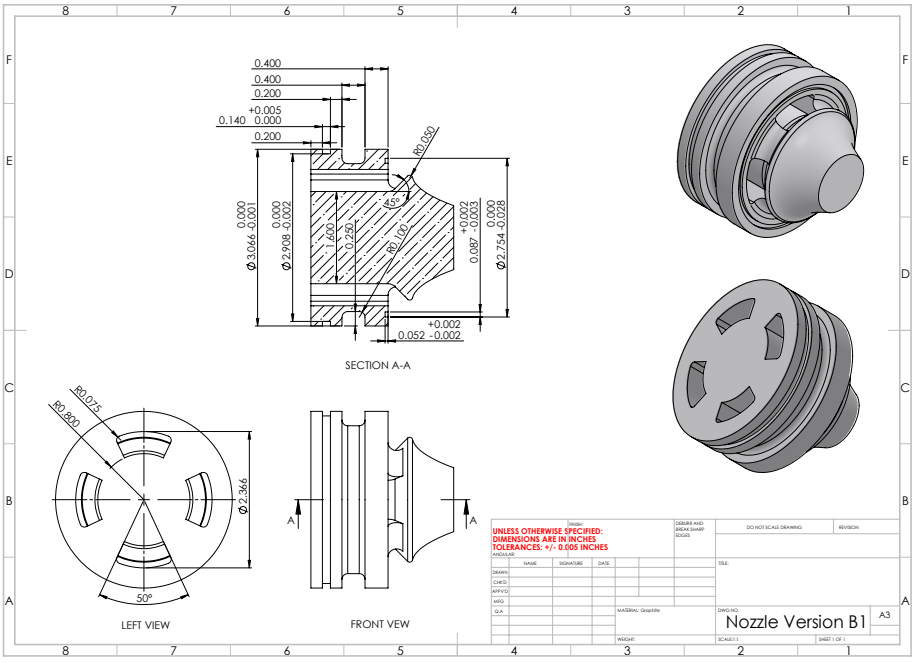

FIGURE D.7: Graphite Nozzle Version 1

Bibliography

[1] Gianfranco Angelino. Approximate method for plug nozzle design. *AIAA Journal*, 2: 1834–1835, 1964.

[2] E. Mayer. Analysis of convective heat transfer in rocket nozzles. *ARS Journal*, 31:911–917, 1961.

[3] Marcello Onofri. Plug nozzles: Summary of flow features and engine performance. January 2006.

[4] A. Gany D. Swami. Analysis and testing of similarity and scale effects in hybrid rocket motors. *Technion-Israel Institute of Technology, Haifa*, 2001.

[5] G.P. Sutton. Rocket propulsion element. *Wiley*, 2009.

[6] A.P. Trumpour. Hybrid rocket engine research in support of prototype development testing. 2009.

[7] Francesco Nasuti Daniele Bianchi. Numerical analysis of nozzle material thermochemical erosion in hybrid rocket engines. *AIAA Journal*, 2013. URL `https://arc.aiaa.org/doi/pdf/10.2514/1.B34813`.

[8] NGR Center. Cea - chemical equilibrium with applications, version 2.0. 1994.

[9] UTAT. Defiance: Breaking the canadian altitude record. 2017.

[10] H.J. Dunn N.M. Alexandrov W.W. Follett G.E. Orient A.H. Hadid J.J. Korte, A.O. Salas. Multidisciplinary approach to linear aerospike nozzle design. *Journal of Propulsion and Power*, 17, 2001.

[11] Brandon Lee Denton. Design and analysis of rocket nozzle contours for launching pico-satellites. 1964. URL `http://scholarworks.rit.edu/cgi/viewcontent.cgi?article=6822&context=theses`.

[12] Lee. Fortran programs for plug nozzle design. 1963.

[13] John D. Anderson. Modern compressible flow with historical perspective.

[14] E. Besnard and J. Garvey. Development and flight-testing of liquid propellant aerospike engines. *40th AIAA/ASME/SAE/ASEE Joint Propulsion Conference and Exhibit*, 2004.

[15] P. Lemieux. Nitrous oxide cooling in hybrid rocket nozzles. *Prog. Aerosp. Sci.*, 14:106–115, 2010.

[16] L. Denies. Regenerative cooling analysis of oxygen/methane rocket engines. *Delft University of Technology*, 2015.

[17] S. D. Eilers. Development of the multiple use plug hybrid for nanosats (muphyn) miniature thruster. *Utah State University*, 2013.

[18] D. R. Bartz. A simple equation for rapid estimation of rocket nozzle convective heat transfer coefficient. *Jet Propulsion Laboratory*, 27:49–53, 1957.

[19] W. Murray J. Mello T. Cooke D. J. Grieb, P. Lemieux and J. Gerhardt. Design and analysis of a reusable n2o-cooled aerospike nozzle for labscale hybrid rocket motor testing. page 5539, 2011.

[20] .W. Lemmon and R. Span. Short fundamental equations of state for 20 industrial fluids. *J. Chem. Eng. Data*, pages 785–850, 2006.

[21] Bernard Geneviève. Developement of a hybrid sounding rocket motor. *University of KwaZulu-Natal*, 2013.

[22] Lauren May Nelson. Rayleight flow of two-phase nitrous oxide as a hybrid rocket nozzle coolant. *California Polytechnic State University*, 2009.

[23] Aspen physical property system. 2013. URL `http://profsite.um.ac.ir/~fanaei/_private/Property%20Methods%208_4.pdf`.

[24] John S. Dennard Charlotte B. Craidon Allen R. Vick, Early H. Andrews Jr. Comparisons of experimental free-jet boundaries with theoretical results obtained with the method of characteristics. *Langley Research Center*, June 1964.

[25] K. Gheshlaghi Amiri M., A.A. Najafi. Response surface methodology and genetic algorithm in optimization of cement clinkering process. *Journal of Applied Science*, 8:2732–2738.

[26] Mirza M. Shah. A new correlation for heat transfer during boiling flow through pipes. *ASHRAE Transactions 82, Part 2*, pages 66–86, 1976.

[27] Mirza M. Shah. Chart correlation for saturated boiling heat transfer; equations and further study. *ASHRAE Transactions, Vol. 88, Part 1*, pages 165–196, 1982.

[28] Dario Pastrone Patrick Lemieux and Pablo Sanchez Arribas. Modeling of n2o heat transfer rates in the nucleate boiling regime, with experimental verification. page 3742. 51st AIAA/SAE/ASEE Joint Propulsion Conference, AIAA Propulsion and Energy Forum, 2015.

[29] Kazimi Mujid S. Todreas Neil E. *Nuclear System I: Thermal Hydraulic Fundamentals*. CRC Press, 2 edition, 2012. ISBN 978-0415802871.

[30] J. Wong. Processing of high performance thermoplastic composites. 2017.

[31] Bruce Rauner. Fiberglass. 2013. URL `http://www.idph.state.il.us/envhealth/factsheets/fiberglass.htm`.

[32] JOE THOMPSON. The die/mould dilemma: Milling graphite. 2017. URL `https://www.canadianmetalworking.com/article/metalworking/the-die-mould-dilemma-milling-graphite`.

[33] Carmen Gonzalez-Lluch Antonio Perez-Gonzalez, Jose L Iserte-Vilar. Interpreting finite element results for brittle materials in endodontic restorations. *Biomed Eng Online*, 2011.

[34] Graphtek L.L.C. Typical grades of graphite. URL `http://www.graphtekllc.com/grades.htm`.

[35] David Warren Whitley. Interacting stress concentration factors and their effect on fatigue of metallic aerostructures. *Doctoral Dissertations*, Fall 2013.

[36] Matt H. Summers. Small-scale hybrid rocket test stand characterization of swirl injectors. 2013.

[37] S. Murugesan Yash Pal, Baskar. Testing of paraffin-based hybrid rocket fuel using gaseous oxygen oxidiser. *Defence Science Journal*, 62:277–283, September 2012.

[38] V.Zakirov. Catalytic decomposition of nitrous oxide for spacecraft propulsion applications. *Surrey Satellite Technology Limited, Centre for Satellite Engineering Research, University of Surrey*, 2000.

[39] Global warming potential values. 2014. URL `http://www.ghgprotocol.org/sites/default/files/ghgp/Global-Warming-Potential-Values%20%28Feb%2016%202016%29_1.pdf`.

[40] Greenhouse gas emissions from a typical passenger vehicle. URL `https://www.epa.gov/greenvehicles/greenhouse-gas-emissions-typical-passenger-vehicle`.

[41] OpenCFD Ltd (ESI Group). User guid: A.1 solvers, 2016. URL `https://www.openfoam.com/documentation/user-guide/standard-solvers.php`.

[42] Eitan Tadmor Alexander Kurganov. New high-resolution central schemes for nonlinear conservation laws and convection-diffusion equations. *Journal of Computational Physics*, pages 241–282, 2000.

[43] Sergio A. Elaskar Luis F. Gutierrez Marcantoni, Jose P. Tamagno. High speed flow simulation using openfoam. *Mecanica Computacional*, XXXI:2939–2959, November 2012.

[44] Oliver Boom. Transonic density based flow solver. *Institute for Flight Propulsion, Technische Universitat Munchen*, 2010.

[45] Inc. ANSYS. 7.3.2 using flow boundary conditions, 2009. URL `http://www.afs.enea.it/project/neptunius/docs/fluent/html/ug/node238.htm`.

[46] Inc. ANSYS. 25.14 initializng the solution, 2006. URL `https://www.sharcnet.ca/Software/Fluent6/html/ug/node1033.htm`.